MINISTRY OF NATIONAL EDUCATION

THE ANNALS OF "DUNAREA DE JOS" UNIVERSITY OF GALATI

Fascicle IX
METALLURGY AND MATERIALS SCIENCE

YEAR XXXV (XXXX)
December 2017, no. 4

ISSN 1453-083X

2017
GALATI UNIVERSITY PRESS

EDITORIAL BOARD

Table of Contents

THE ANNALS OF "DUNAREA DE JOS" UNIVERSITY OF GALATI
FASCICLE IX. METALLURGY AND MATERIALS SCIENCE
N°. 4 - 2017, ISSN 1453-083X

ANALYSIS AND RECOVERY OF SLUDGE FROM THE WASTE WATER FILTERING STATION OF GALAŢI FOR USE IN AGRICULTURE

Beatrice TUDOR
"Dunarea de Jos" University of Galati
e-mail: beatrice.tudor@ugal.ro

ABSTRACT

The paper presents a study on the use of sludge from sewage treatment plants for the purpose of using it in agriculture. The use of biosolids in agriculture is considered the most sustainable option of sewage-sludge management. The purpose of the use of sludge in agriculture is the recovery of content of nutrients and organic matter to mud, thus improving the fertility of the land and reducing farmers' dependence on chemical fertilizers. Due to this, damaging effects on soil, water, vegetation, animals and humans, pollutants can be reduced by using mud.

The application of sewage-sludge on agricultural land is generally the most economical solution, though, because it is seasonal and it represents an opportunity for recycling nutrients, organic matter, and plants for agricultural crops. The nitrogen and potassium contained in mud supplements consistently the demand for fertilizers. Soil fertility can also increase by improving the physical properties of the soil, through the application and incorporation of organic matter contained in the mud.

KEYWORDS: sludge, waste water, agriculture

1. Introduction

The use of treatment/sewage biosolids in agriculture is regarded as the most sustainable method of using them for this purpose and the guide, based on the most consistent scientific data available, ensures that the use of biosolids in agriculture: is compatible with good agricultural practices, does not put at risk the health of humans, animals and plants, maintains the integrity of the soil ecosystem, and avoids polluting environmental factors.

The biosolids can be used in the production of arable crops and fruit trees (10 months before harvesting). Application of biosolids for legumes and berries or pastures is forbidden.

The use of sewage sludge on agricultural land has been a traditional agricultural practice worldwide. These methods eliminate waste and recycle valuable nutrients within the soil-plant system.

The problem of sludge application in agriculture is complex and needs very good monitoring to avoid the occurrence of adverse effects; account must be taken of the physical, chemical and microbiological properties of the sludge and of the soil properties, the capacity of the plants to benefit from the nutrients to be found in the sludge and the danger of environmental pollution. The issue of transport and access roads to agricultural land should also be considered.

The use of sludge in agriculture is an economical and beneficial solution for both soils and agricultural crops. The purpose of using sludge is to utilize the sludge from Wastewater Treatment Plants so it could be used in agriculture, while any adverse effects of sludge on human health and the environment be avoided [1, 2, 6].

2. Experimental results

We took a set of 5 sludge samples from the Galati Waste Water Treatment Plant and these are: primary sludge; dehydrated sludge; sludge thickened with polyelectrolyte added; fermented sludge; sludge from the anaerobic fermenter.

Determination of the metals from the sludge samples, were analyzed in the laboratories of the Faculty of Engineering, using the X-ray spectrometer (Fig. 1).

Sewage sludge samples were processed to analyze them in a number of steps.

Fig. 1. *X-ray spectrometer*

Primary sludge

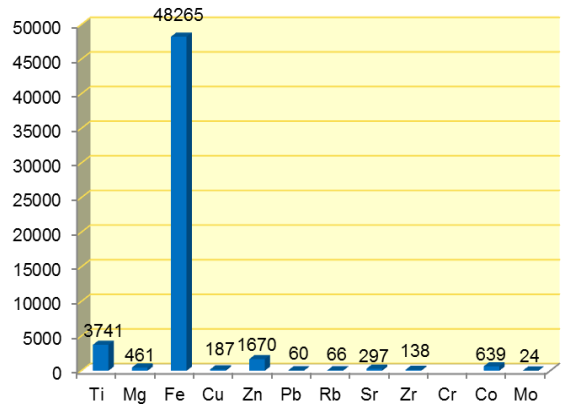

Fig. 2. *Metals detected in the primary sludge sample*

From the primary sludge sample taken by the Wastewater Treatment Plant in Galati from the secondary stage we found that all the elements are above the admissible limits, which means that the primary sludge has to be treated before being used in agriculture [3].

In the sample with primary sludge, all elements are above permitted limits, which results in the primary sludge being treated before it is used in agriculture (Fig. 2).

Regarding the dehydrated sludge from Galati purification plant, the sludge is the result of waste water treatment. This sludge comes from both the primary treatment stage and the secondary stage. The concentration of dry matter in the sludge is low and the volume it occupies is very high, making it difficult to handle and very costly to transport. To overcome these problems, a sludge dehydration plant is always needed.

Dehydrated sludge, although falling within the admissible limits in terms of chemical content should be treated for use in agriculture (Fig. 3).

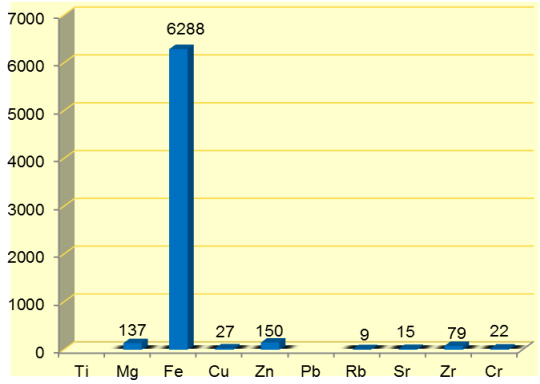

Fig. 3. *The metals detected in the dehydrated sludge sample at the Galati purification plant*

For sludge thickened with polyelectrolyte addition the polyelectrolytes are distributed in solid form (dust and granulate) and liquid, namely emulsion and dispersion.

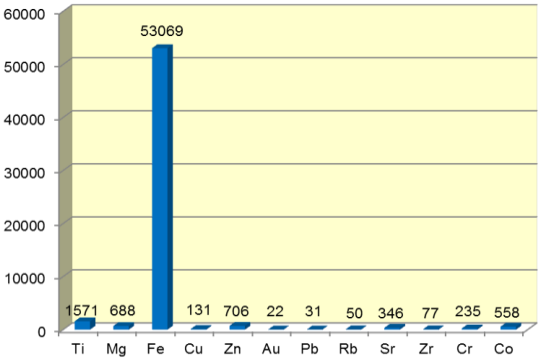

Fig. 4. *The metals detected in the sludge thickened with polyelectrolyte added*

For fermented sludge the samples with sludge thickened with polyelectrolyte added, and fermented sludge, should be treated, although the addition of

polyelectrolyte improves the physical, chemical and biological properties of soil, with the exception of saturated soils (Fig. 4, Fig. 6).

Fig. 5. *Dry sludge sample, inserted into the X-ray spectrometer*

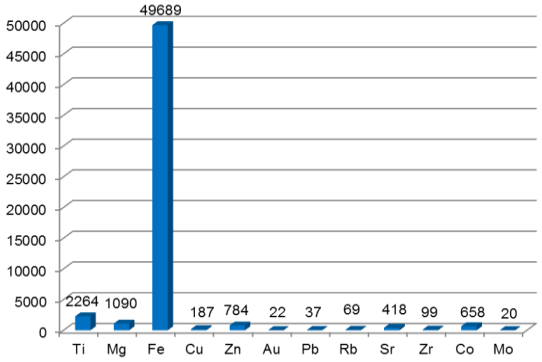

Fig. 6. *The metals detected in the fermented sludge*

In the case of the sludge from the anaerobic fermenter, the anaerobic fermenter-Dig2 is the process of biological degradation of organic substances from sludge by the activity of bacterial populations which, under certain environmental conditions (pH, temperature, etc.), decompose organics from the sludge through biochemical oxidation reduction processes into simple molecules CH_4, CO, CO_2 and H_2, which form the so-called fermentation gas or biogas, and which has an average calorific value of about 5,000 kcal/Nm^3 [4, 5].

Anaerobic Dig 2 fermenter improves sludge dewatering, stabilizes sludge, reduces odor and solids (Fig.7).

Regarding the determination of pH in sewage sludge, this was done on all 5 dry sludge samples from the Galati Waste Water Treatment Plant using the apparatus called Hach HQ40d, pH Multiparameter (Fig. 8).

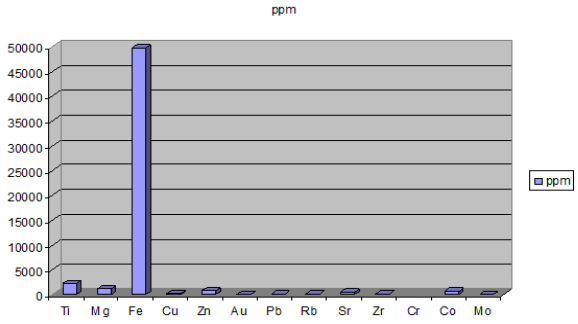

Fig. 7. *The metals detected in the sludge from the anaerobic fermenter*

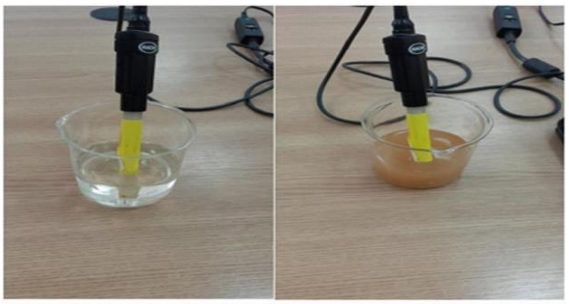

Fig. 8. *PH electrolysis*

Table 1. *PH values of the sludge samples*

Samples	pH
Primary sludge	7.42
Dehydrated sludge	7.75
Slurry thickened with polyelectrolyte added	7.85
Fermented sludge	7.68
Sludge from the anaerobic fermented	7.66

Most plants prefer soil with a pH ranging from 6.5 to 7.5. After determining the pH of the sludge samples, a value ranging from 7.42 to 7.85 was obtained, which means it is obligatory for the sludge to be treated to be used in agriculture. It is necessary to reduce salt and use calcium phosphate (Fig. 9).

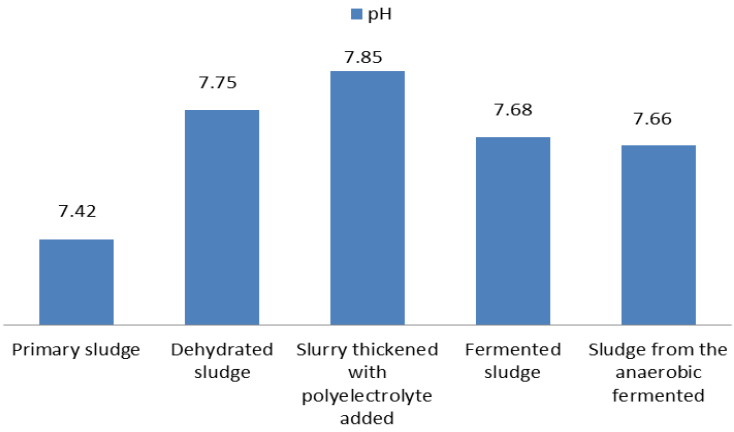

Fig. 9. *pH of sludge samples from the Galati purification plant*

3. Conclusions

The application of sewage sludge in agriculture is an economical and sustainable solution because it has the advantage of recycling nutrients to develop crops while being an ecological solution for the recovery and use of sewage sludge from urban agglomerations.

Most heavy metals found in sewage sludge come from diffuse sources difficult to control, including the erosion of the metallic water distribution network, domestic products.

Heavy metals reach the ground, air, water and sludge. From the surface they descend into the soil through diffusion, absorption, and carried away by water or macro-organisms.

Soil resistance to heavy metal pollution differs depending on the nature of the soil. Thus, clay soils retain more pollutants, neutral and carbonate soils retain strongly, while sandy soils retain the least (leaching is strong, except Mo and Se). Also, the finer the texture of soil is, the more pollutants retained in the soil there are, wherefrom they pass through plants.

Some heavy metals (Zn and Cu) are essential microelements in plant nutrition and feature toxicity only in high concentrations. Other elements (cadmium, lead, mercury) show toxic action in the food chain, and their limit values are set by Order 34412A04 so that humans and animals are protected.

The content of heavy metals is inevitably found in urban sludge, the industrial wastewater discharged into the original sewerage system being always their main source but by controlling the discharge of sewage into the sewage system, it has progressively been reduced the concentrations of heavy metals in the sludge across Europe.

Acknowledgement

The authors wish to thank the student Simona Pesu who helped us in this study.

References

[1]. ***, *Ghid pentru Dezvoltarea unui Plan de Management Regional privind Utilizarea Benefică a Nămolului în Sol*.
[2]. ***, *Elaborarea politicii nationale de gestionare a namolurilor de epurare*, AM POS Mediu-Septembrie 2011.
[3]. ***, http://documents.tips/documents/tratarea-namolurilor-in-statiile-de-epurare.
[4]. ***, http://aquamundus.ro/epurarea%20biologica.php.
[5]. ***, http://ecotrust.ro/ro/blog-ecotrust/70-namolul-activ
[6]. ***, http://www.wall street.ro/articol/Economie/111107/P-BiotehnologiiIe-O-solutie-eficienta-pentru-epurarea-apelor-uzate.html.
[7]. ***, https://ro.scribd.com/document/224380503/Namol-Activ.

THE ANNALS OF "DUNAREA DE JOS" UNIVERSITY OF GALATI
FASCICLE IX. METALLURGY AND MATERIALS SCIENCE
N°. 4 - 2017, ISSN 1453-083X

STUDY ON THE USE OF OXYGEN-ENRICHED COMBUSTION AIR AT THE IGNITION INITIATOR FURNACE FROM THE AGGLOMERATION MACHINE

Adrian VASILIU
"Dunarea de Jos" University of Galati, Romania
email: avasiliu@ugal.ro

ABSTRACT

Comparative study on the use of oxygen-enriched combustion air at the homogenization coal ignition coil from Dwight-Lloyd agglomeration No 5 from the ArcelorMittal Galati metallurgic plant to reduce fuel consumption, increase machine productivity and agglomerate quality.

KEYWORDS: agglomeration process, ignition furnace, oxygen enriched air, heat balancing furnace

1. Introduction

Sintering iron ore is a thermal treatment process for agglomerating fine particles into larger pieces, which then serve as raw material for the furnace. High quality sintering is essential for efficient furnace operation. The quality and yield of the agglomerate are largely determined by the iron ore's chemical properties, such as physical behaviors and chemical reactions of the sintering materials during the process. The thermal treatment and treatment of the material deposited on the agglomeration machine affects the structure and mineralization at temperatures high and has a high influence on quality indices, sintering efficiency and fuel consumption.

The sintering process consists of combining iron-bearing fines with a solid fuel and igniting the mixture on a traveling grate with a downdraft of air. As the fuel burns, the temperature in the bed increases to about 1300 °C to 1480 °C, sintering the fines into a porous, clinker-like material that is suitable for use as blast furnace feed. The bonding between the particles is by recrystallization and partial melting, and so no additional binder needs to be added in this process.

Sintering is a continuous agglomeration process in which mixtures of fine iron ores, streams, coke and recycled materials are melted together to produce a porous material designated as sinter. A scheme of the process is shown in Figure 1. A raw sinter mixture of raw materials is placed on a continuous grate which moves slowly (sintering wire) typically 40-60 cm deep and 4-5 m wide.

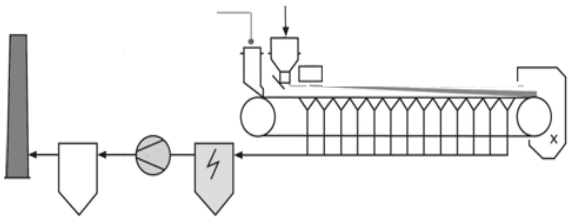

Fig. 1. *Dwight - Lloyd agglomeration band*

2. Objectives

In the agglomeration process, ignition and thermal treatment of the sintered layer is of great importance in achieving high productivity, low coke consumption and superior agglomeration quality.
The purpose of this paper is to develop methods for calculating fuel gas consumption to ignite the sintered load and the specific energy consumption of the process as well as to determine the main parameters that affect this value.

In order for the furnace to have a high ignition temperature, optimal use of gaseous fuel is required, therefore a complete gas burning. Without unbound gas, it increases fuel consumption, delays the burning of coke and lowers the furnace temperature.

Decreasing coke consumption is achieved by better use of gaseous fuel and by increasing the percentage of oxygen at the same ignition heat.

Currently, the energetic performance of the ignition of the load is empirically determined, which does not allow the identification of the factors that influence the sintering process and the reduction of the energy consumption for its implementation.

By modifying the percentage of oxygen in the air, the ratio between the thermal wave travel rate and the combustion rate is changed. Oxygen can increase specific agglomeration production, promote a better oxidized useful sinter with better reducibility. If a higher temperature is reached at the front of the flame, the fuel consumption will be reduced, but more NOx will be produced in the flue gases.

The presence of air enriched in a small amount of oxygen in the front of the flame is a means of raising the temperature in the ignition furnace of the homogenized layer and to obtain a better quality of the agglomerate. In this paper, oxygen-enriched air was used, between 21% and 24% of the total oxygen.

From experiments at agglomeration plants in the world, it was concluded that adding oxygen to combustion air leads to an increase in productivity by 3-4% for each additional oxygen percentage.

3. Theoretical considerations

The adiabatic flame temperature is calculated at different oxygen concentrations. The results show that the adiabatic flame temperature increases with a higher concentration of oxygen in the combustion air as shown in the green line in Figure 2. The red line shows how the adiabatic temperature changes with different oxygen concentrations when considering the gas dissociation (H_2O, CO_2 SO_2).

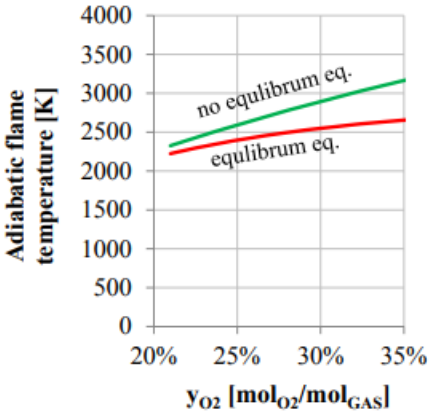

Fig. 2. *Adiabatic flame temperature*

What we are most concerned about possible energy savings is how much fuel we can save with oxygen-enriched combustion. The amount of energy leaking with the exhaust gas decreases as the oxygen concentration increases as the resulting amount of nitrogen decreases (Figure 3).

The amount of energy produced by combustion with 21% oxygen in the combustion air is used as a reference. With increasing oxygen concentration in the combustion air, more energy is available from the combustion so that less fuel is needed.

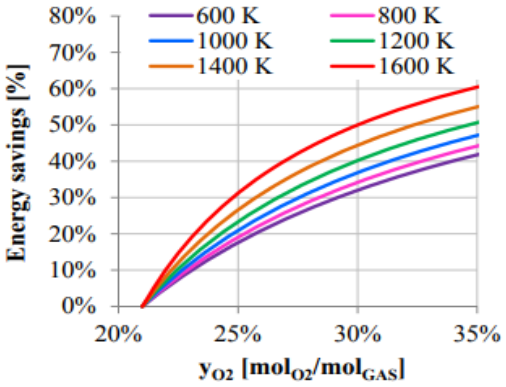

Fig. 3. *Energy savings*

Burning of hydrocarbons. For a hydrocarbon consisting solely of carbon and hydrogen, of the formula CxHy, the combustion reaction is (Figure 4).

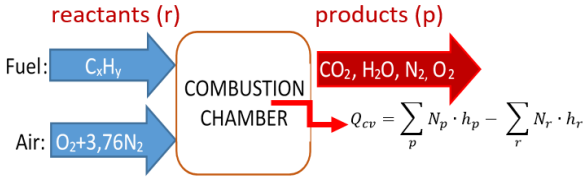

Fig. 4. *The hydrocarbon burning equation*

The composition of the air is in molar fractions, 21% oxygen, 78% nitrogen and 1% argon. These two substances are supposed to be inert, and for simplicity, air is considered to be composed of 21% oxygen and 79% nitrogen to which a fictitious molar mass is attributed, the presence of argon. The combustion reaction of a hydrocarbon with air thus becomes:

$$C_xH_y + \left(x + \frac{y}{4}\right)O_2 + \frac{79}{21}\left(x + \frac{y}{4}\right)N_2 \rightarrow$$
$$\rightarrow xCO_2 + + \frac{y}{2}H_2O + \frac{79}{21}\left(x + \frac{y}{4}\right)N_2 \quad (1)$$

It is said that the reaction is complete if the exhaust gases contain, in addition to inert elements, only fully oxidized products.

To achieve complete combustion with theoretical air, a perfect blend would be needed. In practice, to ensure complete firing, you need an excess of air (λ). This is characterized by the theoretical air coefficient or the excess air coefficient:

$$\lambda = \frac{used\ air}{theoretical\ air} \qquad (2)$$

Regarding the adiabatic flame temperature, the adiabatic combustion reaction is without the kinetic and potential energy variation. The temperature of products of this type of reaction is called adiabatic flame or combustion temperature. In this hypothesis, the absence of work and variations in kinetic energy is the maximum temperature that can be reached for a certain type of fuel at its pressure and temperature.

Adiabatic flame temperature (ta) is no longer theoretical and is maximum for a stoichiometric mixture. It is calculated based on the first principle with the equation:

$$t_a = \frac{Q_i - Q_{dis} + L_{min} \cdot i_a + i_c}{c_{smga} \cdot v_{ga}} \left[{}^0C \right] \qquad (3)$$

Heat required for ignition. Heating the layer with an external heat source is required to create a sufficiently high temperature to ignite the solid fuel (coke) at the top of the layer and heat it to a sufficient depth to provide additional fuel ignition in the lower. In this combustion process, the gases resulting from the combustion burned in the ignition furnace are absorbed through the homogenized layer (hearth).

The characteristic dimensions that are taken into account when heating the layer from an external heat source. The intensity of ignition is:

$$I = 60 \cdot c_h \cdot t_c \cdot w_h \ [kJ/m^2\ min.] \qquad (4)$$

is directly proportional to the gas flow rate through the homogenized layer, wh, (m^3/m^2s) and the specific heat of the flue gas c_h (kJ/m^3K).

The heat received by the homogenized to ignite the coating is:

$$Q' = I \cdot \tau_{ig} \ [kJ/m^2] \qquad (5)$$

- t_c - furnace temperature ($t_c \approx 1250 \div 1300$ °C);
- τ_{ig}, - ignition time ($\tau_{ig} = l_h / w_h$) (min);
- I, - specific ignition intensity (kJ / m^2 min).

4. Method of research

4.1. Thermal check of the ignition furnace

Before the actual balancing of the agglomeration machine was made, the firing furnace was chosen as a balance sheet, whose thermal balance led to the highlighting of the energy consumptions made for the ignition of the batch layer and the determination of the furnace's energy efficiency (Figure 5). Because the agglomeration manufacturing process is of a continuous nature, the balance is made per unit of product, that is, per ton of agglomerate. The batch sintering process is carried out on an agglomeration machine having an active surface area of 300 m².

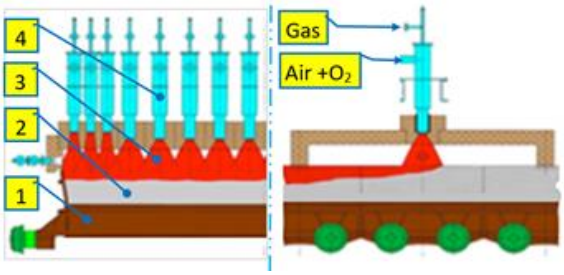

Fig. 5. *Ignition furnace. 1. Pallet; 2. Sinter mixture; 3. Flame cycle; 4. Burners*

4.2. Combustion of gas

The average chemical composition of the fuel gas is shown in table no. 1.

Table 1

Elements	N_2	CH_4	C_2H_6	C_3H_8	C_4H_{10}	O_2	Hi [kJ/m^3_N]
(%)	8.3	87.94	0.69	0.28	0.19	2.6	35635
c_{sp} (25 °C)	1.04	2.17	1.75	1.672	1.828		
q (x 10^3)	-	39.8	70.5	101.8	134.0	-	

Combustion heat (lower calorific value):

$$H_i = \sum_{i=1}^{n} H_{ik} \cdot r_k = 35635 \ [kJ/m^3_{Ncb}] \qquad (6)$$

Combustion reactions (equation 1):

$$\begin{cases} CH_4 + 2\ O_2 & = CO_2 + 2H_2O \\ C_2H_6 + 3{,}5\ O_2 & = 2\ CO_2 + 3H_2O \\ C_3H_8 + 5O_2 & = 3\ CO_2 + 4H_2O \\ C_4H_{10} + 6{,}5\ O_2 & = 4\ CO_2 + 5H_2O \end{cases}$$

Stoichiometric oxygen required for combustion:

$$O_{nec} = \sum_{i=1}^{n} \left(x + \frac{y}{2}\right) \cdot \%C_xH_y = 1{,}7833\ m^3_{NO2}/\ m^3_{Ncb}$$

Actual air required for combustion (equation 2):

Table 2

The real air [m^3_{Naer} / m^3_{Ncb}]	
(21 % O_2)	(24 % O_2)
$L_{nec} = \frac{100}{21} \cdot O_{nec} = 8,49$	$L_{nec} = \frac{100}{24} \cdot O_{nec} = 7,43$
$L_{real} = \lambda \cdot O_{nec} = 9,34$	$L_{real} = \lambda \cdot O_{nec} = 8,17$

Flue gas volume resulting from combustion:

$$V_{ga} = V_{CO2} + V_{H2O} + V_{N2} + V_{Oex} \quad (7)$$

Table 3

21 % O_2	V_{CO_2}= (CH_4+2C_2H_6+3C_3H_8+4C_4H_{10})/100 = 0.9092	
	V_{H_2O}= (2CH_4+3C_2H_6+4C_3H_8+5C_4H_{10})/100 =1.8002	
	V_{N_2}= (L_{real} 79) / 100 + N_i/100 = 7.4616	
	V_{Oex}= L_{nec}·(λ -1)·21/100·= 0.17829	
TOTAL		Vga = 10.34929

Table 4

24 % O_2	V_{CO_2}= (CH_4+2C_2H_6+3C_3H_8+4C_4H_{10})/100 = 0.9092	
	V_{H_2O}= (2CH_4+3C_2H_6+4C_3H_8+5C_4H_{10})/100 =1.8002	
	V'_{N2} = (L_{real} ·76) / 100 + N_i / 100 = 6.2922	
	V'_{Oex} = L_{nec}· (λ -1)·24 / 100 = 0.17832	
TOTAL		**Vga = 9.17992**

The share of each gas in the flue gas volume:

$$x_i = \frac{V_i}{V_{ga}} \cdot 100\ [\%] \quad (8)$$

Table 5

Percent [%]		X_{CO2}	X_{H2O}	X_{N2}	X_{Oex}	Total
Oxygen [%]	21	8.792	17.394	72.095	1.724	100
	24	9.904	19.611	68.543	1.942	100

Temperature resulting from combustion (equation 3):

Table 6

Oxygen [%]	Enthalpy [kJ/ m^3_N]		Temperature [^{0}C]	
	air *	gas **	theoretical	real ***
21	26.021	1.651	2050	1558
24	26.022	1.705	2349	1785

* i_a - combustion air enthalpy ($i_a = t_a \cdot c_a$; at t_a = 20 °C)
** i_g - combustion gas enthalpy ($i_g = t_g \cdot c_g$; at $t_g = t_a$ °C)
*** t_r – real combustion temperature ($t_r = \eta \cdot t_a$; η = 0.76)

4.3. Heat kiln heat exchanger

Characteristics of the furnace:
- type: room with burners in the vault;
- destination: ignition of the batch layer;
- working regime: continuous;
- focal size: 7 m x 3 m x 1,5 m (l x b x h);
- operating temperature: 1250 °C;
- gas consumption: average 785 m³N / h;
- air consumption (λ = 1,1): 8500 m³N / h.

Characteristics of the agglomeration machine:
- productivity 1600 t / h (850 t / h with exhaust);
- specific productivity: 20 ÷ 40 t / m^2 per day;
- area: 300 m^2;
- speed: 1.5 - 6.5 m / min;
- maximum useful floor height: 550-600 mm;
- trolley length: 1500 mm;
- trolley width: 3000 mm;
- trolley height: 600 mm.

4.4. Heat balance of the furnace (O_2-21%)

Heat inputs: The lack of oxygen in the area of the furnace contributes to delaying the ignition of the superficial layer, which implicitly determines the delay of the firing front transmission to the grills. The heat enters the outline are:
- the chemical heat of the fuel gas (Q_1);
- physical heat of the fuel gas (Q_2);
- sensible heat of combustion air (Q_3).

Chemical Heat of Gas (Q_1):

$$Q_1 = \frac{B_{CH4} \cdot H_i}{P_{aglo}} = 163643,72\ \left[kJ/t_{aglo.}\right]$$

where:
- fuel gas - methane gas;
- B_{gaz} - specific fuel gas [m^3_N / h];
- H_i - heat fuel efficiency [kJ / m^3_N];
- P_{aglo} production of agglomerate [t / m^2zi];

Physical Heat of Gas (Q_2):

$$Q_2 = \frac{B_{CH4} \cdot i_{CH4}}{P_{aglo.}} = 260,75\ \left[kJ/t_{aglo.}\right]$$

The enthalpy of gas is calculated by:

$$i_{CH4} = \sum x_n \cdot c_n \cdot t_n = 51,12\ [kJ/m^3_n]$$

where:

i_{CH4}-enthalpy of gas at temperature [kJ/m^3_N];
x_n - percent of gases n in the gas composition [%];
c_n - the specific heat of component n, [kJ/m^3_N grd];
t_n – temperature of gas from the entrance, [°C].

Physical Heat of combustion air (Q_3):

$$Q_3 = \frac{L_{real} \cdot B_{CH4} \cdot i_a}{P_{aglo}} = 1539{,}08 \ [kJ/t_{aglo.}]$$

where:

L_{real} - the amount of air required, [m$^3_{N\ air}$/ m$^3_{N\ gaz}$];

i_a - enthalpy of combustion air at t=20 °C [kJ/m^3_N].

Total heat entering the contour:

$$\sum_{i=1}^{3} Q_{Ti} = Q_1 + Q_2 + Q_3 = 165443{,}55 \ [kJ/t_{aglo.}]$$

Table 7. *Entry in the account balance*

No. crt.	Inputs			
	Heat	Symbol	Quantity	
			kJ/t agl	%
1	The chemical heat of methane gas	Q_1	163643,72	98,91
2	Physical heat of methane gas	Q_2	260,75	0,157
3	Physical heat of combustion air	Q_3	1539,08	1,6
TOTAL		$\sum Q_{Ti}$	**165443,55**	**100**

Heat outputs:
- heat loss through radiation (Q_4);
- heat lost through trolley walls (Q_5);
- heat lost with the gases from the layer (Q_6);
- heat loss through furnace walls (Q_7);
- useful heat (firing layer) (Q_8).

Heat loss through radiation through holes (Q4):

$$Q_4 = \frac{C_0 \cdot S \cdot \varphi \cdot \left[\left(\frac{T_c}{100}\right)^4 - \left(\frac{T_a}{100}\right)^4\right] \cdot \tau}{P_{aglo}} = 1587{,}26$$

where:
- C_0 – emission factor, (C_0 = 5.67), [W/m^2 h K^4];
- S - opening area [m^2];
- τ - the time at which the opening (τ = 1 h);
- T_c - radiator wall temperature (T_c = 273 + t_c), [°K];
- T_a - ambient temperature (T_a = 273 + t_a), [°K].

The surface of the apertures and the aperture coefficient are calculated separately for the furnace front apertures and for the visors practiced in the side walls of the furnace.

Heat lost through the troller walls (Q_5):

$$Q_5 = \frac{M_c \cdot c_c \cdot (t'_p - t''_p)}{P_{aglo.}} = 12525{,}90 \ [kJ/t_{aglo.}]$$

where:
- Mc - mass of trolleys
$M_c = V \cdot \rho = 190 \ [kg]$;
- V - volume of side walls (V = 0.025 m^3)
- ρ_c - wall material density (ρ_c = 7600 [Kg/m^3]
- c - specific heat (c = 0.56916 kJ/kg grd);
- t_p', t_p'' - the temperature of the side walls [°C];
- (t'_p = 194 °C; t''_p = 77 °C).

Heat lost with the gases coming out of the layer (Q_6):

$$Q_6 = \frac{B \cdot \left(0{,}1 \cdot c_{ga}^{tp} \cdot t_p + 0{,}9 \cdot c_{ga}^{ts} \cdot t_e\right)}{P_{aglo}} = 24285{,}13$$

where:
- B = specific gas consumption [m^3_N / t $_{aglo}$];
- c_{gae}, c_{gap} - heat-specific gas that is lost and drawn by the exhaust (t_e = 125 °C and t_p = 1067 °C).

Heat lost through the walls of the furnace (Q_7):

$$Q_7 = Q_{71} + Q_{72} + Q_{73} + Q_{74} + Q_{75} \ [kJ/t_{aglo}]$$

in which:
- Q_{71} - lost through the right wall, [kJ / t_{aglo}];
- Q_{72} - lost through the left wall [kJ / t_{aglo}];
- Q_{73} - lost through the kiln vault [kJ / t_{aglo}];
- Q_{74} - lost through the front wall [kJ / t_{aglo}];
- Q_{75} - lost through the back wall [kJ / t_{aglo}].

$$Q_7 = \sum_{i=1}^{5} Q_{7i} = \sum_{i=1}^{5} \frac{\alpha_{ci}(t_{ei} - t_{ai})}{P_{aglo}} \cdot S_i = 2797{,}75$$

where:
- α_c - coefficient of exchange by convection;
- t_e - the outer wall temperature, [°C];
- t_a - air temperature, [°C];

- S - heat exchange area, [m²].

Heat released to the layer band - ignition (Q_8):

$$Q_u = Q_8 = \sum_{i=1}^{3} Q_i - \sum_{i=4}^{7} Q_i = 124247{,}51\left[\mathrm{kJ/t_{aglo}}\right]$$

Total heat consumed:

$$Q_{Tc} = \sum_{i=4}^{8} Q_i = 165443{,}55\ [kJ/t_{aglo}]$$

The furnace's thermal yield - η_t:

$$\eta_t = \frac{Q_u}{B \cdot v_{ga} \cdot (i_0 - i_{gc})} \cdot 100 = 76{,}5\ \ [\%]$$

Specific fuel consumption:

$$B_{sp} = \frac{B \cdot H_i \cdot \rho_{gaz}}{H_{cc}} = 683{,}7\ [kg_{cc}\ /t_{aglo}]$$

Table 8. *Outputs in the account balance*

No. crt.	OUTPUTS			
	Heat	Symbol	Quantity	
			kJ/t agl	%
1	Heat loss through radiation	Q_4	1587,26	1,259
2	Heat lost through the troller walls	Q_5	12525,90	7,572
3	Heat lost by the gas through the layer	Q_6	24285,13	14,678
4	Heat loss through furnace walls	Q_7	2797,75	1,691
5	Heat released to the layer band - ignition	Q_8	124247,51	75,467
TOTAL		$\sum Q_{Tc}$	**165443,54**	**100**

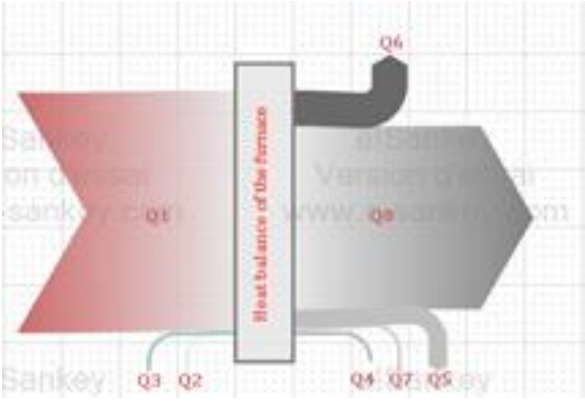

Fig. 6. *Heat balance of the furnace (21% Oxygen)*

Sankey diagram (O_2-free): Heat consumed and generated during the combustion process is estimated by thermal balances. The heat is released mainly due to the combustion of gas in the ignition furnace. A typical heat balance in the firing furnace at sinter plants is shown in Table 7 and Table 8 and is graphically represented in Figure 6.

4.5. Heat balance of the furnace (O_2-24%)

Heat inputs

- the chemical heat of the fuel gas (Q_1^{ox});
- physical heat of the fuel gas (Q_2^{ox});
- sensible heat of combustion air (Q_3^{ox});
- chemical heat resulting from the combustion of CO from the atmosphere of the furnace (Q_4^{ox});
- the physical heat of carbon dioxide (Q_5^{ox}).

Chemical Heat of Gas (Q_1^{ox}):

$$Q_1^{ox} = \frac{B_{CH4} \cdot H_i}{P_{aglo}} = 163643{,}72\ \ [kJ/t_{aglo.}]$$

Physical Heat of Gas (Q_2^{ox}):

$$Q_2^{ox} = \frac{B_{CH4} \cdot i_{CH4}}{P_{aglo.}} == 260{,}75\ \ [kJ/t_{aglo.}]$$

Physical heat of combustion air (Q_3^{ox}):

After the introduction of oxygen, an increase in air oxygen percentage of 3.8% was found to result in 22.4% in the combustion air, which corresponds to an oxygen flow of 969 m³ / h. So, at an excess of $\lambda = 1.4$, the air required to burn a m^3_N CH_4 will be:

$$Q_3^{ox} = \frac{L_{real}^{ox} \cdot B_{CH4} \cdot i_a}{P_{aglo}} = 3670{,}24\ \ [kJ/t_{aglo.}]$$

where:

- L_{real}^{ox} - the amount of air required, [$m^3_{N\ air}$/ $m^3_{N\ gaz}$];
- i_a - enthalpy of combustion air at t=20 °C [kJ/m^3_N].

Table 9

No. crt.	Oxygen flow		
	m^3N/h	%	O in air %
1	35.05	21.79	3.4
2	39.17	22.44	3.8
3	45.36	23.20	4.4

Heat of combustion of CO in the furnace (Q_4^{ox}): We calculate the excess air, (λ_1), resulting from flue gas analyzes, after the introduction of oxygen.

The volume of CO corresponding to 1.8% of the flue gases before the introduction of oxygen.

$$Q_4^{ox} = \frac{V_{CO} \cdot q_{CO}}{P_{aglo}} = 17694{,}18\ [kJ/t_{aglo}]$$

where:

- V_{CO} - volume of carbon dioxide no burn, [m^3_{NCO}];
- q_{CO} - thermal effect of combustion, CO [kJ/m^3_{CO}].

The physical heat of carbon dioxide (Q_5^{ox}):

$$Q_5^{ox} = \frac{V_{CO} \cdot i_{CO}}{P_{aglo}} = 2120{,}95\ \ [kj/t_{aglo}]$$

i_{CO} – enthalpy CO la t_{ga}≈1050 °C (i_{CO}=1520) [kj/m^3_N]

Total heat entering the contour:

$$\sum_{i=1}^{5} Q_i^{ox} = 165443{,}55\ [kJ/t_{aglo.}]$$

Table 10. *Entry in the account balance*

No. crt.	INPUTS			
	Heat	Symbol	Quantity	
			kJ/t agl	%
1	The chemical heat of methane gas	Q_1^{ox}	163643,72	87,328
2	Physical heat of methane gas	Q_2^{ox}	260,75	0,139
3	Physical heat of combustion air	Q_3^{ox}	3670,24	1,958
4	Heat of combustion of CO in the furnace	Q_4^{ox}	17694,18	9,442
5	Physical heat of carbon dioxide	Q_5^{ox}	2120,95	1,132
TOTAL		$\sum Q_{Ti}^{ox}$	**187389,66**	**100**

Heat outputs:

- heat loss through radiation (Q_6^{ox});
- heat lost through the furnace walls (Q_7^{ox});
- heat lost through the trolley walls (Q_8^{ox});
- heat lost with the gases from the layer (Q_9^{ox});
- useful heat (firing layer) (Q_{10}^{ox}).

Heat loss through radiation (Q_6^{ox}):

$$Q_6^{ox} \frac{C_0 \cdot S \cdot \varphi \cdot \left[\left(\frac{T_c}{100}\right)^4 - \left(\frac{T_a}{100}\right)^4\right] \cdot \tau}{P_{aglo}} = 1587{,}26$$

Heat loss through the walls of the furnace (Q_7^{ox}):

$$Q_7^{ox} = \sum_{i=1}^{5} \frac{\alpha_{ci}(t_{ei} - t_{ai})}{P_{aglo}} \cdot S_i = 2797{,}67\ [kJ/t_{aglo.}]$$

Heat accumulated in the trolley walls (Q_8^{ox}):

$$Q_8^{ox} = \frac{M_c \cdot c_c \cdot (t_p' - t_p'')}{P_{aglo.}} = 12525{,}9[\text{kJ/t}_{\text{aglo.}}]$$

Heat lost with the gases coming out of the layer (Q_9^{ox}):

$$Q_9^{ox} = \frac{M_c \cdot c_c \cdot (t_p' - t_p'')}{P_{aglo.}} = 24285{,}13\ [\text{kJ/t}_{\text{aglo.}}]$$

Heat released to the layer band - ignition (Q_{10}^{ox}):

$$Q_u = Q_{10}^{ox} = \sum_{i=1}^{9} Q_{Ti} - \sum_{i=4}^{9} Q_i = 124247{,}5[\text{kJ/t}_{\text{aglo}}]$$

Total heat consumed:

$$Q_{Tc} = \sum_{8}^{i=4} Q_i = 146182{,}67[kJ/t_{aglo}]$$

The furnace's thermal yield - η_t:

$$\eta_t = \frac{Q_u}{B \cdot v_{ga} \cdot (i_0 - i_{gc})} \cdot 100 = 78{,}4\ \ [\%]$$

Table 11. *Outputs in the account balance*

No. crt.	OUTPUTS			
	Heat	Symbol	Quantity	
			kJ/t agl	%
1	Heat loss through radiation	Q_6^{ox}	1587,26	0,847
2	Heat lost through the walls of the furnace	Q_7^{ox}	2797,67	1,493
3	Heat lost through the trolley walls	Q_8^{ox}	12525,90	6,684
4	Heat lost by the gas through the layer	Q_9^{ox}	24285,13	12,959
5	Heat released to the layer band - ignition	$Q_{10}(Qu)$	146182,67	78,017
TOTAL		$\sum Q_{Tc}^{ox}$	**187389,66**	**100**

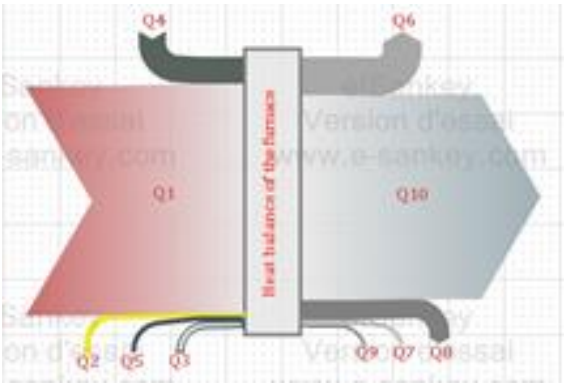

Fig. 7. *Heat balance of the furnace (24% Oxygen)*

5. Conclusions

The influence of ignition on the sintering process, and thus the quality of the agglomerate, is manifested at the temperature at which the superficial layer of the agglomeration mixture is heated at the time of ignition. This value has a limited variation of variation and overcoming the upper bound leads to the formation of a compact, slightly permeable but extremely brittle crust, and an intermittent temperature below the lower limit leads to the formation of a layer of non-sintered material that completely passes in the return. From the above, the following resulted:

- the optimal percentage of oxygen in the combustion air is 22.4%;
- the amount of air required to burn the gaseous fuel decreases as the air enriches the oxygen;
- the amount of combustion gases decreases as the percentage of oxygen in the combustion air increases, thus reducing the heat loss by evacuating them;
- by increasing the oxygen content, complete combustion of the fuel is achieved;
- heat yield of the furnace improves from 75.72% to 78.4%;
- the introduction of oxygen leads to increased reaction rates in the layer, increasing the vertical sintering speed and thus increasing the agglomeration machine productivity.

The ignition furnace is compact. The volume has been reduced and the length of the oven has been reduced by reducing the burner flame, reducing the ceiling height of the furnace and shortening the ignition time by igniting at high temperatures. To meet the above requirements, the ignition furnace must be equipped with the following features:

- the flame burner should operate at a low speed to avoid disruption of the gross feed bed;
- the flat flame is advantageous for rapid and uniform ignition of the green supply;
- proper provision is essential to obtain regular cooling air supply with the burners to achieve the desired flame temperature;
- there must be adequate burner controls that are easy to handle;
- all oven controls must be safe.

The advantages are: reduced size (length), low energy consumption, CO_2 reduction, superior sintering, low return, less maintenance, short return time.

In view of the findings of the experiments, it is necessary to apply this oxygen injection system to the combustion air at agglomeration machine.

References

[1]. ***, *Documentation form ArcelorMittal Galati*.
[2]. Xinyu Ming, *Possibility of Combustion Furnace Operation with Oxygen*, University of Michigan, Mechanical Engineering, p. 3-2.
[3]. Berinde T., *et al.*, *Întocmirea și analiza bilanțurilor energetice în industrie*, Editura Tehnică, 2006.
[4]. Vegman E. F., *Theory and practice of agglomeration*, Moscow, Metallurgy, p. 288, 1974.
[5]. Gerasimov L. K., *Experience of the design and development of ignition furnace for sintering machines*, Steel, no. 3, p. 23-27, 2010.
[6]. Frolov Yu. A., *Thermal aspects of the initial period of agglomeration*, Steel, no. 1, p. 2-10, 2004.

THE ANNALS OF "DUNAREA DE JOS" UNIVERSITY OF GALATI
FASCICLE IX. METALLURGY AND MATERIALS SCIENCE
N°. 4 - 2017, ISSN 1453-083X

HEAVY METALS AND PHYSICO-CHEMICAL PARAMETERS ANALYSIS FROM THE WELLS IN THE BUHOCI AREA, BACAU

Alina COCHIORCA[1]*, Valentin NEDEFF[1], Adriano FIORUCCI[2], Mirela PANAINTE-LEHĂDUȘ[1], Narcis BÂRSAN[1], Oana IRIMIA[1]

[1]Department of Environmental Engineering and Mechanical Engineering,
„Vasile Alecsandri" University of Bacău
[2]DIATI, Politecnico di Torino, Italy
e-mail: cochiorca_alina@yahoo.co.uk

ABSTRACT

The study purpose is to analyze the heavy metals concentrations in the water from the Buhoci area wells and to evaluate the physico-chemical parameters of this water. Measurement of physico-chemical parameters were performed on site in five locality points using portable equipment. Heavy metals from these samples were analyzed in the laboratory of Hydrogeology, Politecnico di Torino, Italy. The analyzed water sources are used for domestic consumption. The results of the physico-chemical parameters comparative analysis fall within the limits admitted according to the requirements of Romanian Law no. 458 of July 8, 2002 with values in the range of: pH ≥ 6.5 - ≤ 9.5; turbidity (°C) ≤ 5; conductivity (µS/cm) ≤ 2,500.

KEYWORDS: heavy metals, physical-chemical analyzes, drinking water

1. Introduction

From the total quantity of water on the surface of the earth it results that 99% is not available to be used. And the percentage of 1% is stored in the earth. In most countries, groundwater and surface waters are the main sources of fresh water that can be used for domestic and irrigation purposes. A particular importance for citizens is the evaluation of drinking water quality to determine if it is adequate for consumption [1-7].

Natural waters, irrespective of their origin, contain many impurities, of a mineral and organic nature, dissolved or dispersed, in a higher or lower concentration, which they carry in the course of natural circulation [1-3, 8].

Water from natural sources presents various qualitative aspects. To determine the quality of the water, there can be examined the organoleptic, physical, chemical, biological and bacteriological properties on the basis of field, at the source site and laboratory analyzes [1-3, 8].

Groundwater is generally characterized by a high mineralization, the dissolved mineral salts content is more than 400 mg/L and particularly formed chlorides and sulfates of sodium, potassium, calcium and magnesium [8].

The concentration of hydrogen ions is around neutral, corresponding to a pH of 6.5 ÷ 7.0. From the dissolved gases predominate free carbon dioxide, the oxygen content being very low below 3 mg O_2/L [8, 9].

Depending on the mineralogical composition of the areas, some groundwater sources contain significant quantities of iron, manganese, hydrogen sulfide and sulphides, nitrogen compounds [8, 9].

Groundwater is formed up of a number of primary ions, which form compounds. These ions are sodium, potassium, magnesium, calcium, manganese and iron. Because of the cations, which are found in water combined with an anion, they can form salt compounds. The main anions are sulfate, chloride, acid carbonate and carbonate [10].

From an economic point of view, groundwater is much cheaper than surface water because there is no need to construct the reservoirs. Groundwater is usually of good quality, without solid suspensions (except for limited areas where pollution was affected) without bacteria and other pathogens [10].

Groundwaters are not just meant to be captured for supply. They have a significant contribution for supply by discharge into the river, either as a base flow or as a spring [10].

The level of water in fountains in particular areas is decreasing year after year. Due to water

supply with the both for drinking and for agriculture and industry, many streams dry out. The quality of drinking water that can come from groundwater sources is important for those who are supplying through drilling or wells [10].

In some regions, groundwater and surface water can be contaminated with heavy metals (lead, mercury and arsenic in large quantities) that can get into the body and can cause certain consequences. Just if it causes some consequences, these metals in small quantities are necessary in the body for human health. Besides the heavy metal pollution of water, it can also be polluted with nitrites and nitrates, microorganisms and organic pollutants [11-16].

The present study has been realized in the locality Buhoci in Bacau county, Romania. The study purpose is to analyze the heavy metals concentrations in the water from the Buhoci area wells and to evaluate the physico-chemical parameters of this water.

2. Study area, materials and methods

2.1. Study area

The Buhoci locality is situated 46º 57' N latitude and 27º 02' longitude E. It is located in the central - eastern area of Bacău County, with a distance of 15 km from the city of Bacau [17].

The Buhoci locality, from the point of view of geographic location, is situated in the temperate area with a strong continental influence. Along the wide corridor of Siret and Bistrita, the cold air enters from N and from the mountainous region [17].

The average annual temperature in the locality is 9.1 °C, which varies from year to year. Precipitation is influenced by temperature, humidity of the air and wind. The most abundant precipitation is in summer, followed by spring and autumn. Decrease in precipitation in winter is due to cold and dry continental air in winter and Asian anticyclone [17].

Figure 1 represents the location of the study area, exactly Buhoci locality [18].

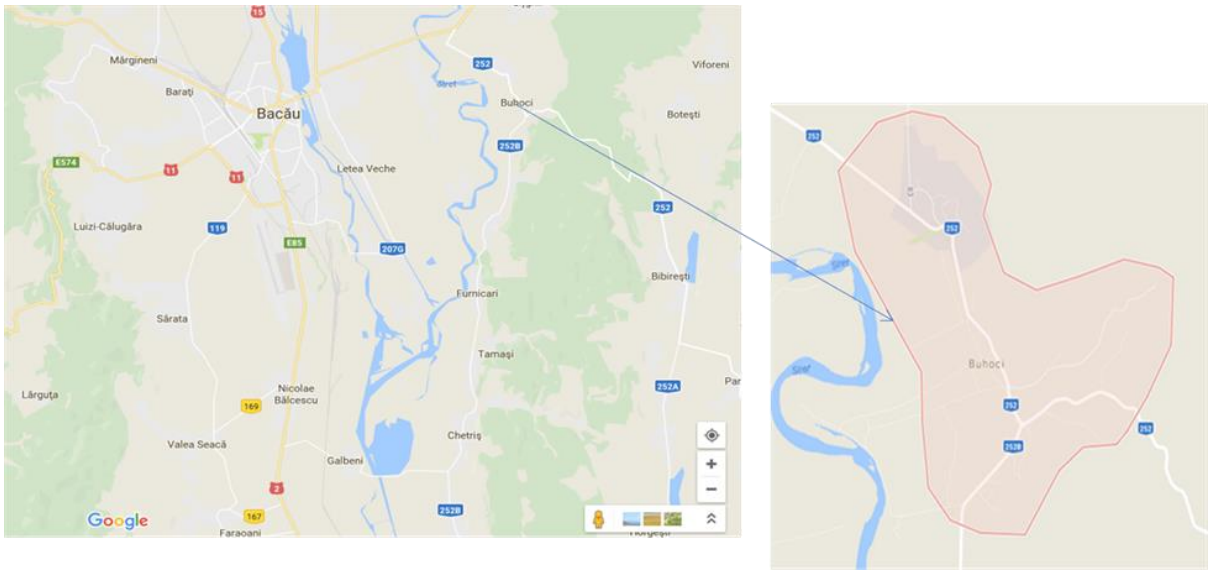

Fig. 1. *Location of the study area* [18]

2.2. Materials and methods

2.2.1. Sampling

For analysis of physico-chemical and heavy metals properties, 5 sampling points (Figure 2) were located using Global Positioning System (GPS), table 1. Water samples were collected in March using plastic containers. For every sampling point was collected every 500 mL of the sample.

2.2.2. Analysis of physico-chemical parameters and metals

Measurement of physico-chemical parameters were performed on site in five locality points using portable equipment. Heavy metals from these samples were analyzed in the laboratory of Hydrogeology, Politecnico di Torino, Italy.

The analysis of metals Na, K was realized using the AA-6800 Atomic Absorption Spectrophotometer. Ca, Mg and HCO_3 were determined by titration

method using the Metrohm 809 Titrando equipment, and the other metals were analyzed using Inductively Coupled Plasma Mass Spectrometry.

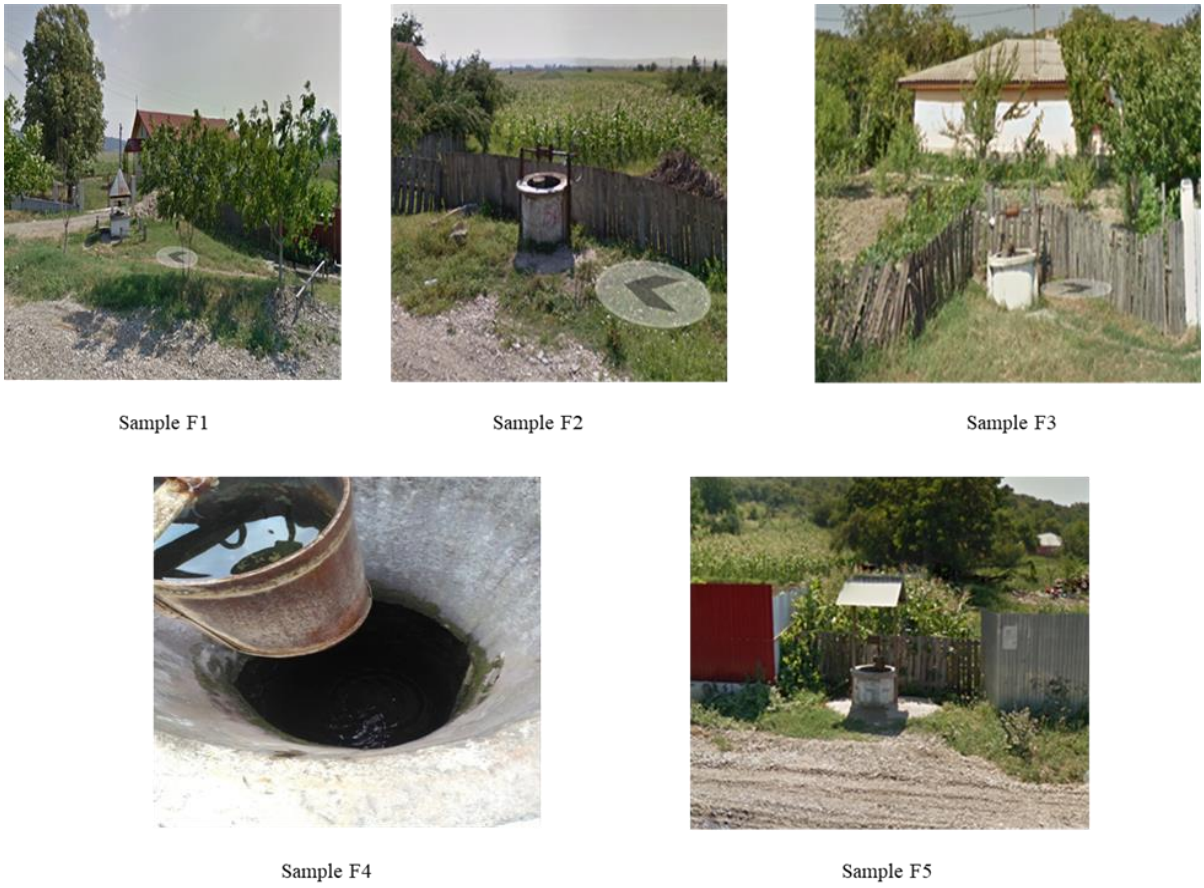

Fig. 2. *Sampling points for analysis* [19]

3. Results and discussion

3.1. Physico-chemical parameters

Physical and chemical parameters analyzed from water samples collected from the wells in March were conductivity, temperature, pH, turbidity, salinity and dissolved oxygen (Table 2).

The admissible limit values of physico-chemical parameters in drinking water according to Law no. 458 of July 8, 2002 updated in 2017 are presented in Table 1.

Table 1. *Limit values permitted for physico-chemical parameters in drinking water* [20]

Nr. crt.	Measured parameters	Maximum Admissible Concentration
1	pH	≥ 6.5; ≤ 9.5
2	Turbidity (NTU)	≤ 5
3	Conductivity (µS/cm)	≤ 2.500
4	Nitrites (mg/L)	0.50
5	Nitrates (mg/L)	50
6	Dissolved oxygen (mg/L)	5

Physico-chemical parameters differ significantly from the sampling samples so that the pH values of the five samples analyzed are easy alkaline (Figure 3) with a pH major than 7, with exception of sample number 1 (F1).

Table 2. *Physico-chemical parameters of water in the locality Buhoci*

No.	Sampling points	Date	pH	O_2 (mg/L)	Temp °C	Turbidity (NTU)	Salinity °C	Conductivity (µS/cm)	Nitrites (mg/L)	Nitrates (mg/L)	Geographical coordinates
1	F_1	March 30, 2017	7	4.7	10.7	4.21	0.6	1647	0.000	110.26	N 46°34'44,7276'', E 27°0'27,828''
2	F_2	March 30, 2017	7.4	5.8	10.5	3.65	0.8	1608	-	-	N 46°34'45''/ E 27°0'28''
3	F_3	March 30, 2017	7.4	3.5	11.5	0.71	0.7	1522	-	-	N 46°34'13''/ E 27°0'56''
4	F_4	March 30, 2017	7.5	4.5	9.2	1.64	0.6	1290	-	-	N 46°33'59''/ E 27°1'9''
5	F_5	March 30, 2017	7.28	3.9	9.8	1.11	0.5	1228	0.000	62.77	N 46°34'7''/ E 26°59'55''

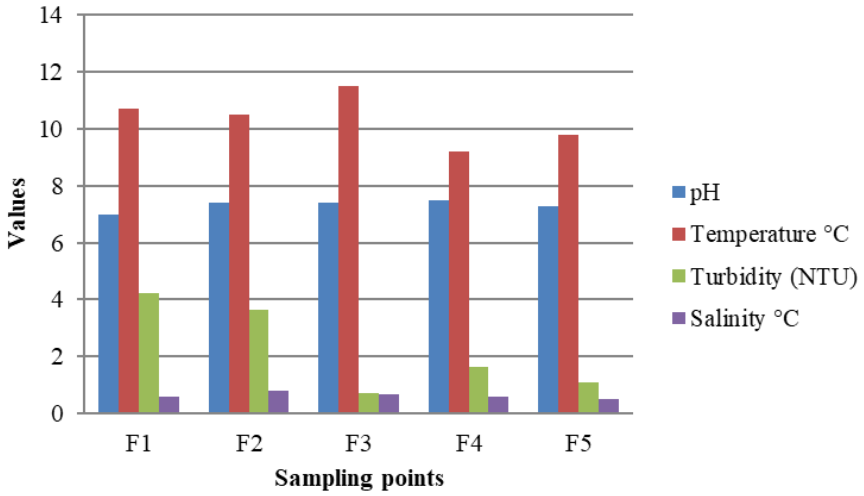

Fig. 3. *Parameter values in water samples*

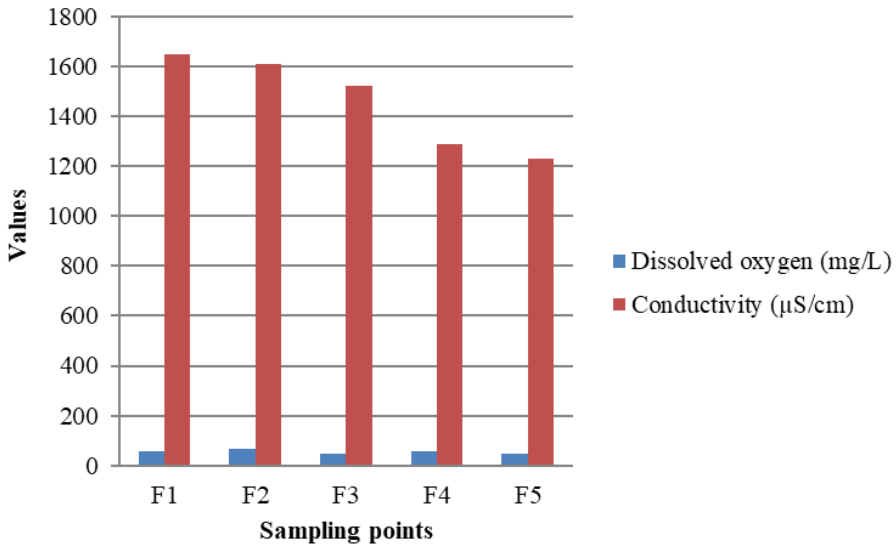

Fig. 4. *Parameter values in water samples*

The turbidity values (Figure 3) of the 5 samples collected from the wells in Buhoci varies between 0.71-4.21 NTU. The highest value is recorded in the sample number 1 (F1) due to disturbance of the soil during the withdrawal of water.

The quantity of dissolved oxygen (Figure 4) is higher in sample 2 (F2) than the other sampling points (Figure 4), because it depends on pressure, alkalinity and temperature (Figure 3).

The results of water conductivity analyses indicate that this parameter falls within the limits allowed by law for all collected samples. Conductivity values varies between 1228 - 1647 µS/cm.

3.2. Concentration of metals in drinking water

The maximum permissible limits of heavy metals in drinking water on the Law no. 458 of July 8, 2002 updated in 2017 are presented in Table 3.

Table 3. *Limits admitted in drinking water of heavy metals* [20]

Metals in water	**Limits admitted in drinking water of metals**	
	Values accepted	**Analysis method**
Cu mg/L	0.1	STAS 3224/69
Pb µg/L	10	STAS 6362/85
Fe g/L	200	STAS 3086/68 SR 13315/96 SR ISO 6332/96
Zn g/L	5000	STAS 6327/81
Mn µg/L	50	STAS 3264/81 SR 8661-1,2/96 SR ISO 6333/96
Al g/L	200	STAS 6326/90
As µg/L	10	STAS 7885/67
Se µg/L	10	STAS 12663/88
Cd µg/L	5	STAS 11184/78

The analysis of the heavy metals in the water from the wells in Buhoci was done for sample 1 (F1) and sample number 5 (F5), because these water sources are much more usable. In Table 4 are shown the analysis of metals in water samples analyzed in the hydrogeological laboratory of the Politecnico di Torino.

Table 4. *Heavy metals concentration in water samples*

Sample	**Heavy metals concentration**								
	Cu mg/L	**Pb** µg/L	**Fe** g/L	**Zn** g/L	**Mn** µg/L	**Al** g/L	**As** µg/L	**Se** µg/L	**Cd** µg/L
F1	0.00347	15.62	0.0000275	0.001455	6.311	0.003421	0.488	33.84	0.08
F5	0.00980	3.621	0.00001434	0.001761	0.782	0.001857	7.518	25.23	0.028

The concentration of Pb in sample number 1 (F1) exceeds the maximum permissible limit of metals in drinking water (Figure 5) according to Law no. 458 of July 8, 2002. The quantity of Selenium (Se) for the two samples of water exceeds the legal limit in drinking water of 10 µg/L, the value being 33.84 µg/L (Table 4). The rest of the metals in the analyzed samples (Cu, Fe, Zn, Mn, Al, As and Cd) do not exceed the limits, falling below the maximum allowed by the law.

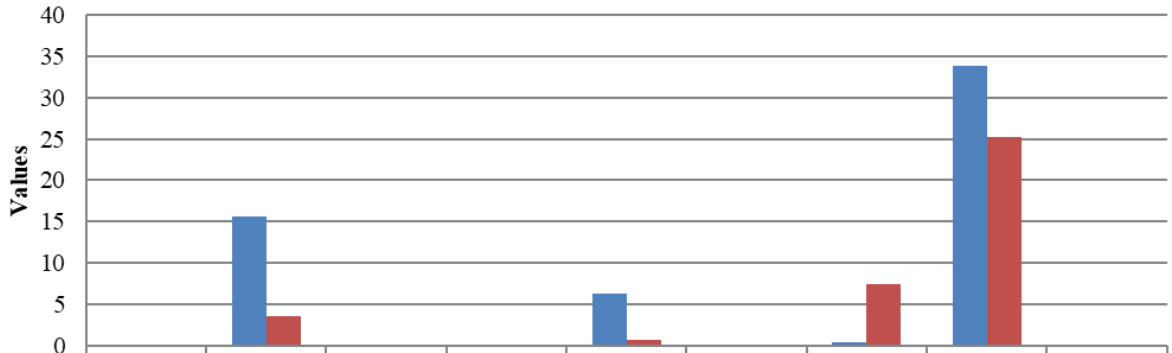

	Cu mg/L	Pb µg/L	Fe g/L	Zn g/L	Mn µg/L	Al g/L	As µg/L	Se µg/L	Cd µg/L
F1	0.00347	15.62	0.0000275	0.001455	6.31	0.003421	0.49	33.84	0.08
F5	0.00980	3.62	0.0000143	0.001761	0.78	0.001857	7.52	25.23	0.028

Fig. 5. *Values of metal concentrations in water samples*

4. Conclusions

This study was accomplished to evaluate physico-chemical parameters of water and to estimate the concentrations of metals in the water from the wells in the Buhoci area. From the analysis made it is to be seen that, the physical and chemical quality of water in the analyzed samples is good. The nitrite values in the analyzed water are zero, instead, the quantity of nitrates in the analyzed samples exceeds with much the maximum allowed by law. The concentration of nitrates in the wells can be due to the failure to comply and composition of the soil.

About the metals analyzed from drinking water coming from Buhoci locality, it results that they are below the limits allowed by law except for Pb, which is much over the limits admissible and Se.

References

[1]. Barsan N., Nedeff V., Temea A., Mosnegutu E., Chitimus A. D., Tomozei C., *A perspective for poor wastewater infrastructure regions: a small-scale Sequencing Batch Reactor treatment system*, Chemistry Journal of Moldova, vol, 12, no. 1, p. 61-66, 2017.

[2]. Barsan N., Nedeff V., Mosnegutu E., Panainte M., *Heat balance components of a small Sequencing Batch Reactor applied for municipal wastewater treatment*, Environmental Engineering & Management Journal, vol. 11, no. 12, p. 2133-2140, 2012.

[3]. Tirtoaca Irimia O., Tomozei C., Panainte M., Mosnegutu E. F., Barsan N., *Efficiency of filters with different filtering materials: comparative study in water treatment*, Environmental Engineering & Management Journal, vol. 11, no. 12, p. 2133-2140, 2012.

[4]. Ross Sadler, Brooke Maetam, Benjamin Edokpolo, Des Connell, Jimmy Yu, Donald Stewart, Park M.-J., Darren Gray, Budi Laksono, *Health risk assessment for exposure to nitrate in drinking water from village wells in Semarang*, Indonesia, Environmental Pollution, vol. 216, p. 738-745, 2016.

[5]. Jie Liu, Nesy Daniel, Dorjderem Amarbayasgalan, Jinhua Fu, Xiaohui Lei, Huajie Liu, Darryl Macer, Qingju Qiao, Amy Sun, Keisuke Tachiyama, Yi Zheng, *Water Ethics and Water Resource Management*, 2009, http://www.unescobkk.org/fileadmin/user_upload/shs/Energyethics/EETAP14rpt.pdf>, accessed in 18.10.2017.

[6]. Muhammad Balal Arain, Ihsan Ullah, Abdul Niaz, Nasrullah Shah, Afzal Shah, Zahid Hussain, Muhammad Tariq, Hassan Imran Afridi, Jameel Ahmad Baig, Tasneem Gul Kazi, *Evaluation of water quality parameters in drinking water of district Bannu, Pakistan: Multivariate study*, Sustainability of Water Quality and Ecology, vol. 3-4, p. 114-123, 2014.

[7]. Sotirios Karavoltsos, Aikaterini Sakellari, Nikolaos Mihopoulos, Manos Dassenakis, Michael J. Scoullos, *Evaluation of the quality of drinking water in regions of Greece*, Desalination, vol. 224, p. 317-329, 2008.

[8]. Oana Țîrțoacă (Irimia), Mirela Panainte, Gabriel Lazăr, Valentin Nedeff, *Potabilizarea apelor. Procedee și tehnici de filtrare*, Ed. Alma Mater, Bacău, 2014.

[9]. Băloiu V., *Gospodărirea apelor*, Ed. Didactică și pedagogic, București, 1971.

[10]. Gray N. F., *Drinking water quality. Problemes and Solutions*, Second edition, Cambridge Uninersity Press, 2008.

[11]. Duruibe J. O., Ogwuegbu M. O. C., Egwurugwu J. N., *Heavy metal pollution and human biotoxic effects*, International Journal of Physical Sciences, vol. 2 (5), p. 112-118, May 2007.

[12]. Lebea N. Nthunya, Monaheng L. Masheane, Soraya P. Malinga, Edward N. Nxumalo, Bhekie B. Mamba, Sabelo D. Mhlanga, *Determination of toxic metals in drinking water sources in the Chief Albert Luthuli Local Municipality in Mpumalanga, South Africa*, Physics and Chemistry of the Earth, vol. 100, p. 94-100, 2017.

[13]. Fabián Fernández-Luqueño1, Fernando López-Valdez, Prócoro Gamero-Melo, Silvia Luna- Suárez, Elsa Nadia Aguilera-González, Arturo I. Martínez, María del Socorro García- Guillermo, Gildardo Hernández-Martínez, Raúl Herrera-Mendoza, Manuel Antonio Álvarez- Garza, Ixchel Rubí Pérez-Velázquez, *Heavy metal pollution in drinking water - a global risk for human health: A review*, African Journal of Environmental Science and Technology, vol. 7(7), p. 567-584, 2013.

[14]. Bing Wu, Yan Zhang, Xuxiang Zhang, Shupei Cheng, *Health Risk from Exposure of Organic Pollutants Through Drinking Water Consumption in Nanjing, China*, Bull Environ Contam Toxicol, vol. 84, p. 46-50, 2010.

[15]. Shakhawat Chowdhury, Jafar Mazumder M. A., Omar Al-Attas, Tahir Husain, *Heavy metals in drinking water: Occurrences, implications, and future needs in developing countries*, Science of the Total Environment, vol. 569-570, p. 476-488, 2016.

[16]. Abdulrahman I., Alabdula'aly, Mujahid A. Khan, *Heavy metals in cooler waters in Riyadh, Saudi Arabia*, Environ Monit. Assess, vol. 157, p. 23-28, 2009.
[17]. ***, http://www.cadrul-natural-localitatea-Buh933.php, accessed in 04.10.2017.
[18]. ***, https://www.google.ro/maps/place/Buhoci, accessed in 04.10.2017.
[19]. ***, https://www.google.ro/maps, accessed in 04.10.2017.
[20]. ***, Legea nr. 458/2002 privind calitatea apei potabile.

THE ANNALS OF "DUNAREA DE JOS" UNIVERSITY OF GALATI
FASCICLE IX. METALLURGY AND MATERIALS SCIENCE
N°. 4 - 2017, ISSN 1453-083X

RESEARCES ON TREATMENT STATION AND THE SEWAGE NETWORK IN THE VILLAGE GHIDIGENI, GALATI

Stela CONSTANTINESCU
"Dunarea de Jos" University of Galati
e-mail: constantinescu_stela@yahoo.com

ABSTRACT

The population of the village is entitled to use the water supply, either through direct connections to the system, with drinking fountains in the yards or through network drinking fountains located in the street.

The commune has its water supply, water source through deep drilling and storage tanks. Household wastewater through its contents is not dangerous and their flow is 5 l/s. The activity will have a positive impact in that they will collect household wastewater from households, while preventing groundwater pollution.

Sewage network will be made of PVC pipes ready for SN2 main collectors having DN 315/400 mm. Sewage pipes will be buried on a bed of sand, about 10 cm thick. Pipes and fittings that make up the network of sewers are resistant to most chemicals present in aqueous solutions.

For wastewater treatment there are disagreements regarding the large installation. This is valid even in the case of legal amendments or conditions caused by exploitation, technical concepts and procedures that will ensure the greatest possible flexibility of the sewage treatment plant.

KEYWORDS: wastewater, groundwater, sewage network, broadband, wastewater treatment

1. Introduction

The main objective of the wastewater treatment is the removal of suspended substances, colloidal and in solution, toxic substances, microorganisms, etc. of the wastewater, in order to protect the environment (air, soil, emissary, etc.).

Discharges of unused or improperly treated wastewater may harm public health. In this line of ideas STAS 1481 provides for the wastewater to be discharged downstream of the points of use.

Wastewater treatment plants are the set of constructions and installations where sewage is subject to technological purification processes that alter its qualities so as to meet the prescribed conditions for receiving and dispatching substances retained in these waters.

Nowadays, treatment plants can be classified into two groups: urban and industrial.

Industrial wastewater treatment plants treat only industrial wastewater, while municipal wastewater treatment plants receive, in varying proportions, domestic sewage, meteoric, drainage and surface water treatment plants [1, 2].

Municipal wastewater treatment with industrial wastewater is sometimes advantageous. The existence of a single wastewater treatment plant, where both industrial and urban waters are treated, can reduce the cost of water treatment production and more efficient cooperation between industry and the populated center for wastewater treatment.

In view of the treatment of wastewater and the reduction of the cost of treatment, besides the measures taken by pre-treatment of waste water, the following must be taken into account: irrigation of urban or industrial wastewater, purification process leading to crop growth; recirculation of treated wastewater, resulting in reduced investment in water treatment and treatment plants; retention and reuse of valuable substances, driven by wastewater (wood fibers, petroleum products, etc.) or resulting in water treatment (sludge, gas, etc.), the replacement of some degradable substances, which are part of the technological process of some industries, with others, more easily degraded, to simplify the treatment process and reduce cleaning costs; the use of self-cleaning capacity for emissions, to reduce sewerage facilities, etc.

Advanced sewage treatment is defined by the set of additional operations following secondary conventional scrubbing with the purpose of removing suspended and dissolved substances left in the water after passing the classical steps. Advanced treatment includes processes and technologies designed to provide high purification rates that cannot be achieved by classical methods and/or to remove pollutants in the physical and biological stages [3-6].

Advanced sewage treatment is mandatory, being required by the need to maintain ecological balance.

The impact of wastewater on the environment must be analyzed both in terms of the consequences of carbon dioxide spillage and the changes that may occur in the emissary as a result of nitrogen and phosphorus compounds. At the same time, the effect of other compounds, such as those toxic, which are accidentally discharged or conducted into natural waters, should also be analyzed.

Advanced sewage treatment is introduced into the treatment technology when it is necessary to obtain high quality water, which cannot be achieved through biological processes, to protect the environment, to avoid eutrophication downstream of the discharge point the purpose of using reused water or when the emissary is used as a source of supply to some localities [7, 8].

For the choice of processes and technology as a whole, it is necessary to consider: the self-purification capacity of the natural course in which effluent discharge takes place; water treatment costs for the purpose of potable water treatment in the case of catchments downstream of the effluent discharge point; the costs of constructions and installations related to the proposed technology, the costs of exploiting and controlling the quality of the effluent discharged; energy requirements for the operation of facilities and equipment related to the proposed technology [9].

2. Experimental procedure

The organic matter retained in the mechanical separators and the primary decanter together with a part of the secondary decant deposition are passed to the plant called tank and subjected to an anaerobic fermentation process.

Unpalatable odorous volatile substances resulting from enzymatic hydrolysis of organic substances and lipids and counterparts are converted into methane gas and carbon dioxide. The residue obtained in the methane, the sludge is dehydrated from the drying layers, resulting in a largely mineralized and generally inactive product.

Most sewage treatment plants have a close-fitting schematic diagram, the difference being made by the dimensions and technologies used.

In the composition of a treatment plant, we distinguish the following steps: a primary, mechanical; a secondary, biological, and a tertiary, biological, mechanical or chemical stage at some stations (Figure 1).

The characteristics of wastewater can be: physical, chemical and biological. (Fig. 2). The physical characteristics are: the urban wastewater temperature is usually 2 to 3 °C higher than that of the supply water and this is a decisive factor in the wastewater treatment.

Turbidity of wastewater and emissivity only indicates the content of suspended matter because there is no well-defined relationship between turbidity and suspension content. Turbidity is measured in degrees on the silica scales and is determined primarily for the emissive water and only occasionally for wastewater.

The scent of fresh wastewater is almost inexistent. The waters under fermentation have more or less pronounced odor of swollen eggs, depending on the fermentation stage in which they are found.

The color of fresh sewage is light gray; by fermenting organic matter from water, the color of the wastewater becomes darker.

With respect to chemical characteristics we can mention: dissolved oxygen (O_2) which is found in small quantities in wastewater (1-2 mgf/dm^3), but only when fresh and after biological treatment. Depending on the degree of pollution, surface waters contain higher or lower amounts of oxygen. If water contains the amounts of oxygen shown in Table 1, that water is considered to be saturated; above these values the water is over-saturated, and below these values, sub-saturated.

Biomedical Oxygen (CBO) consumption of wastewater or emissary is the amount of oxygen consumed for biochemical decomposition under aerobic conditions of total organic solids at standard temperature and time - 20 °C and 5 days respectively; In this case, the value is marked with CBO5 - biochemical oxygen demand at 5 days.

Oxygen deficiency is the amount of oxygen missing from water to reach the saturation value. To determine the degree of soiling of surface water, it is of great importance to know its oxygen content.

Chemical oxygen consumption (CCO) measures the carbon content of all organic matter categories by determining the oxygen consumed by potassium bicarbonate in acidic solution.

Biological characteristics are all the organisms present in the wastewater.

Table 1. *Oxygen depending on the water temperature*

Parameter	**Value**						
Temperature [°C]	0	5	10	12	14	16	18
O_2 in water [mgf/dm^3]	14.23	12.80	11.33	10.83	10.37	9.95	9.64
Temperature [°C]	20	22	24	26	28	30	
O_2 in water [mgf/dm^3]	9.17	8.83	8.53	8.22	7.92	7.63	

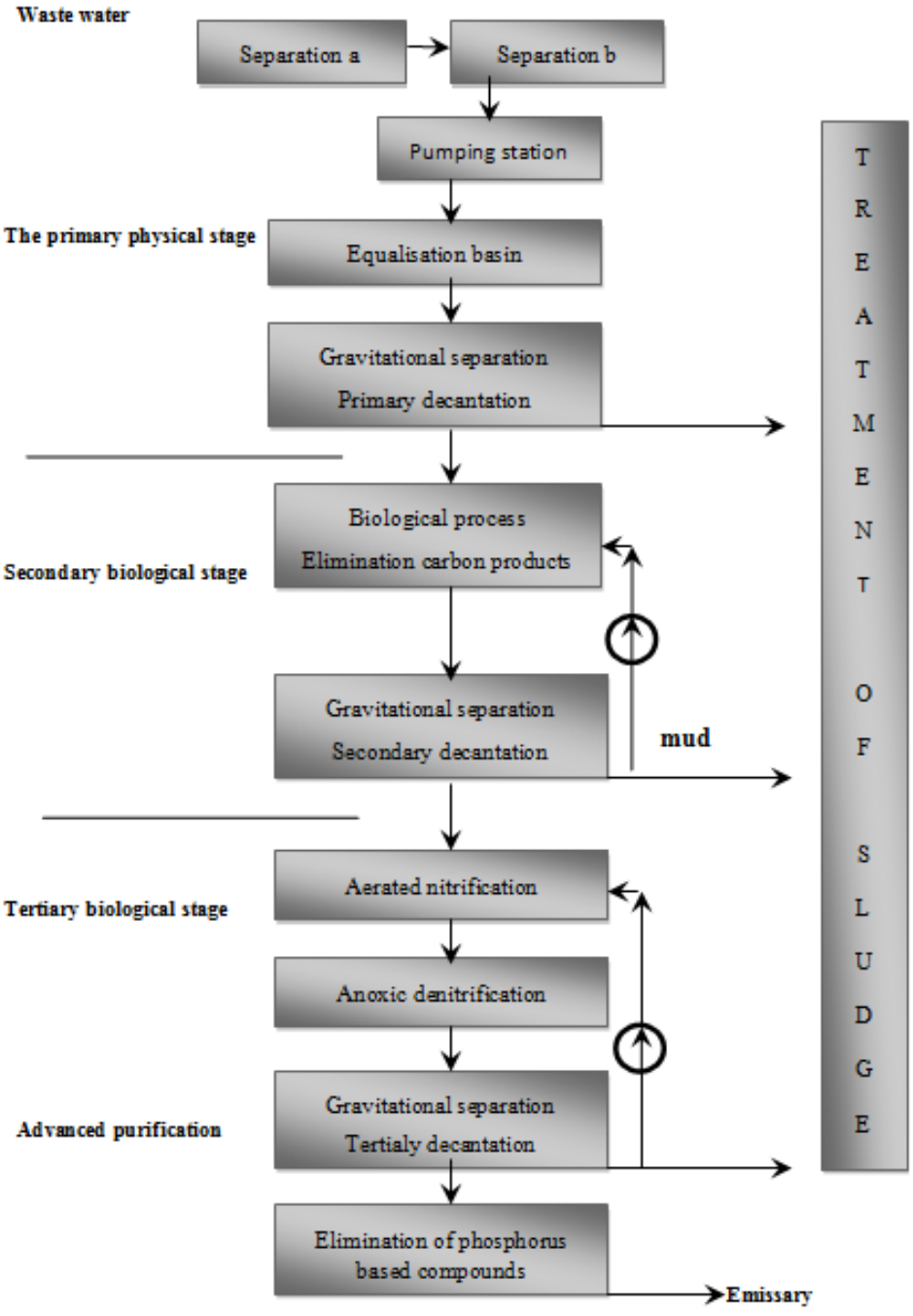

Fig. 1. *The general scheme of a treatment plant*

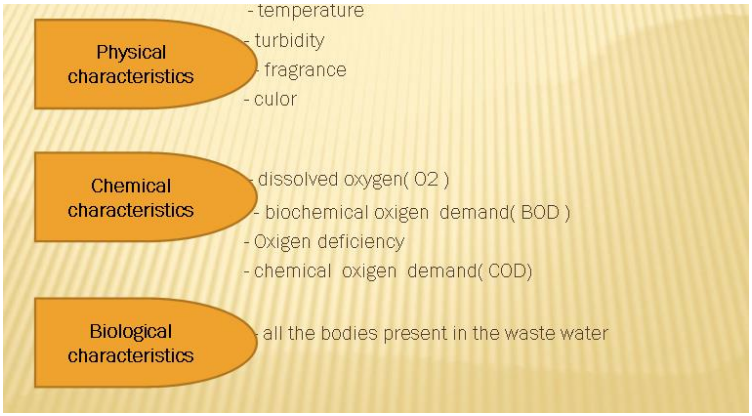

Fig. 2. *Characteristics of waste water*

Active sludge is the basic structural unit of the process. The term *activated sludge*, introduced by Arden and Locket, considers the cause and effect of self-purification of polluted, sufficiently aerated and agitated water in the presence of microorganisms. At a concentration of biomass in the aeration basin of 1000-8000 mg/l, in a properly conducted process, a biomass concentration in the sludge at the 6-15 g/l decanting outlet will result. The secondary decant in the scheme retains the active sludge with an efficiency of 25-80%; he cannot retain isolated microorganisms. The recycled sludge percentage is 25-200% of the treated flow rate. Active sludge contains species that in their common activity can metabolize the organic matter to carbon dioxide and water. Looking at the microscope, a flacon has a complicated structure characterized by a gelatinous mass secreted by microorganisms in which many bacteria and inert substances are contained; among the flocks live protozoa and some metazores.

There are two categories of sludge that interfere with the operation of activated sludge basins: recirculating sludge and excess sludge [Figure 3].

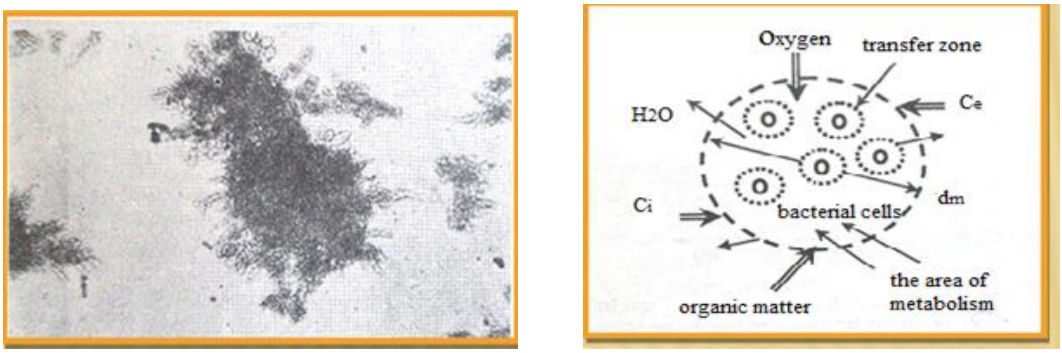

Fig. 3. a) Microscopic aspect of activated sludge b) Bottle with active sludge

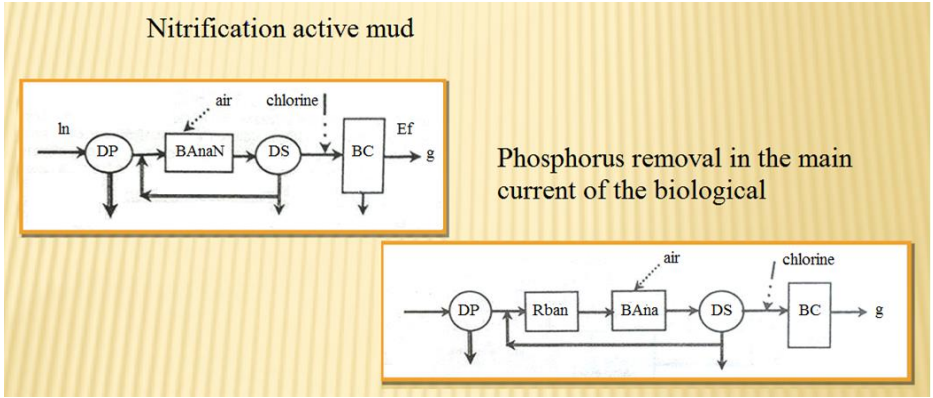

Fig. 4. *Technological schemes for advanced waste water treatment*

In activated sludge treatment plants, a balance must be struck between rapid mineralization of organic substances which requires rapid development of microorganisms and formation of flocs by concentrating live cells from the aqueous system at low cell growth rates. This balance is achieved by recycling the sludge retained in the secondary decanter.

Advanced sewage treatment is defined by a set of additional operations aimed at eliminating the suspended and dissolved substances remaining in the water after passing the classical steps. Technological schemes for advanced wastewater treatment are presented below (Figure 4).

Wastewater contains phosphorus compounds, an essential element of the plant's and animal's nutrients. Wastewater contains about 10-12 mg/l of phosphorus.

Phosphorus removal can be accomplished by chemical or biochemical reactions.

Osmosis can occur when there is a semipermeable membrane such as cell membrane. When a cell is submerged in water, water molecules cross the cell membrane from the low solvate zone to a high solvated zone. This process is called osmosis.

Osmosis is important in biological systems where many biological membranes are permeable. There are two types of osmosis: reverse osmosis and direct osmosis.

Reverse Osmosis produces clean, even "clean" (demineralized) water, and can be used for sewage treatment, potable water preparation (Figure 5).

The principle of operation of the process is a semi-permeable membrane through which water passes very easily from other substances less or not due to the size of the molecule.

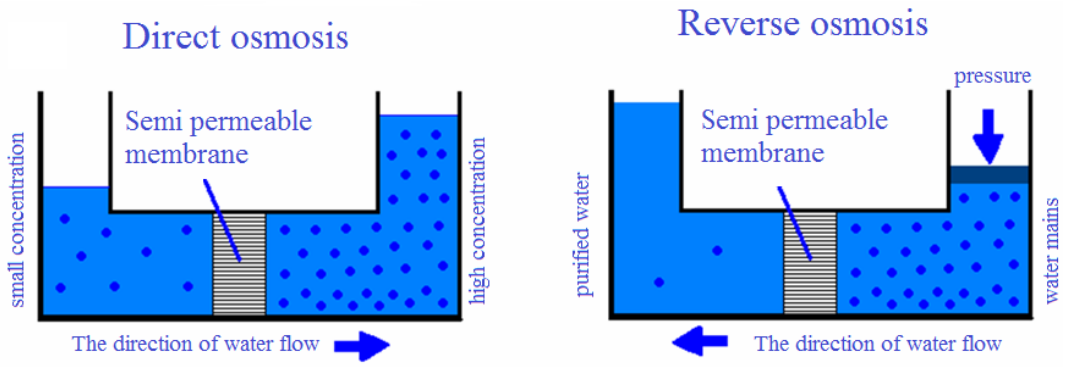

Fig. 5. *Osmosis*

3. Sewage treatment plant and sewerage network in the commune of Ghidigeni, Galati

Ghidigeni Commune is located in the north of Galati County, about 25 km north of Tecuci. The access to the locality is through a branch of the national road Tecuci - Bârlad - DN24 (www.proiect-galati.ro).

Existing water supply system has a water source with depth drilling and existing storage tanks 300 and 1 x R500, can ensure the flow in future distribution network expansions for the entire population of the commune.

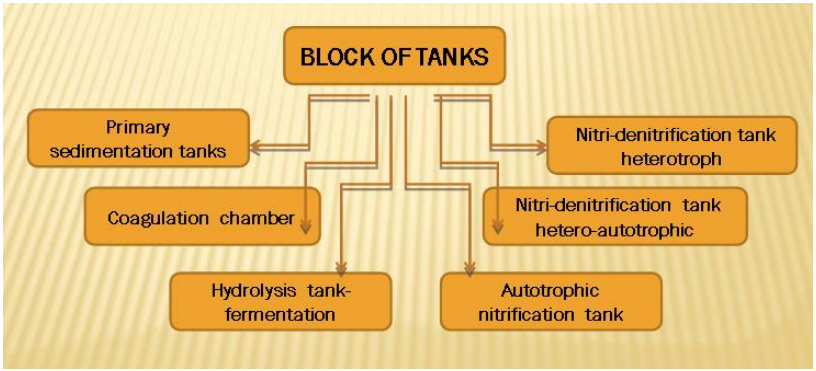

Fig. 6. *Biological treatment stage*

Domestic wastewater is pumped into the pressure and quench chamber and then into the switching house. From this, the wastewater gets gravitationally into the manure grate's home for retaining coarse solid matter and further gravitationally to the grease separator / separator. After the sand and fats are retained in the grease separator, the wastewater gets gravitationally into the equalizing, homogenizing and pumping basin. From here the water is pumped through the radiator shaft and the electromagnetic flowmeter into the mechanical grate attached to the RESETILOVS N3-CA1S-160-931 compact container type treatment N + P, and from here, in the biological and chemical treatment tanks block where organic, biodegradable substances and nitrogen and phosphorus compounds are removed.

The biological treatment step consists of a biological treatment module with two parallel treatment lines, type RESETILOVS N3-CA1S-160-931. N + P. This plant performs a very efficient mechanical and biological treatment, the process being automated and permanently controlled (Figure 6).

The sewerage network will be made of PVC pipe fittings SN2 for main collectors with DN 315/400 mm. The sewer pipes will be buried on a sand bed about 10 cm thick. The pipes and fittings that make up the sewer system have chemical resistance to most aqueous solutions.

In order to achieve the required degree of purification, it is proposed that the electro-pumps in the endowment of the technological objects be FLYGT type due to the reliability, the high energy efficiency, and the long service life.

The provision of advanced machinery and equipment is mandatory in order to achieve the desired cleaning efficiencies. The proposed technological solution includes state-of-the-art, low-energy, simple operation operations by applying a process-specific automation.

4. Conclusions

The wastewater treatment plant from the village of Ghidigeni, Galati county, is characterized by a simple but modern technology and high efficiency.

The village has its water supply system, a water source through deep drilling and storage tanks.

Domestic wastewaters are not hazardous and their flow rate is 5 l/s.

The sewerage network will be made of PVC pipe fittings SN2 for main collectors with DN 315/400 mm.

The sewer pipes will be buried on a sand bed about 10 cm thick. The pipes and fittings that make up the sewer system have chemical resistance to most aqueous solutions.

The introduction of the biological treatment step was made due to the very high content of organic matter present in the wastewater.

Implementing the three principles, i.e. recycling, recovery, non-degradation of quality, has a beneficial effect both on the environment and on the economic and productive aspect.

References

[1]. Ovidiu Ianculescu, Raluca Racovițeanu, Gheorghe Ionescu, *Epurarea apelor uzate*, Editura Tehnică București, 2005.
[2]. Diana Robescu, Attila Verestoy, Szabolcs Lanyi, Dan Robescu, *Modelarea și simularea proceselor de epurare*, Editura Tehnică București, 2004.
[3]. Lydia-Maria Vaicum, *Epurarea apelor uzate cu nămol activ; Bazele biochimice*, Editura Academiei Republicii Socialiste România București, 1981.
[4]. ***, http://www.scribd.com/doc/217214914/Caracteristicile-Apelor-Uzate.
[5]. ***, http://ro.scribd.com/105112785.
[6]. ***, http://www.energ.pub.ro/fisiere/master.
[7]. ***, http://www.scrigroup.com/geografie/ecologie-mediu/Epurarea-apelor-uzate- istoric-13936.php.
[8]. ***, http://www.scrigroup.com/geografie/ecologie-mediu/Epurare-biologica42188.php.
[9]. ***, http://www.ecomagazin.ro/o-noua-tehnologie-epurare-tertiara/.

THE ANNALS OF "DUNAREA DE JOS" UNIVERSITY OF GALATI
FASCICLE IX. METALLURGY AND MATERIALS SCIENCE
N°. 4 - 2017, ISSN 1453-083X

BIOCORROSION BEHAVIOR OF A DENTAL SHAPE MEMORY ALLOY

Carmela Gurau, Gheorghe Gurau*
"Dunarea de Jos" University of Galati, Faculty of Engineering,
Domnească Street, 47, RO-800008, Galati, Romania
*e-mail: gheorghe.gurau@ugal.ro

ABSTRACT

Designing shape memory alloys (SMAs) with suitable mechanical properties, playing a predominant role as functional biomaterials and targeted degradation behavior has been a goal in recent time. Biocompatibility within the human body environment is the essential requirement of metals and their alloys used in reconstructive surgery, such as dental implants. In this research, a cooper based SMA was proposed to replace the most common dental bronze, benefit of unique property of pseudo-elasticity. Therefore, alloys that performs well in the air being inert or passive, may suffer a severe corrosion in the body. Bio-corrosion is accelerated by aqueous ions inside the complex biomechanical system displayed by various parts of human body. The microstructure and bio-corrosion behaviors of the SMA alloy in NaCl aqueous solution have been systematically investigated for nine years. The surface morphology of the resulted specimens was investigated using scanning electron microscopy (SEM) equipped with an energy dispersive spectrometry (EDX). Electrochemical tests were conducted using simulated body fluid (SBF) solution.

KEYWORDS: metallic biomaterials, biocompatibility, corrosion, shape memory alloy and cooper based SMA

1. Introduction

Cu-based alloys, especially Cu-Al-Ni SMAs, are currently being developed as an alternative to the first worldwide known and used in a broad range of biological applications, Ti-Ni. They can exhibit good properties like a large super-elastic window as well as a small thermal hysteresis concomitant with the remarkably high corrosion resistance [1-6]. Furthermore, for a few years it has also been established that the pseudo-elastic and shape memory effects are very competitive, being an advantage over the expensive Ti-Ni SMAs [7]. During the quenching process of the Cu-Al-Ni SMAs, the martensitic transformation exhibited from β-phase to a close packed structure. In the CuAl13Ni4 alloy, two types of thermal induced martensites (β1 and γ1) prevail on this specific alloy composition. The memory properties occur based on crystallographic reversible thermo-elastic martensitic transformation being stable upon cycling in these ternary alloys [1, 7]. In recent years, Cu-Al-Ni shape memory alloys have attracted a lot of interests due to their high strength and good corrosion resistance. Since 2009, an SMA alloy of very close composition has been investigated as material for biomedical applications [8]. Cu–Al–Ni thin ribbons produced by rapid solidification in martensitic state suggest improvement of the corrosion stability and biocompatibility in vitro as compared with dendritic microstructure in cast state. The reason of this paper is to study bio-corrosion for the replacement of the CuAl11Ni4 (ORCAST or NPG brands) an alloy commonly used in dentistry, with an SMA of the same system, CuAl13Ni4. The content of 13 wt.% Al produced satisfactory shape memory properties: pseudo-elastic behavior - allows deformations at body temperature without exerting stress on the oral tissues and damping property - due to their shape recovery under tension and compression loading [9].

2. Experimental procedure

The research program has used samples made from CuAl13Ni4 polycrystalline shape memory alloy. The overall chemical composition was

determined by automatic spectrophotometry type Quantovac as: Cu balance, Al 12.88, Ni 4.00, Mn 0.09, Si 0.04, Sn 0.02, Pb 0.01 wt.%. The corroded specimen surfaces examined were in cast, quenched, rolled and extruded state. The proposed CuAl13Ni4 biomaterial was cast in the same mold prepared as for real dental pivot (ORCAST alloy) used in dentistry. The mold containing the hot pivot obtained by centrifugal casting was suddenly cooled in an ice-water container. By quenching, the dendritic structure has become martensitic allowing activation of memory properties. The specimens were immersed each into a glass container containing 0.5 L 0.9% NaCl physiological solution on the 11th of March 2008. The samples were maintained in the corrosion environment, in stagnant conditions at room temperature. The surfaces of the specimens were in state of technological condition, without any preparations, mechanical polishing or chemical etching. Surface morphology of samples was observed using an OLIMPUS BX51 microscope and a Phillips Quanta 200 scanning electron microscope (SEM) coupled with an EDX detector. The electrochemical corrosion of the dental pivot was studied in SBF (a solution that imitates human fluids) on a VoltaLab 21 Electrochemical System (PGP-201).

3. Results and discussion

Results, concerning morphological and structural characterization of surface corrosion are reported in terms of OM images and SEM-EDX date. The corrosion behavior of Cu-Al alloys showed that the addition of aluminum content slightly decreases pseudo-passive current density at the anodic potential [7] being involved in formation of barrier film of Al_2O_3, enhancing of corrosion resistance of these alloys. In this research we propose to increase the aluminum content with 2 wt.%. The main reason for the enhancement of corrosion resistance is formation on the alloy surface of a barrier film of hydrated aluminum oxide/hydroxide, which builds up quickly in salt water. In ternary Cu-Al-Ni alloy is considered that enhancement of corrosion resistance is given by the emergence of duplex layer composed of $Cu_2O{\cdot}Al_2O_3{\cdot}xH_2O$ [7, 8] thin and strongly adherent inner barrier Cu_2O. The existence of Ni leads to the improvement of corrosion resistance, grater with higher Ni content due to the incorporation of Ni into the thin and strongly adherent inner barrier Cu_2O protective film [9]. Ni also is considered to suppress diffusion of Al and Cu [8].

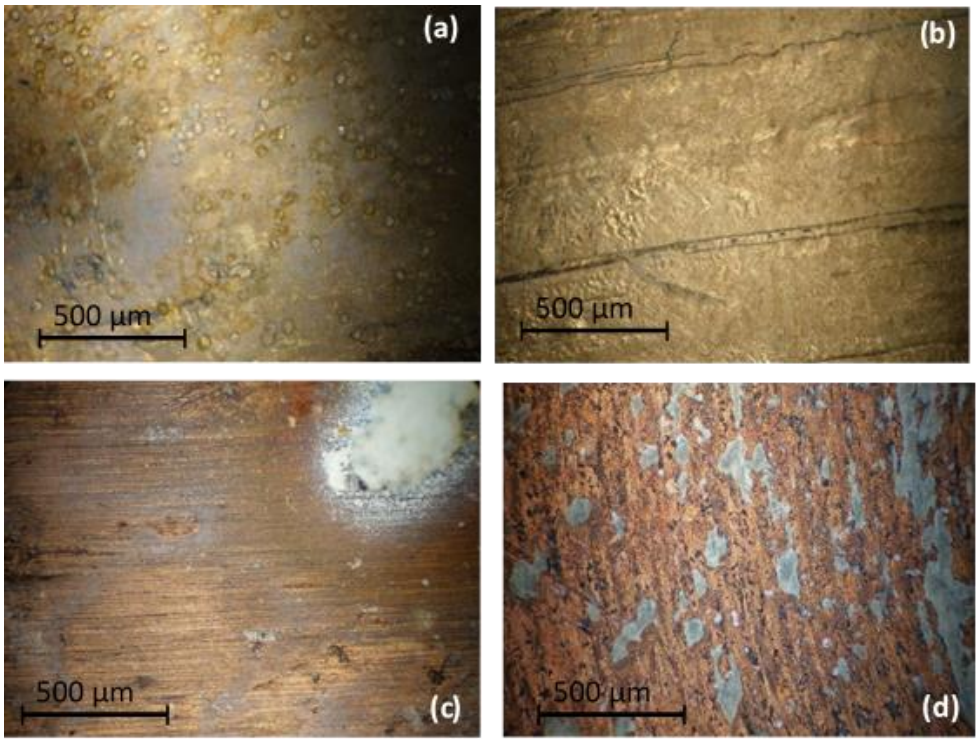

Fig. 1. *OM micrographs of CuAl13Ni4 shape memory alloy in martensitic state of surface after exposure for nine years in NaCl aqueous solution: a) quenched state; b) rolled; c) extruded and d) after electrochemical test in SBF*

Although the alloy is very homogeneous and chemically pure - prerequisite for shape memory properties, surface corrosion after exposure for nine years in NaCl aqueous solution, it is not uniform. The selective oxidation products appear to be specific copper oxide, red or turquoise, yellow (Figure 1c-d) [11]. The gray color is specific to aluminum passivation (Figure 1a). The green and blue colors are specific to nickel oxides and Ni_3Al precipitates in oxidized state (Figure 1a, c and d) [11]. Out of the more important ionic species, only Cl^- has an aggressive behavior in copper corrosion, especially in the "pitting" process. For bio-liquids in the oral cavity, aggressive type ions are much broader considering that a number of other ions enter this environment. In the cast state, as it is now used in dental technology, the alloy is more susceptible to corrosion than in martensitic state because of chemical inhomogeneity associated to dendrite structures [8]. The greatest part of the surface quenched sample is light brownish CuO_2 and gray aluminum oxide, but with blue interpenetration from Ni oxides (Figure 1a). In some areas of specimens, the corrosion products were absent in particular in rolled state (Figure 1b). There can be viewed salt (NaCl) crystals in the form of white crystals colorless. Figure 1d presents the sample studied in SBF solution highlighting red-brownish cooper oxides in strings and gray areas of aluminum oxide. The Penetration Index of 12.11 μm/year, calculated based on linear polarization data, reveals a good stability compared to the behavior of 316L steel in the same solution, which is 438 μm/year [12].

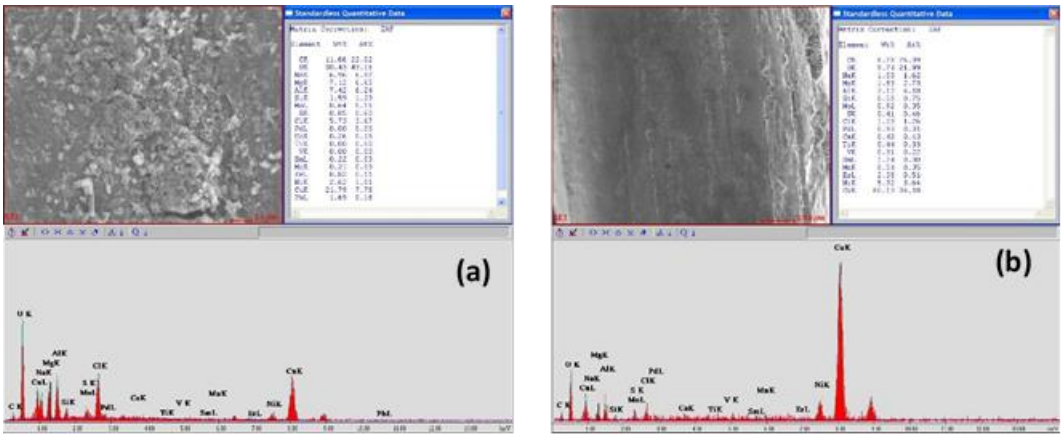

Fig. 2. *SEM-EDX images to typical surface corrosion of CuAl13Ni4 shape memory alloy surface after exposure for nine years in NaCl aqueous solution in quenched state-a) ensemble; b) detail from peripheral area*

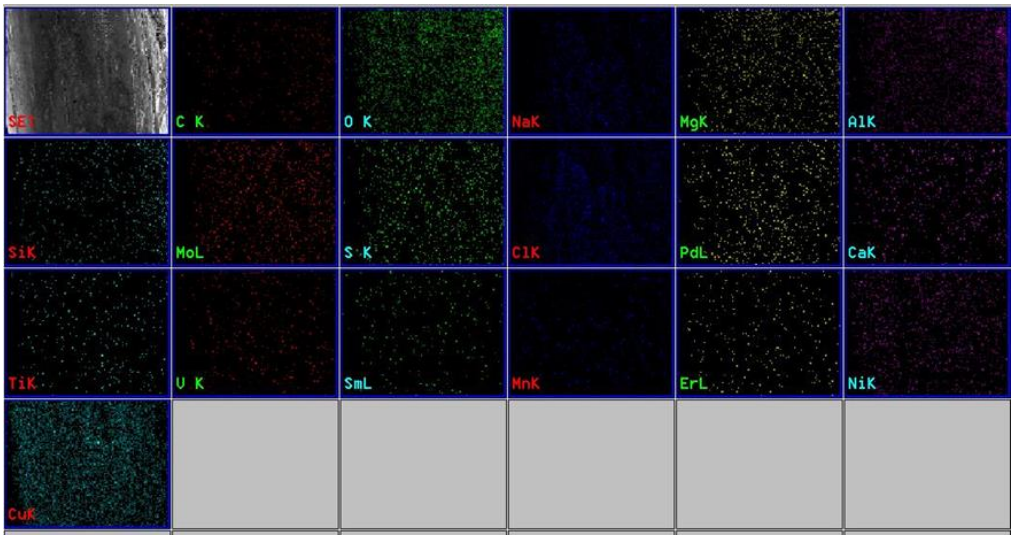

Fig. 3. *EDX spectrum of CuAl13Ni4 shape memory alloy surface after exposure for nine years in NaCl aqueous solution in quenched state: elemental map*

SEM observations (Figure 2) showed the morphology of oxidation $CuAl_{13}Ni_4$ shape memory alloy surface after exposure for nine years in NaCl aqueous solution in quenched state on which fine and ordered structure was allowed, being chemical homogenous. The area viewed in Figure 2a presented EDX highest picks for oxygen, aluminum, chlorine and sodium, but cooper pick reaches only 21.79%. The enlarged detailed image b presented EDX highest picks for cooper and oxygen, most probably porous Cu_2O film. The elemental mapping regions from Figure 2b and corresponding mappings of elements are presented in Figure 3. EDX spectrum of CuAl13Ni4 shape memory alloy surface after exposure for nine years in NaCl aqueous solution in quenched state as qualitative analysis identify Cu, Al and Ni elements showing a fairly uniform distribution. It is obvious that the oxygen reached areas are present only on the corroded surface indicating the formation of oxide layer. Chlorine and sodium atoms are dispersed on surface, too.

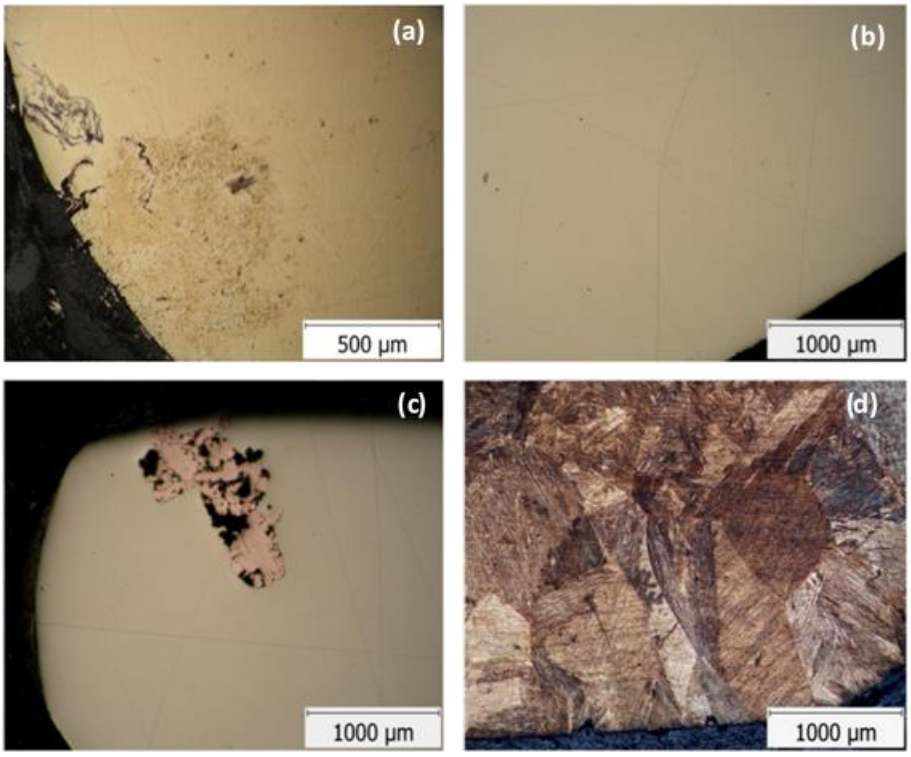

Fig. 4. *OM micrographs of CuAl13Ni4 shape memory alloy the surface cross section after exposure for nine years in NaCl aqueous solution: a) cast state; b) and c) quenched; d) etched with $FeCl_3$ in quenched state*

In Figure 4 is presented the surface cross section after almost 8 years for cast state and quenched samples. The mainly surface cross section aspect of all sample studied looks almost uncorded except dendritic, eutectoid or structure with grain boundaries precipitate. As can be seen from images, initiation of corrosion process occurs on scratch remaining after processing. The crevice corrosion is manifested as a result of water capillarity action inside micro-cracks. The quenched dental pivot had good corrosion behavior as can be seen from Figure 4b and c. The only crevice allowed seepage under oxide film on grains boundaries and occasionally inside whole grains. The grains that are etched at grains boundaries became pink colored. When the gap is larger, an inside deep corrosion takes place. If the surface after processing would be polished as the dental technology requires, the corrosion resistant would be improved over the dendritic or eutectoid structure. The corroded sample in quenched state polished and etched with $FeCl_3$ reveals fine martensite needles inside large austenitic grains.

4. Conclusion

This study comes on a long term, about 9 years, and analyses corrosion behavior in NaCl aqueous solution of a $CuAl_{13}Ni_4$ shape memory alloy after casting, quenching and plastic deformation processes. The alloy highlights a good corrosion behavior in martensitic quenched state after centrifugal casting.

The OM, SEM, EDX reveal the protection of oxide films and initiation and growth of corrosion products. The study confirmed that centrifugal casting followed by quenching enables the production of $CuA_{13}Ni_4$ dental pivots with the shape memory effects which exhibit higher resistance to corrosion than a mould cast alloy ($CuAl_{11}Ni_4$) used in dentistry. The corrosion behavior of shape memory dental pivots in salt water may be improved by polishing the uneven surfaces.

References

[1]. Straumal B., Kilmametov A., Opez G. L., Opez-Ferre I. L., San Juan J., Hahn H., Baretzky B., *High-pressure torsion driven phase transformations in CueAleNi shape memory alloys*, 2017.

[2]. Nady H., Helal N. H., El-Rabiee M. M., Badawy W. A., *The role of Ni content on the stability of CueAleNi ternary alloy in neutral chloride solutions*, Mater. Chem. Phys., vol. 134, p. 945-950, 2012.

[3]. Sarı U., Aksoy İ., *Micro-structural analysis of self-accommodating martensites in Cu-11.92 wt.% Al-3.78 wt.% Ni shape memory alloy*, J. Mater. Process. Technol., vol. 195, no. 1-3, p. 72-76, Jan. 2008.

[4]. Sarı U., Kırındı T., *Effects of deformation on microstructure and mechanical properties of a Cu-Al-Ni shape memory alloy*, Mater. Charact., vol. 59, no. 7, pp. 920–929, Jul. 2008.

[5]. Wang Z., Liu X., Xie J., *Effects of solidification parameters on microstructure and mechanical properties of continuous columnar-grained Cu-Al-Ni alloy*, Prog. Nat. Sci. Mater. Int., vol. 21, no. 5, p. 368-374, Oct. 2011.

[6]. Dar R. D., Yan H., Chen Y., *Grain boundary engineering of Co-Ni-Al, Cu-Zn-Al, and Cu-Al-Ni shape memory alloys by intergranular precipitation of a ductile solid solution phase*, Scr. Mater., vol. 115, p. 113-117, Apr. 2016.

[7]. Saud S. N., Hamzah E., Abubakar T., Bakhsheshi-Rad H. R., *Correlation of microstructural and corrosion characteristics of quaternary shape memory alloys CuíAlíNiíX (X=Mn or Ti)*, Trans. Nonferrous Met. Soc. China, vol. 25, p. 1158-1170, 2015.

[8]. Oli M. Č., Rudolf R., Stamenkovi D., Anžel I., Vučevi D., Jenko M., Lazi V., Lojen G., *Relationship between microstructure, cytotoxicity and corrosion properties of a Cu-Al-Ni shape memory alloy*, Acta Biomater., vol. 6, p. 308-317, 2009.

[9]. Gurau G., Gurau C., *Copper Based Shape Memory Alloy a Modern Opportunity to Change Classic Casting Dental Alloys*, TMS2013 Supplemental Proceedings, 25 Feb 2013, USA, p. 999-1006.

[10]. Zhu J.-J., Li S.-H., Shen L.-N., Yang W.-L., Li Z., *Corrosion behavior of novel Cu−Ni−Al−Si alloy with super-high strength in 3.5% NaCl solution*, Trans. Nonferrous Met. Soc. China, vol. 27, p. 1096-1104, 2017.

[11]. Warthon J. A., Stokes K. R., *The influence of nickel-aluminium bronze microstructure and crevice solution on the initiation of crevice corrosion*, Electrochemica Acta, 53, p. 2463-2473, 2008.

[12]. West J., *Basic Corrosion and Oxidation of Metals*, Ellis Horwood Ltd., England, 1986.

THE ANNALS OF "DUNAREA DE JOS" UNIVERSITY OF GALATI
FASCICLE IX. METALLURGY AND MATERIALS SCIENCE
N°. 4 - 2017, ISSN 1453-083X

THE INFLUENCE OF THE TEMPERATURE REGIME ON THE MECHANICAL PROPERTIES OF THE THICK STEEL SHEETS FROM CARBON AND LOW-ALLOY STEELS, LAMINATED TO THICKNESSES LESS THAN 40 MM

Marian BORDEI, Carmen Penelopi PAPADATU
"Dunarea de Jos" University of Galati, Romania
e-mail: marian.bordei@ugal.ro

ABSTRACT

Steel remains the most used material in the machinery industry, the construction of oil and gas pipelines, etc. Hot rolling is no longer a simple means of obtaining the final geometry of products in the steel industry, but in some way leading to the lamination process, it is possible to obtain a given structure which gives the rolled products the desired mechanical characteristics.

In this paper we analyzed the technological parameters which influence the properties of the materials, the technological measures for obtaining the appearance and structure of the steels can be deduced.

KEYWORDS: temperature regime, mechanical properties, carbon alloy steel

1. Introduction

The level of mechanical and technological properties of hot rolled flat products is the expression of the combined action of chemical composition factors (including micro-alloying) and structure.

For a given chemical composition, the decisive role in obtaining a certain set of mechanical properties is the structural factor, especially since, depending on the way of conducting the manufacturing process, a wide range of types can be obtained on the finished product structures.

The structure obtained is the result of the cumulative action of all the technological and compositional factors involved in the production of flat products:

- the heating temperature for rolling;
- the degree of reduction applied;
- the cooling rate after rolling;
- final temperature of rolling.

When choosing the technological parameters of lamination, it is taken into account their influence on the structural changes that occur during deformation (dynamic recrystallization, static recrystallization, austenite grain growth, phase transformation).

From the analysis of the sizes that influence the properties of the materials, the technological measures for obtaining the appearance and structure of the steels can be deduced.

Modern molding processes allow the structure and the characteristics of the finished product to be controlled during the deformation processes.

The decrease of the lamination temperature implies, while the other factors (degree of deformation, rolling time) are constant, the reduction of the rate of recrystallization and the obtaining of a fine austenitic granulation and, under certain conditions, of a non-recrystallized austenite upon the background of which cooling forms a ferrite-perlite structure whose fineness will depend on the deformation temperature [1].

It is important to obtain a fine austenitic structure during roughing deformation. The total degree of roughing deformation is generally 60%, decreasing with lower heating temperatures. The last roughing pass must be as large as possible (within acceptable limits) and the rolling temperature should be as low as possible.

Each category of sheet is a particular case in which the chemical composition of the base metal and the lamination scheme must be defined to allow the desired mechanical properties to be obtained without further heat treatment.

Indeed, according to Petch's laws, the limit of elasticity and the transition temperature (resilience) improve when the ferrite grain size decreases.

Numerous papers have specified the optimal configuration of austenite before transformation

$\gamma \rightarrow \alpha$, the grains must be fine, homogeneous and hardened [3].

The lamination at controlled temperature, fixing the conditions of recrystallization and deformation of the austenite, allows obtaining such g grains. At high temperature, the deformations introduced to the lamination of the thick sheets are accompanied by a static recrystallization of the austenite.

In the case of higher temperatures, the grains may increase between each pass. In the case of intermediate temperatures, the grains are refined through successive deformations and recrystallizations. At low temperature the austenite recrystallizes slowly. From a lamination pass to another, the grain does not have time to recrystallize; it progressively prolongs resulting the development of ferrite germination sites (grain boundaries, deformation bands) [4].

The good practice of laminating at controlled temperature therefore requires precise determination of the temperatures at which deformations of the product are to be carried out.

2. Deviations of mechanical characteristics and technological properties

Mechanical characteristics and inappropriate technological properties may in general have the following causes:

- inappropriate chemical composition;
- defects of steel material;
- inappropriate conditions at plastic deformation or chemical treatment;
- inappropriate sample sampling (non-precision dimensions, unfinished surfaces, uninterrupted joints);
- incorrect test execution.

The main mechanical characteristics and technological properties, the more significant and frequent causes (in the hypothesis of a suitable chemical composition) are:

a. Low tensile strength: inappropriate chemical treatment; inappropriate fiber orientation; plastic deformation with a too small cut; discontinuities of the material; internal defects (breaths, cracks, non-metallic inclusions, porosity); steel burning; regional segregation.

b. High tensile strength: inappropriate chemical treatment; too low temperature at the end of plastic deformation; excessive cutting of the laminate section; internal stresses (caused, for example, by uneven cooling of the material).

c. Low resistance: insufficient degassing of steel; gross or non-homogeneous granulation; precipitation at the edge of grains; segregation; structure pronounced in strips; inappropriate fiber orientation; steel burning; material discontinuities; internal defects (breaths, cracks, non-metallic inclusions, porosity); too small ratio of reduction; inappropriate microstructure due to heat treatment; residual internal tensions; fragility on tempering.

d. Insufficient elongation: the causes of these defects are the same as those shown for low resilience, with the observation that the fibrous structure or non-metallic plastic inclusions disposed parallel to the sample axis do not significantly influence the reduction of the elongation and constriction.

e. Shock test: material discontinuity; internal defects (cracks or tears, puffs, traces or porosity); structural defects (trans-crystallization, coarse granulation, grain precipitation, segregation); improper heat treatment, steel burning.

In the case of a suitable chemical composition, the steel structure largely determines the properties of the laminated sheets. Mechanical characteristics and technological properties are strongly influenced by the internal stresses of the laminates, usually caused by non-homogeneous deformations in the section, by inaccurate rolling temperatures and too high cooling speeds, i.e. by non-observance of the technological instructions of the products delivered in laminated state. Mechanical features can be reshaped in these situations by appropriate heat treatments.

Requirements for mechanical and technological properties are particularly important, especially for some steels, such as for example the construction ones. In some cases, the required properties are obtained directly from the plastic processing of steel, or sometimes a thermal treatment is required.

Generally, rejects due to chemical composition are rare, especially when assembling new assortments for which no verified chemical compositions have not yet been established. In order to ensure the prescribed mechanical and technological properties, the steel from which the product is processed must be adequate; badly deoxidized steel and the presence of defects such as: nonmetallic clusters, strong segregation, shrinkages, cracks, may (depending on the defect intensity) reduce the properties to their permissible limit or cause the products reject.

3. Industrial experiments

The industrial experiments aimed at establishing the hot deformation regime of the thick sheets in order to modify the existing rolling technologies to reduce the non-compliance of the mechanical characteristics values within the limits stipulated in the manufacturing norms [13].

For this purpose, different deformation regimes were used for carbon steel and low alloyed sheets with thicknesses less than 40 mm.

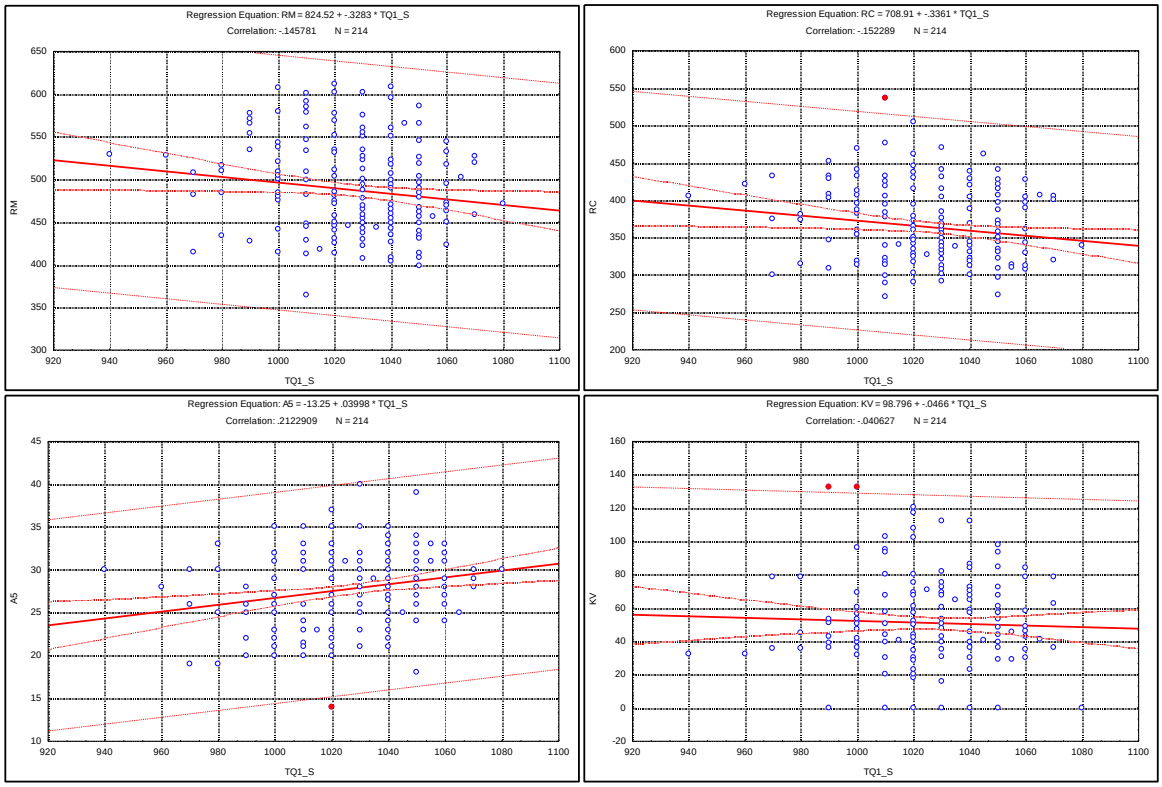

Fig. 1. *Results of the laboratory tests according to the final temperature of rolling in the roughing stand (TQ1-S)*

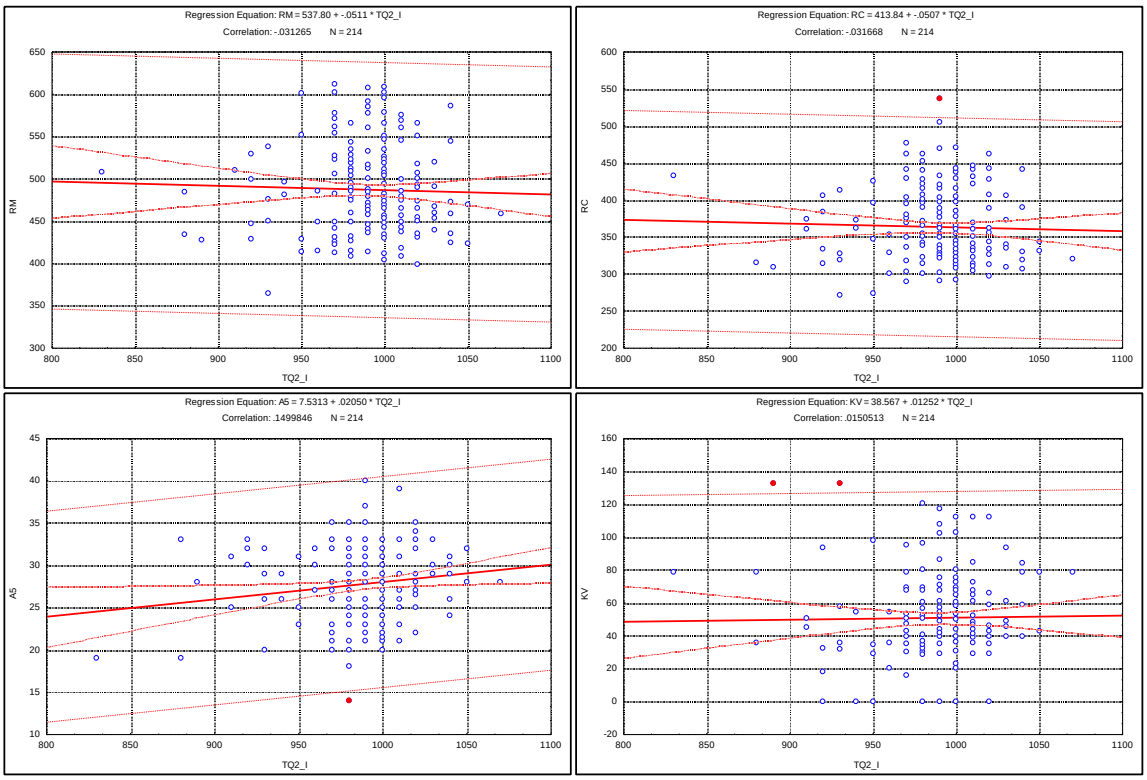

Fig. 2. *Results of the laboratory tests according to the starting temperature in the finishing stand (TQ2-I)*

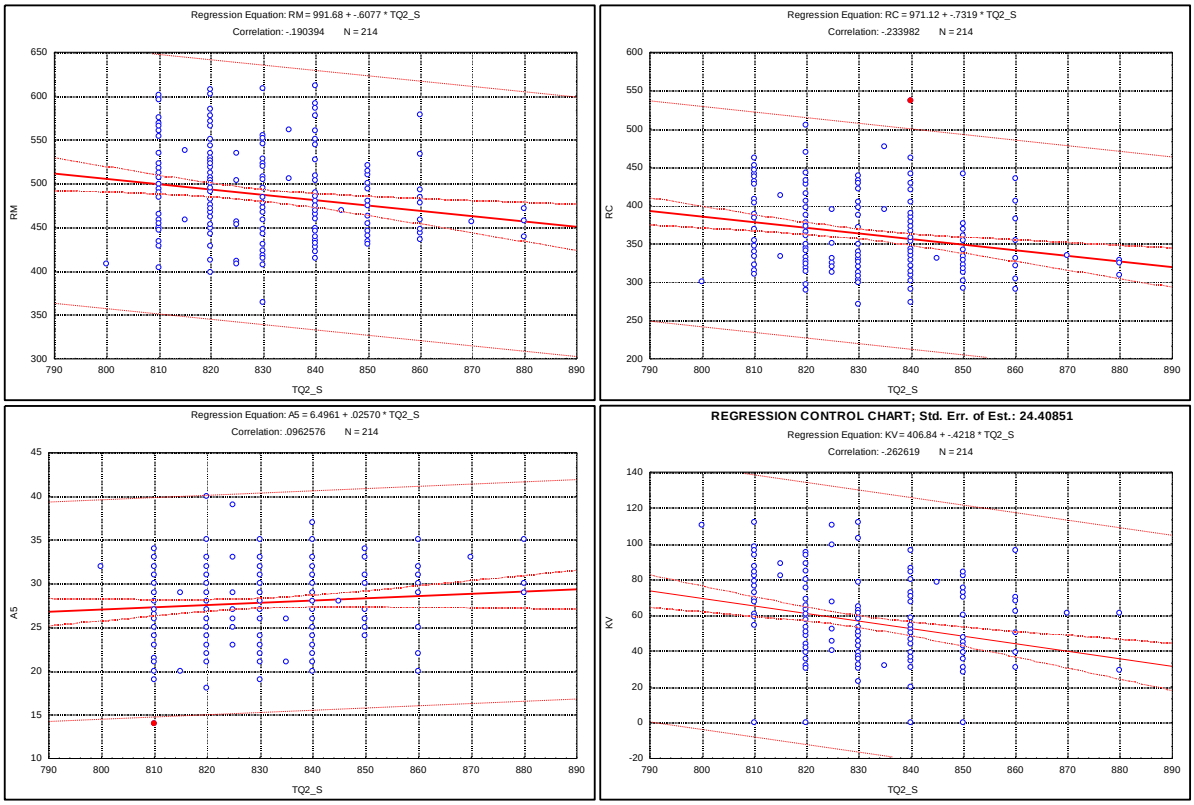

Fig. 3. *Results of the laboratory tests according to the final temperature of rolling in the finishing stand (TQ2-S)*

The parameters values recorded of the flow and the mechanical characteristics resulting from the laboratory tests have been recorded and processed.

With the results of the laboratory tests, the regression curves were plotted according to:

- the final temperature of rolling in the roughing stand (TQ1-S);
- the starting temperature in the finishing stand (TQ2-I);
- the final temperature of rolling in the finishing stand (TQ2-S);
- the degree of deformation in the roughing stand (DH-Q1) and;
- the degree of deformation in the finishing stand (DH-Q2) (as a percentage of the total reduction).

The graphical representation of the regression equations thus obtained is shown in Figures 1-3.

4. Conclusions and measures

4.1. Conclusions resulting from the processing of recorded data

From the analysis of the mechanical test values and the shape of the regression curves, the following conclusions are reached regarding the carbon and low alloy steel plates with thicknesses less than 40 mm:

a) the influence of the thermal deformation regime:

- the tensile strength and flow limit decreases with the increase of the end lamination temperature;
- elongation and resilience increase with the end lamination temperature increasing;
- deformation in the finishing stand provides values corresponding to the mechanical characteristics if it is in the range 980 - 820 °C;
- the final temperature of rolling is in the range 820-840 °C.

b) Influence of the deformation degree:

- by increasing the degree of reduction in the roughing stand over 75%, the values of the tensile strength, the flow limit and the resilience decrease while the elongation increases;
- by increasing the reduction in finishing stand, the values of the mechanical characteristics are higher than the minimum admissible limits and it is recommended that the reduction should be approx. 30% from the total reduction;

4.2. Measures to improve rolling technologies

We presented the dependence of the mechanical characteristics of the plate products on the manufacturing process parameters. Therefore, the mechanical characteristics can be varied within wide limits by choosing suitable manufacturing conditions within the three phases: elaboration, lamination, heat treatment.

1. For hot rolled flat products made of low carbon or low alloy steels up to 40 mm thick, it is possible the improvement of the strength properties by rolling at lower temperatures followed by accelerated cooling.

2. Achievement of high mechanical characteristics is ensured by the proper choice of steel and by strict observance of the specific technological parameters of the process: austenitic temperature, temperature and deformation degree, number of passes, duration of breaks between passes, final cooling conditions, etc.

3. It is proposed to supplement the manufacturing process instructions as follows:

- the application of a reduction degree of about 75% in the roughing stand;

- the final temperature of rolling in the finishing stand is between 820 and 840 °C.

References

[1]. Antonio Augusto Gorni, *Steel Forming and Heat Treating Handbook*, São Vicente SP Brazil, 20 February 2014.

[2]. Bordei M., Drăgulin I, Tănase D., Vasiliu A., *Tehnologii, agregate şi utilaje pentru deformare plastică la cald*, Ed. Ştiinţifică Fundaţia Metalurgia Română, ISBN 973-8151-26-0, Bucureşti, 2004.

[3]. Cazimirovici E., *Bazele teoretice ale deformării plastice*, Ed. Bren, Bucureşti, 1999.

[4]. Cananau Nicolae, Tanase Dinel, *Bazele teoretice ale deformărilor plastice - Rezistenţa la deformare a materialelor metalice*, Galati University Press, 2011.

[5]. Chen C. Y., Yen H. W., Kao F. H., Li W. C., Huang C. Y., Yang J. R., Wang S. H., *Precipitation hardening of high-strength low-alloy steels by nanometer-sized carbides*, Materials Science and Engineering, 499(1), p. 162-166, 2009.

[6]. Mihoc G., *Matematici aplicate în statistică*, Ed. Academiei, Bucureşti, 1988.

[7]. Moretto Christian, *Making Heavy Plate - plate mill rolling process*, ArcelorMittal University 2014;

[8]. Ginzburg Vladimir B., Ballas Robert, *Fundamentals of Flat Rolling Manufacturing Engineering and Materials Processing*, Publisher CRC Press, 2000.

[9]. Potecaşu Florentina, Potecaşu Octavian, Drugescu Elena, Alexandru Petrică, *The Influence of Cold Rolling on the Microsucture for Drawing Steels*, The Annals of 'Dunărea de Jos' University of Galaţi, Fascicle IX Metallurgy and Material Science, no. 2, p. 40-46, 2007.

[10]. Potecasu Octavian, Potecasu Florentina, Alexandru Petrica, Radu Tamara, *The Influence of Cold Rolling on the Mechanical Characteristics for Drawing Steels*, The Annals of 'Dunărea de Jos' University of Galaţi, Fascicle IX Metallurgy and Material Science, no. 1, p. 55-61, 2008.

[11]. Sakaia Taku, Belyakovb Andrey, Kaibyshevb Rustam, Miuraa Hiromi, Jonasc John J., *Dynamic and postdynamic recrystallization under hot, cold and severe plastic deformation conditions*, Progress in Materials Science, vol. 60, p. 130-207, March 2014.

[12]. Stănescu C., *Studii şi cercetări de modelare matematică a procesului de laminare la caje reversibile*, Teză doctorat, Universitatea-Politehnica Bucuresti 1996.

[13]. Wang X. D., Huang B. X., Wang L., Rong Y. H., *Microstructure and mechanical properties of microalloyed highstrength transformation-induced plasticity steels*, Metallurgical and Materials Transactions A., 39(1), p. 1-7, 2008.

[14]. Charles Romberger, *Studiu tehnico economic LTG2 - 1979 - Procedura de fabricaţie a tablelor groase/ Making Heavy Plate - Slab prepapration*, ArcelorMittal University, 2014.

THE ANNALS OF "DUNAREA DE JOS" UNIVERSITY OF GALATI
FASCICLE IX. METALLURGY AND MATERIALS SCIENCE
N°. 4 - 2017, ISSN 1453-083X

DESTRUCTION OF THE INSIDE PART OF A COAT OF A HARD CHROME CYLINDER USED FOR COMBUSTION ENGINES

Marian BORDEI, Florentina POTECAȘU
"Dunarea de Jos" University of Galati
email: Marian.Bordei@ugal.ro

ABSTRACT

This paper had as a starting point the broken down through explosion suffered by the coat of a cylinder made of cast iron. The cylinder coat material must provide the necessary resistance to dynamic and static stresses and, especially, to wear, taking into account the operation in particularly unfavorable friction conditions. Analyzes have been made on the quality of the material in terms of chemical composition and microstructural analysis.

For comparison, the same investigations were carried out on samples taken from a cylinder coat with a good functioning (blank samples). This paper presents the analysis and conclusions regarding the chemical composition of the material from which the landmark chrome cylindrical coat was used for combustion engine, in order to determine the causes of its breakage and the excessive wear of the segments.

KEYWORDS: hard chrome coat, microstructural analysis, graphitizing elements.

1. Introduction

The cylinder is the organ inside which the piston moves and the engine fluid evolves. It is usually made in the form of a metallic bush, also called the drum sleeve. The drum liner material must provide the necessary resistance to dynamic and static stresses and specially to wear, taking into account the operation in particularly unfavourable friction conditions [1-2].

The most commonly used material is the grey cast iron alloyed with Cr, Ni, Mo, Ti, V, elements that increase wear resistance. More narrowly, aluminium alloys are used, although they are lighter and have a higher thermal conductivity, have a mechanical resistance and unsatisfactory corrosion. In some engines with special functional parameters, coat of Cr steel, nitrides steels and graphite steels are also used. The process of making the cylinder coats is casting (usually, centrifugal casting), followed by chunking, chrome plating, nitration or phosphating. Light alloys are chrome-plated or metallized, resulting both increased hardness and improved lubrication [1-2].

Common grey cast iron has the following characteristics: good casting properties, less solidification shrinkage than steels, high fluidity, which allows thin-walled parts to be made, complex shapes unreachable by mechanical methods, mechanical properties of strength and tenacity inferior to steels due to the presence of graphite. However, graphite also has positive effects if it shows the optimal amount, size, shape and distribution, ensuring good machining by cutting, high vibration damping capacity, lubricating properties under dry rubbing conditions, nipple insensibility, corrosion resistance in common corrosion environments [3-7].

The main element, which influences the structure of the cast iron, is the carbon. In grey iron for machine building, carbon is found within 2.6-3.8%. Lower limit decreases for alloyed alloys with strongly graphitizing elements, Si and Al.

Carbon is a graphitizing element that increases the amount of graphite in the grey cast iron structure and reduces the amount of perlite. Consequently, the increase in carbon content, by increasing the amount of graphite, leads to the decrease of the mechanical strength, hardness and tenacity of the cast iron. In white or mottled cast iron, the increase in carbon content increases the amount of cementite, hardness and brittleness [3-4, 7-8].

The quantity, size, shape and mode of graphite distribution with positive effects on the mechanical characteristics and area of the applications [3-8] can

be obtained by changing the conditions of production or casting and by heat treatment.

2. Materials and experimental conditions

Samples were taken for analysis from a well-functioning of the cylinder coat, samples used as a control (A series), and samples from a cylinder coat breached by explosion (B series).

Since the carbon content in the two series of materials is the same (2.8%) and corresponds to that required by the manufacturer, analysis regarding the quantity of graphitizing, anti-graphitizing and carburizing elements from the chemical composition (the two series of materials with such different behavior in industrial practice) were imposed in order to determine the possible causes which led to the explosion breakdown.

Table 1 presents the chemical analysis for the graphitizing elements of the two series of materials determined by means of an X-ray fluorescence spectrometer from the material characterization laboratory. Table 2 shows the chemical analysis of the anti-graphitizing and carburizing elements determined by the spectrometer.

Table 1. *The chemical analysis for the graphitizing elements*

Series of samples	The determined element	
	Si [%]	**Cu [%]**
A Series (blank samples)	2.46±0.12	0.27±0,03
B Series	2.28±0.12	0.41±0,03

Silicon is found in grey cast iron within 1.5-2.5%. The lower limit drops to 0.5% Si in the white and upper castles it raises to 16% Si in alloy cast iron. Silicon dissolves in ferrite, and it hardens it. Ferrite from grey cast iron, also called silico-ferrite, has a tensile strength Rm = 350-500 N/mm^2 and hardness HB = 100-150 daN/mm^2, superior to steel. Silico-ferrites is included in the perlite (mechanically ferric + cementitious mixture), which is also harder and more resistant: Rm = 900-1200 N/mm^2, HB = 220-330 daN/mm^2. Silicon is a strongly graphitizing element, which increases the refractoriness of the cast iron. Silicon increases the amount of ferrite and graphite, reduces the amount of perlite, and thereby reduces the strength and hardness of grey cast iron [3-4, 8].

In the Maurer structural diagram of Figure 1, the influence of carbon and silicon content on the structure of cast iron is reflected [2]. It can be noticed that at the same carbon content (as in the case of the A and B series cast iron analyzed in the paper) but with the variation of the silicon content, the entire range of cast iron can be obtained: I - white cast iron; II - perlite-cementitious grey cast iron; III - grey pearls; IV - ferrite-perlite grey lichens; V - ferrite grey cast iron.

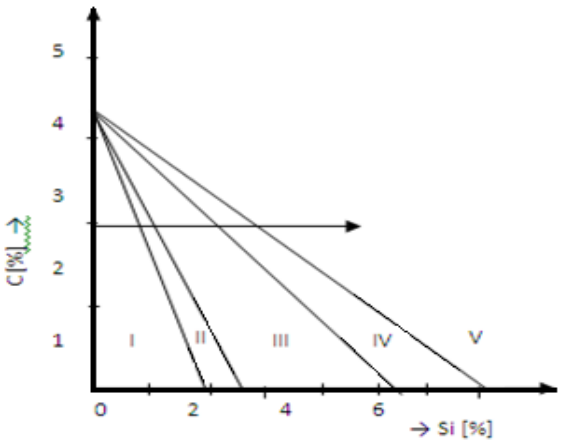

Fig. 1. *The Maurer structural diagram*

Analyzing the results in Table 1 for the two series of materials, it is obvious that if both series have the same carbon content (2.8%) and the series A, with good functioning, has the perlite matrix (sector III in Figure 1) implies that for series 2, the reduction in silicon quantity to 2.28% for the same thickness of the cylinder coat, can lead to structures with areas in sector II, or even I. In this case, these structures can lead to hardening of the cast iron and to an increase in the fragility of the pieces [4, 8]. For this reason, a rigorous microstructural study is required to correlate the chemical composition with the cast iron structure and properties derived from the structure.

Table 2 shows the chemical analysis of the anti-graphitizing and carburizing elements determined by the spectrometer.

Table 2. *The chemical analysis of the anti-graphitizing and carburizing elements*

Series of samples	The determined element		
	Cr [%]	**Mn** [%]	**Mo** [%]
A Series (blank samples)	0.35±0.03	0.53±0.04	0.43±0.01
B Series	0.54±0.02	0.35±0.05	0.19±0.01

The carburizing alloy elements Cr, Mn, Mo have anti-graphitizing action, and the non-carboniferous elements Si, Cu are graphitizing. The anti-graphitizing elements (Cr, Mn, Mo) are elements which either dissolve in cement [$(Fe, Mn)_3C$, $(Fe, Cr)_3C$], which stabilizes, or forms stable carbons, which facilitates cementitious germination (Cr_2C_3, Mo_2C). The carburizing elements, determined by Mn, Cr, Mo, are those that have higher affinity to carbon and, after interaction, they form stable carbides [3-4, 8].

Manganese is dissolved in cement, increasing its stability, or in the form of sulphides. It is an anti-graphitizing element, which increases the amount of grey cast iron, i.e. the mechanical strength, hardness and wear resistance of the cast iron [3-4, 8]. Molybdenum is an alphagen element that partially dissolves in ferrite and cementite, the remainder forming carbides. In this way the characteristics of resistance and, to a certain extent, plasticity increase.

The alloying elements which partially dissolve in the cementite, partially form their own carbides, such as chromium and molybdenum, can form (especially when present in amounts exceeding solubility in cementite) EA_7C_3, $EA_{23}C_6$ or EA_6C type carbides with complex crystalline structure too, which dissolves relatively easily in austenite (on heating of alloyed steels or alloys) and type EAC, with cubic crystal structure or EA_2C, with hexagonal crystal structure (insoluble in austenite) [3-4, 8].

Carbides of alloying elements compared to iron carbide (cementite) are tougher and influence the properties of the material according to their quantity, size, shape, dispersion in the metal matrix. Thus, the primary carbons (as individual phases or as the constitutive phases of the eutectic mixture) can be arranged at the boundaries of the basic metallic mass in a mesh form and lead to an increase in the strength characteristics (mechanical strength and hardness), but diminish considerably plasticity and tenacity (in the case of chromium and manganese carbides). The fine-grained globular carbons (molybdenum carbides), uniformly dispersed, are desired phases in the base mass, as it provides a good complex of mechanical characteristics (with high values of both mechanical strength and hardness characteristics as well as plasticity and tenacity characteristics) [3-4, 8].

Analyzing the elements determined in Table 2, we can assume that considering the high carbon concentrations of the two series of cast iron and taking into account the quantities of graphitizing alloying elements (Si) as well as the quantities of carburizing alloying elements (Cr, Mn, Mo) it is possible that at their liquid cooling, the eutectic transformation to be realized, and small amounts of ledeburite (constituent specific to the structure of the white or spherical pigments, zones I and II in Figure 1) [9-12] to appear in their structure. Obviously, to the B Series with less silicon, a larger amount of carbon remains which is available to interact with the carburized elements. Depending on the carbon concentrations and alloying elements that characterize their composition, the ledeburitic formations in the structure of these steels can be dispersed coherently, in the form of an intergranular mesh (referred to as the ledeburitic skeleton), which can be primed and crack propagation pathways external requests [3, 8].

Starting from the analysis of the chemical composition of the material from which the hard chrome coat cylinder was made, destroyed by explosion and excessive wear of the segments, we determined the metallographic appearance on two polished samples (B series) but without metallographic attack from areas with and without cracks (Figure 2).

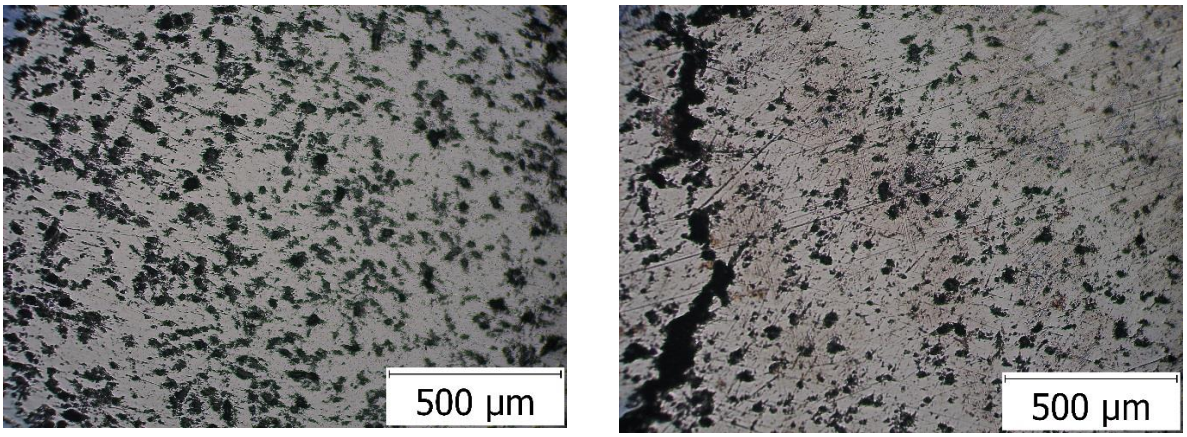

a) *b)*

Fig. 2. *Microstructure of the material (B Serie) on polished probe (without metallographic attack). Magnification 100:1*

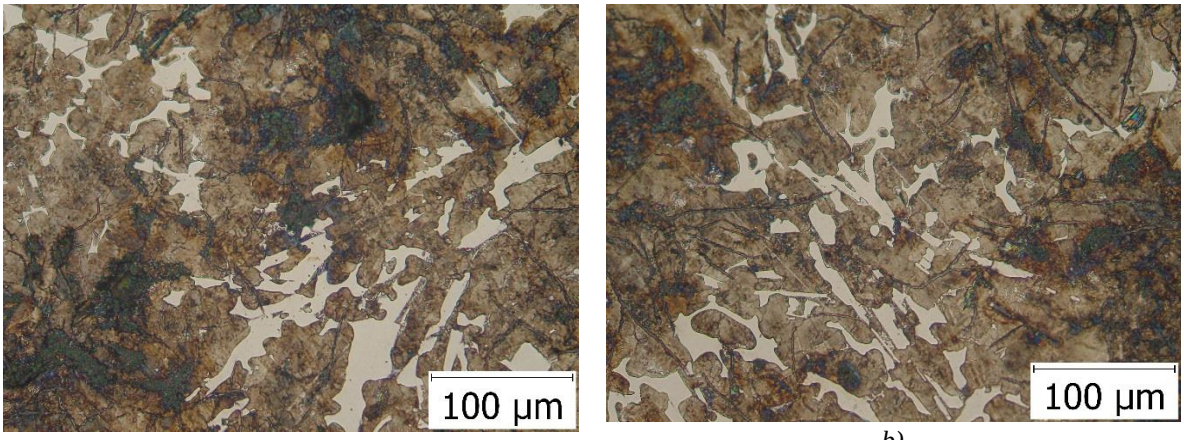

a) *b)*

Fig. 3. *Microstructure of the material (B Serie) on polished probe and attacked metallographic) (with nital reactive); Magnification 100:1*

The shape, magnitude and dispersion of graphite in the base mass (dark grey colour) as well as white glowing micro-volumes suggesting the presence of free carbons have induced the idea that it could be a mottled cast iron (a part of carbon in free graphite form and another part in free form of carbides). Such an inappropriate structure would not be desirable considering the working properties of the cylinder coat landmarker.

On this purpose, the microstructures of the samples in the areas where the explosion cracks were propagated were studied in order to identify the structural constituents in the base mass (Figure 3).

The microstructures confirmed that the B series cast iron matrix is a perlite, but due to alloying amounts, it includes Alloyed carbides I (alloyed primary carbides), Alloyed carbides II (alloyed secondary carbides) with white colour and an atypical eutectic with both dispersed carbon forms in the matrix perlite, carbide and graphite, E [P + Graphite II + Alloyed carbides II + Graphite E], which explains the increased fragility of the piece breakdown through explosion.

3. Conclusions

The results obtained suggested the need for a thorough / rigorous, comparative (for the two A series and B series) microstructural analysis to explain the inappropriate behaviour, the destruction through explosion of the benchmark (B series), although the cast iron of the cylinder has the correct content of carbon. The beneficiary only requested the form of graphite and the perlite metallic matrix. The analysis of the authors has shown that for proper functioning it is necessary to specify not only the quantity of carbon but also the quantity of carbon in correlation with the alloy elements in order to achieve the correct physical-chemical constitution of the cast iron (structural constituents and constitutive phases).

References

[1]. Roşca R., Rakosi E., Manolache Gh., Roşu V., Elemente de tehnologia autovehiculelor, Editura "Politehnium" Iaşi, 2005.
[2]. Popa B., Bățagă N., Căzilă A., Motoare pentru autovehicule, Editura Dacia, Cluj-Napoca, 1982.
[3]. Levcovici M. S., Studiul materialelor I, Editura Fundaţiei Universitare "Dunărea de Jos", Galaţi, 2002.
[4]. Potecasu F., Metalurgie fizică, vol. 1, ISBN-978 - 973-8151-48-1; ISBN-978 - 973-8151-49-9- Editura FRM, 2007.
[5]. ***, SR EN ISO 945-1:2009/AC:2010 ver.eng. Microstructura fontelor. Partea 1: Clasificarea grafitului prin analiză vizuală.
[6]. Ripoşan I., Sofroni L., Fonta cu grafit vermicular. Bucureşti. Editura Tehnică, 1984.
[7]. Sofroni L., Ripoşan I., Brabie, V. Chişamera M., Turnarea fontei, Bucureşti. Editura Didactică şi Pedagogică, 1985.
[8]. Potecasu F., Transformări structurale în materiale cristaline – e-book, platforma ugal, 2014.
[9]. Cojocaru- Filipiuc V., Ipoteze cu privire la obţinerea de materiale metalice pe baza tendinţei spre echilibrul chimic - aplicaţii la modificarea fontelor, Iaşi. Editura „Politehnium", 2011.
[10]. Cojocaru-Filipiuc V., Remanent graphite and its implication in modification process of iron, Metalurgia Internaţional, Vol. XV No. 5. p. 57-62, 2010.
[11]. Jukov A. A., Fe-C. The stable and metastable equilibria. Giessereiforschung, p.106-112, 1992.
[12]. Dumitrescu T., Diagrama de echilibru stabil Fe-C, Ed Universitatea "Dunărea de Jos", Galaţi, 1989.

THE ANNALS OF "DUNAREA DE JOS" UNIVERSITY OF GALATI
FASCICLE IX. METALLURGY AND MATERIALS SCIENCE
N°. 4 - 2017, ISSN 1453-083X

MATERIAL BALANCE IN A BLAST FURNACE, WHEN REPLACING COKE WITH COAL DUST

Adrian VASILIU
"Dunarea de Jos" University of Galati
email: avasiliu@ugal.ro

ABSTRACT

The paper presents the technology for the preparation and burning of coal dust in the blast furnace, as well as the material balance, - without and with the in - of coal dust. On the basis of the comparative analysis, measures are proposed to replace the amount of coke with coal dust in the range of 0.8-1 coke / CDI.

KEYWORDS: *blast furnace, coke, injection of coal dust (CDI), material balance*

1. Introduction

In advanced ironmongery, the development of this process has grown since 1983, so over 100 plants currently consume 20 million tons of energy per year, replacing 19 million tons of coke.

Current research is directed towards optimizing the coke/coal dust replacement ratio so that this ratio remains in the range of 0.9 ÷ 1.1 kg coke / kg of coal, being very dependent on the type of coal and especially the way it is prepared. Thus, in the European Union there is currently a brew of approx. 180 kg CD/$t_{p.i}$, at a consumption of 320 kg coke/$t_{p.i}$.

The efficiency of the use of auxiliary fuels consists of the price difference from coke and the high coke replacement coefficient 0.8-0.9. This coefficient depends on the blast furnace operating conditions, the calorific value of the auxiliary fuels, and the energy consumption required to feed the blast furnace.

The ArcelorMittal Steel Galati plant is equipped with a CDI[1] preparation unit and a distribution and injecting transmission installation at the blast furnace, a plant made at the highest level of the current technology, having a capacity of 70 tons coal dust/h and 560,000 tons/year, and can save between 400,000 and 500,000 tons of coke per year.

2. Objectives

The aim is to reduce the consumption of coke from the blast furnace load by infusing the coal dust:

- on the short term, reducing energy costs per ton of pig iron by reducing coke consumption;
- on the medium and long term, the reduction in the share of coke ovens, sections with high pollutant potential and the recovery or replacement of which have a high cost price.

This involves the use of quality materials for blast furnace loading, agglomerated coke, coal, and intensification of the coal dust burning process at the tuyeres, reducing the proportion of carbonaceous residue left off and adequate equipment with computational techniques.

3. Theoretical considerations

The theoretical study of the combustion of pulverized coal in the burning area in front of the tuyeres blows shows the importance of maintaining a sufficiently large and stable cavity.

The most important steps, which describe the carbon dioxide combustion process in the air, are the following:

a) Combustion chemical reactions. In order for the combustion process to occur it is necessary for the oxygen atoms to reach the reaction front and the reaction products to be removed in the atmosphere (Figure 1).

Under the high temperature of the burning area in front of the wind gullies, 70-80% of the coal dust mass is consumed in the process as follows:

- volatile materials react in gaseous phase:

$$C_{(s)} + 0{,}5\ O_{2(g)} \rightarrow CO_{(g)} \quad \Delta H = < 0 \quad \text{Exoth.}$$
$$H_2 + 0{,}5\ O_2 \rightarrow H_2O \quad \Delta H = < 0 \quad \text{Exoth.} \qquad (1)$$

[1] CDI - coal dust injection

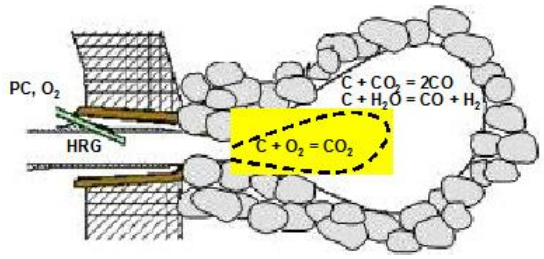

Fig.1. *Carbon burning in front of the tuyere*

- in cases of oxidant deficiency, carbon dissociation (carbon black) can also be formed. The carbon residue suffers a heterogeneous reaction:

$C_{(s)} + 0{,}5\ O_{2(g)} \rightarrow CO_{(g)}$ $\Delta H = < 0$ Exoth.
$C_{(s)} + CO_{2(g)} \leftrightarrow 2CO_{(g)}$ $\Delta H = > 0$ Endoth. (2)

- coke is subject to a heterogeneous combustion reaction similar to coal residue:

$C + O_{2(g)} + N_{2(g)} \leftrightarrow CO_{2(g)} + N_{2(g)}$ $\Delta H = < 0$ Exoth.
$C + CO_{2(g)} \leftrightarrow 2CO_{(g)}$[2] $\Delta H = > 0$ Endoth. (3)
$C_{(s)} + H_2O_{(g)} \rightarrow CO_{(g)} + H_{2(g)}$ $\Delta H = > 0$ Endoth.

Since the reaction takes place in the presence of excess carbon at a high temperature, the carbon dioxide is reduced by the Bell-Boudouard reaction (Figure 2) or loss of carbon monoxide solution (eq.3).

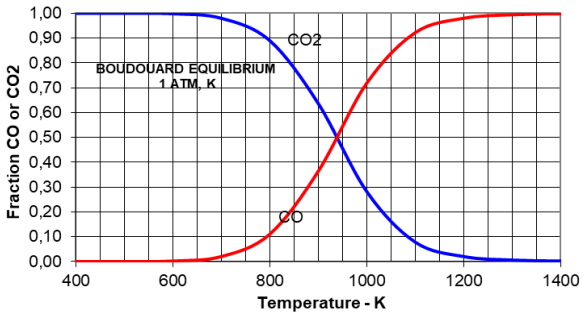

Fig. 2. *Bell - Boudouard diagram*

b) Transfer of reaction products from the ash surface to the volume of the gaseous phase. The CO flow at the ash-atmosphere interface is determined with the relation:

$$F_{\{CO\}} = 4\pi r_0^2 \cdot K_d^{CO} \cdot C[X_{CO}^s - X_{CO}^{\upsilon}] \quad (4)$$

Similarly, the CO2 flow is calculated by:

$$F_{\{CO_2\}} = 4\pi r_0^2 \cdot K_d^{CO_2} \cdot C[X_{CO_2}^s - X_{CO_2}^{\upsilon}] \quad (5)$$

Where:

- r_0 - radius of spherical coal;
- K_d^{CO}, $K_d^{CO_2}$ - transfer mass constant of CO/CO_2 in the volume of the gaseous phase;
- X_{CO}^s, $X_{CO_2}^s$ - the molar fraction of CO/CO_2 at the surface of the ash coke turned into ash;
- X_{CO}^{υ}, $X_{CO_2}^{\upsilon}$ - The molar fraction of CO/CO_2 in the volume of the gaseous phase.

The schematic of coal dust injection technology and internal structure around raceway in a blast furnace is shown in Figure 3.

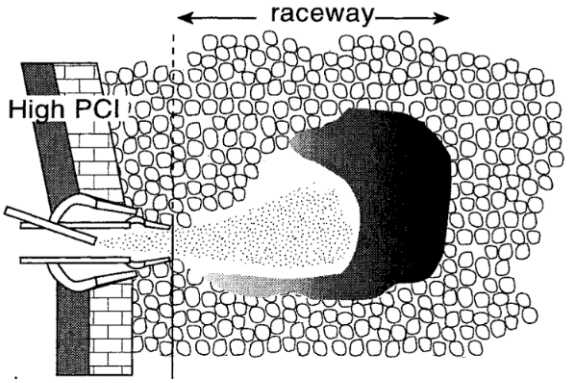

Fig. 3. *Pulverized coal reactions in the raceway*

The main parameters influencing the burning rate of the coal dust, at the blast furnace tuyeres are:
- granulometry or specific surface area of the CDI;
- degree of enrichment in oxygen;
- the type of coal;
- chemical composition of coal;
- the excess of air or oxygen;
- air temperature;
- air humidity;
- the temperature of the flame;
- the gas composition profile of the combustion zone (the maximum CO_2 tuyere);
- running of the blast furnace.

c) Blast furnace material balances. The material balance must always be accompanied by an indication of the area of the installation to which the balance sheet relates. The mass balance is calculated for all components involved in the process (Figure 4), and is defined as:
- the mass of materials entering the system;
- mass of materials leaving the system.

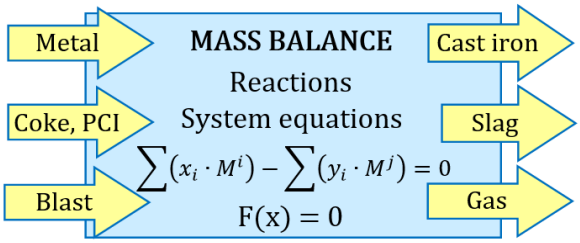

Fig. 4. *Mass balance*

[2] Bell - Boudouard reaction

The calculation is based on the mass balances considering all injectors with the following assumptions:

- the oxygen in the coke composition can be neglected in comparison with the O_2 content of the blowing air;
- the reducing gas in the tank does not contain free oxygen, this means that all the available oxygen is reacting in front of tuyere gullies to form CO;
- the downstream gas from the blowpipe area does not contain CO_2, if carbon oxides are formed as a result of the various carbon dioxide reduction reactions, it is immediately converted to CO as a result of the Bell - Boudouard reaction.

In the area of direct reduction there are only oxides reduction reactions with carbon. This means that H_2 reacts with oxides in the area of indirect reductions. All the H_2 content in the blast furnace comes from the scaling area, the difference being consumed and converted to H_2O in the area of indirect reductions.

The percentage of indirect CO_2 reductions is defined as the ratio between the amount of CO_2 generated from indirect reduction reactions and the sum of the amounts of CO_2 and H_2O formed by indirect reduction reactions and the amount of CO formed from direct reduction reactions.

$$RI_{CO2} = \frac{CO_{2\text{indirect}}}{CO_{2\text{indirect}} + CO_{\text{direct}} + H_2O_{\text{indirect}}} \quad (6)$$

The percentage of indirect reductions that form H_2O is defined as the ratio between the amount of H_2O formed by indirect reduction reactions and the sum of the amounts of CO_2 and H2O formed by indirect reduction reactions and the amount of CO formed by direct reduction reactions.

$$RI_{H2O} = \frac{H_2O_{\text{indirect}}}{CO_{2\text{indirect}} + CO_{\text{direct}} + H_2O_{\text{indirect}}} \quad (7)$$

Mass balances allow for the calculation of the amount of CO produced by direct reduction reactions and the amounts of CO and CO_2 produced by the direct reduction reactions.

4. Method of research

The calculation of the material balance for two assumptions, respectively, without the CD insufflations with (1) and (2) the operation of the blast furnace with the insufflations of the coal dust. If the determination of the substitution ratio of coke with coal dust is not sufficient, the technical analysis is necessary, and knowledge of the elemental chemical composition of coal is also necessary. The calculation is complex and iterations can be applied in its deployment. Some empirical relationships are also considered.

The chemical composition of pig iron, coke and coal dust are given in tables 1-3.

Table 1. *The chemical composition of pig iron*

FAK2	Fe	C	Si	Mn	P	S	Ti	Rest.
%	94,34	4,10	0,40	1,1	0,1	0,03	0,14	0,64

Table 2. *The chemical composition of coke*

C	H	N	S	A	W_k	Slag	VM	H_i [kJ/kg]
86,8	0,40	0,60	0,50	10,30	4,00	0,195	1,65	17566

Table 3. *The chemical composition of coal dust*

C	H	N	S	A	W_{CD}	Slag	VM	H_i [kJ/kg]
75,55	5,11	1,40	0,70	6,55	1,25	0,134	34,02	26883

The balance material of the blast furnace process for 1000 kg pig iron is shown in Figure 5. The coke rate is settled as 340 kg/t of pig iron, the metallic cargo rate is 1600 kg/t of pig iron, the volume of top gas is about 1 500 Nm^3/h, the output slag from the bottom of the furnace is 275 kg, the amount of injected coal dust is 169 kg/t of pig iron and the produced pig iron is 1000 kg.

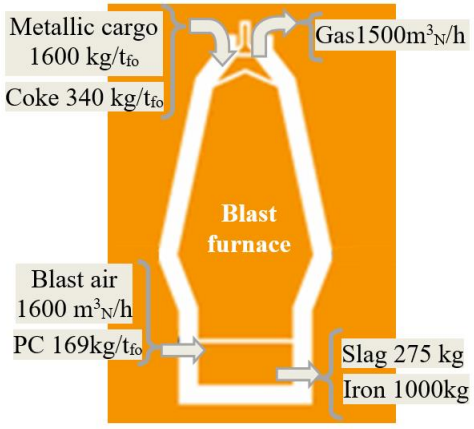

Fig. 5. *Balance material for 1000 kg pig iron*

- The amount of carbon that burns to CO_2 (gf):

$$C_{(CO_2)} = CO_{red} \cdot \frac{M_c}{22.4} = 213{,}01\ [kg\ C]$$

- The amount of carbon that burns at CO (gf):

$$C_{(CO)} = (CO_{gas} - CO_{\upsilon}) \cdot \frac{12}{2{,}44} = 132{,}55\ [kg\ C]$$

$$100\frac{M_{CDI}}{V_{air} \cdot \rho_{CDI}} = 7{,}866\ CDI\ [\%]$$

- Air preheats temperature:

$$T_{air} = t_{pa} + 60\frac{120}{1016{,}8} \cdot 100 = 1290^{o}C$$

The preheating temperature of the air is considered at 1000 – 1060 °C and of the coal dust at 60 °C.

- Humidity of tuyere blowing through the tuyere:

$$G_{air_{tu}} = W_{air} \cdot \frac{M_{H_2O}}{22,4} = 11,66\ [kg\ H_2O]$$

Carbon balance

The amount of carbon combustion (burnt) in the tuyere ($C_{b.tu}$) is determined as the difference between the amount of carbon introduced into the blast furnace and the amount of carbon consumed for combustion, reduction, casting, Bell - Boudouard reaction. Total carbon introduced into blast furnace with fuels:

$$C_{b_{tu}} = \langle C \rangle - [C] - C_{rd} = 281,59\ [kg_{carbon}]$$

- carbon coke:

$$C_k = k_t \frac{\%C_{fk}}{100} = 293,52\ [kg_{carbon}]$$

$$k_t = (100 - W_k) \cdot k_{th} = 336,6\ [kg_{carbon}]$$

- carbon with coal dust (CD):

$$C_{CDI} = CDI_t \frac{\%C_{fCDI}}{100} = 129,78\ [kg_{carbon}]$$

- total carbon introduced into the blast furnace:

$$\langle C \rangle = C_k + C_{CDI} = 423,30\ [kg_{carbon}]$$

- carbon carbide for iron (FeC):

$$[C] = \frac{1000}{100} \cdot [C_{pig\ iron}] = 41,1\ [kg_{carbon}]$$

- carbon direct oxide reduction is given in table 4:

Table 4. *Reducing carbon oxides*

Oxide	Reaction	kg_{carbon}	%
SiO_2	SiO_2+2C=Si + 2CO	$C_{Si_{rd}} = 6,00$	5,96
MnO	MnO + C = Mn+CO	$C_{Mn_{rd}} = 2,18$	2,16
P_2O_5	P_2O_5 + 5C=2P + 5CO	$C_{P_{rd}} = 1,45$	1,44
FeO	FeO + C=Fe +CO	$C_{Fe_{rd}} = 90,97$	90,42
$C_{rd} = C_{Si} + C_{Mn} + C_P + C_{Fe}$		**=100,60**	**100,00**

The total amount of iron that is reduced and turns into pig iron is:

$$[Fe] = 1000 - 10 \cdot \sum oxide = 94,01\ [kg_{Fe}]$$

where:

- $[Fe]$ - is the total iron, into the pig iron [kg/$t_{pig\text{-}iron}$];
- R_d - rate of direct reduction (R_i≈55%, R_d≈45%).

Carbon balance is given in Table 5 and also is illustrated in Figure 6.

Table 5. *Carbon balance*

Inputs			Outputs		
	Value	[%]		Value	[%]
C_k	293,520	69,340	$C_{pig\ iron}$	41,100	9,710
C_{CDI}	129,780	30,660	C_{rd}	100,610	23,760
			$C_{a.tu}$	281,590	66,530
Total	**423,300**	**100,00**	**Total**	**423,300**	**100,00**

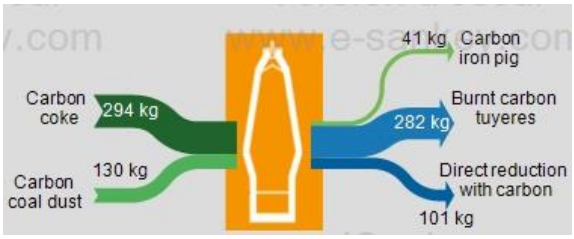

Fig. 6. *Carbon balance*

Hydrogen balance

Hydrogen is introduced into the blast furnace by the humidity in the air injected through the tuyere vents, the hydrogen brought from the volatile matter coal dust v_{CDI} and the coke volatile matter v_k :

$$H_t = H_{(air)_{wet}} + H_{v_{CDI}} + H_{v_k} = 7,98\ [kg_H]$$

- the amount of hydrogen introduced into the blast furnace with the inspired air (Table 6), (eq. 3):

$$H_{(air)_{wet}} = C_{b_{tu}} \cdot \frac{\%H_{air}}{\%O_{air}} \cdot \frac{2M_{H_2}}{22,4} = 2,250\ [kg_H]$$

Table 6. *Air composition [%]*

O_2	H_2	N_2	W	ρ_a [kg/m^3]
21,184	0,995	77,82	1,00	1,293

- the amount of hydrogen brought by volatile matter from coke (v_k):

$$v_K = k_{th} \cdot \%(v)_{(k)} = 5,554\ [kg_{v_k}]$$

$$H_{(v)k} = v_k \cdot \%H_v = 1,764\ [kg_H]$$

- the amount of hydrogen brought with the volatile matter from the coal dust (v_{CDI}):

$$v_{CDI} = CDI \cdot \%(v)_{(CDI)} = 57,5\ [kg_{v,CDI}]$$

$$H_{v_{CDI}} = v_{CDI} \cdot \%H_v = 3,966\ [kg_H]$$

To determine the minimum H_2 theoretical amount required for Fe_2O_3 reduction to iron, at a temperature typically considered as 900 ^{0}C, under the conditions of a countercurrent reactor, we can keep to the following scheme:

$3Fe_2O_3 + H_2 = 2Fe_3O_4 + H_2O$ Zone I. (8)
$2Fe_3O_4 + 2H_2 = 6FeO + 2H_2O$ Zone II. (9)
$6FeO + 6H_2 = 6Fe + 6H_2O$ Zone III. (10)

From the total amount of hydrogen (H_t) introduced into the blast furnace at indirect reductions

takes 40 ÷ 50%, the rest is the blast furnace gas (45%):

$$H_{r_{ind}} = (45)\% \cdot H_t = 3{,}910 \ [kg_H]$$

The amount of hydrogen in the blast furnace:

$$H_{gas} = H_{wet} + H_v - H_{r_{ind}} = 4{,}070 \ [kg_H]$$

The calculated data for hydrogen balance are given in Table 7 and also schematically represented in Figure 7.

Table 7. *Hydrogen balance*

Inputs			Outputs		
	Value	[%]		Value	[%]
$H_{(air)wet}$	2,250	28,190	$H_{rd.ind}$	3,910	48,997
$H_{(v)k}$	1,764	22,110	H_{gas}	4,070	51,003
$H_{(v)CD}$	3,966	49,700			
Total	**7,980**	**100,00**	**Total**	**7,980**	**100,00**

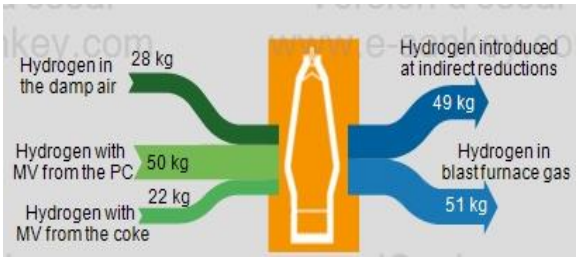

Fig. 7. *Hydrogen balance*

Carbon dioxide balance

According to the principle of transformation succession, the reduction of iron oxide (Fe_2O_3) is achieved in more stages. The lower iron oxide (FeO) is stable only at temperatures above 572 ^{0}C, and the reduction of iron oxides takes place as follows:

$$Fe_2O_3 \rightarrow Fe_3O_4 \rightarrow FeO \rightarrow Fe \qquad T > 572^\circ C \quad (11)$$

$$Fe_2O_3 \rightarrow Fe_3O_4 \rightarrow Fe \qquad T < 572^\circ C \quad (12)$$

The distribution and degree of oxidation of Fe and Mn in the blast furnace are given in Table 8.

Table 8. *The distribution and degree of Fe and Mn oxidation in the blast furnace*

Material	$Fe_{tot.}$	Fe		Mn_{tot}	Mn	
		Fe_2O_3	FeO		Mn_2O_3	MnO
Sinter	690,24	586,67	103,53*	4,31	4,31	-
Ore Fe	280	280	-	1,5	1,5	-
Ore Mn	7,98	7,98	-	16,81	16,81	-
Ash coke	8,66	-	8,66	0,105	-	0,105
Total	**986,88**	**874,65**	**112,19**	**22,72**	**22,62**	**0,105**
Pig iron	981,88	874,65	107,19	12,72	12,72	-
Slag	5,0		5,0	10	9,9	0,105

*- corresponding to 55-65 % Fe in the agglomerate

a) Amount of carbon dioxide resulting from the indirect reduction of metal oxides:

- the amount of oxygen resulting from the reduction of iron oxides, Fe_xO_y are given in Table 9.

Table 9. *The amount of oxygen resulting from the reduction of iron oxides, Fe_xO_y*

Oxide by Fe	Oxygen resulting from reduction (Fe_xO_y)	
	Fe	Oxygen, [kg]
$Fe_2O_3 \rightarrow FeO$	874,65	$874{,}65 \cdot 0{,}143^{**} = 125{,}074$
$FeO \rightarrow Fe$	874,65	$874{,}65 \cdot 0{,}268^{**} = 234{,}406$
$FeO \rightarrow Fe$	112,19	$112{,}19 \cdot 0{,}268^{**} = 30{,}066$
		Total 389,546

**) - $Fe_2O_3 \rightarrow 0{,}429$ $kgO_2/kgFe_{(Fe2O3)}$
- FeO $\rightarrow 0{,}286$ $kgO_2/kgFe_{(FeO)}$
$0{,}429 - 0{,}286 = 0{,}143$ $kgO_2/kgFe_{(Fe2O3 \rightarrow FeO)}$

Table 10.

Indirect reduction with CO (eq. 10, 11)	
$Fe_2O_3 \rightarrow FeO$	125,074 - 20,198 (red. H) = 104,388
$FeO \rightarrow Fe$	234,406+30,066-91,40 (red C) =173,067
Total oxigen, $O_{tot.Fe}$ = 104,388+173,067=**277,406**	

- the carbon dioxide obtained from the indirect reduction (eq. 5), results from the following calculation:

$$CO_{2_{r,ind.Fe}} = O_{tot.Fe} \cdot \frac{2 \cdot 22{,}4}{M_{O_2}} = 388{,}367 \ [Nm^3_{co_2}]$$

- the carbon dioxide resulting from the indirect reduction of manganese oxide is:

$$Mn_2O_3 + CO = 2MnO + CO_2 \qquad (13)$$

$$CO_{2_{r,ind.Mn}} = Mn_{tot} \cdot \frac{2 \cdot 22{,}4}{2 \cdot M_{Mn}} = 9{,}253 \ [Nm^3_{co_2}]$$

- total carbon dioxide from indirect reduction is:

$$CO_{2_{r,ind.Fe}} + CO_{2_{r,ind.Mn}} = 397{,}622 \ [Nm^3_{CO_2}]$$

b) CO_2 from volatile coke materials are:

$$CO_{2\ vk} = k_t \cdot \frac{v_k}{100} \cdot \frac{CO_{2(vk)}}{100} \cdot \frac{22{,}4}{M_{CO_2}} = 1{,}425 \ [Nm^3_{CO_2}]$$

c) CO_2 from volatile CDI materials:

$$CO_{2\ vCDI} = CDI \cdot \frac{v_{CDI}}{100} \cdot \frac{CO_{2(vCDI)}}{100} \cdot \frac{22{,}4}{M_{CO_2}} = 6{,}058 \ [Nm^3_{CO_2}]$$

d) CO_2 in blast furnace gas there are:

$$CO_{2\ gas} = 397{,}622 + 1{,}425 + 6{,}058 = 405{,}105$$

$$G_{CO_2} = CO_{2\ gas} \cdot \frac{28}{22{,}4} = 506{,}381 \ [kg\ CO_2]$$

The calculated data for carbon dioxide balance are given in Table 11 and also schematically represented in Figure 8.

Table 11. *Carbon dioxide balance [$Nm^3_{CO_2}$]*

Inputs			Outputs		
	Value	[%]		Value	[%]
$CO_{2_{r,ind}}$	397,622	98,154	$CO_{2_{gas}}$	405,105	100
$CO_{2_{vk}}$	1,425	0,351			
$CO_{2_{vCDI}}$	6,058	1,495			
Total	**405,105**	**100,00**	**Total**	**405,105**	**100,00**

Fig. 8. *Carbon dioxide balance*

Carbon monoxide balance

a) CO resulted from direct reduction reactions is from direct reduction of FeO to Fe (eq. 6); it is allowed a proportion of 46% from FeO → Fe and for 92,73% Fe in pig iron:

$$CO_{Fe} = 170,62\ [Nm^3_{CO}]$$

Carbon monoxide resulted from direct reduction of oxides is given in Table 12.

Table 12. *Carbon dioxide from direct reduction*

Oxide	Reaction	$[Nm^3_{CO_2}]$	%
SiO_2	SiO_2+2C=Si + 2CO	$CO_{Si} = 6,40$	
MnO	MnO + C = Mn+CO	$CO_{Mn} = 4,68$	
P_2O_5	P_2O_5+5C=2P + 5CO	$CO_P = 32,51$	
FeO	FeO + C=Fe +CO	$CO_{Fe} = 170,62$	
		$CO_{r.dir.} = 214,21$	**100**

b) From the burning of carbon to the tuyere (eq. 6):

$$CO_{b_{tu}} = C_{b_{tu}} \cdot \frac{22,4}{12} = 525,635\ [Nm^3_{CO}]$$

c) From volatile matter of coke:

$$CO_{v,k} = k_t \cdot \frac{\%v_k}{100} \cdot \frac{\%CO_{vk}}{100} \cdot \frac{22,4}{M_{CO}} = 1,64\ [Nm^3_{CO}]$$

d) Carbon monoxide consumed at indirect cuts:

$$CO_{cons.} = CO_{2_{red}} = 397,62\ [Nm^3_{CO}]$$

From the amount of carbon monoxide obtained, the amount of monoxide required to carry out the reduction reactions decreases.

Total carbon monoxide in the blast furnace gas is:

$$CO_{gas} = CO_{r.dir.} + CO_{b_{tu}} + CO_{mv} - CO_{cons.} =$$

$$= 343,81\ [Nm^3_{CO}]$$

$$G_{CO_{gas}} = CO_{gas} \cdot \frac{28}{22,4} = 429,77\ [kg_{CO}]$$

The calculated data for carbon monoxide balance are given in Table 13 and also schematically represented in Figure 9.

Table 13. *Carbon monoxide balance [Nm^3_{CO}]*

Inputs			Outputs		
	Value	[%]		Value	[%]
$CO_{r.dir.}$	214,210	28,889	CO_{cons}	397,620	53,624
$CO_{b_{tu}}$	525,635	70,890	CO_{gf}	343,865	46,375
$CO_{v,k}$	1,640	0,221			
Total	**741,485**	**100,00**	**Total**	**741,485**	**100,00**

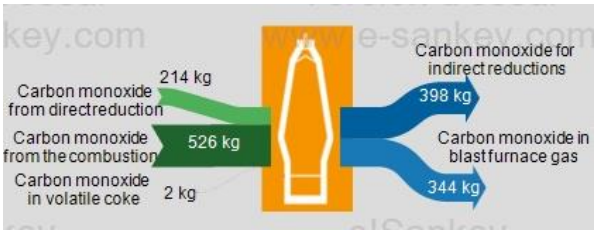

Fig. 9. *Carbon monoxide balance*

Nitrogen balance

a) Oxygen blown on blast furnace blasts:

$$O_{2\ tu} = C_{b_{tu}} \cdot \frac{22,4}{2 \cdot 12} = 262,817\ [Nm^3_{O_2}]$$

The amount of nitrogen brought by the air:

$$N_{2\ air} = O_{2_{tu}} \cdot \frac{77,82}{21,184} = 965,466\ [Nm^3_{N_2}]$$

b) Coke volatile nitrogen

$$N_{vk} = k_t \frac{\%v_k}{100} \cdot \frac{\%N_2}{100} \cdot \frac{22,4}{28} = 0,732\ [Nm^3_{N_2}]$$

c) Nitrogen from coal dust:

$$N_{vCDI} = CDI \cdot \frac{\%v_{CDI}}{100} \cdot \frac{\%N_2}{100} \cdot \frac{22,4}{28} = 0,647\ [Nm^3_{N_2}]$$

Total nitrogen in blast furnace gas:

$$N_{gas} = N_{air} + N_{vk} + N_{vCDI} = 966,845\ [Nm^3_{N_2}]$$

$$G_N = N_{gas} \cdot \frac{28}{22,4} = 1208,556\ [kg\ N_2]$$

The calculated data for nitrogen balance is given in Table 14.

Table 14. *Nitrogen balance [$Nm^3{}_{N_2}$]*

Inputs			Outputs		
	Value	[%]		Value	[%]
$N_{2\ air}$	965,466	99,857	N_{gas}	966,845	100
$N_{2\ vk}$	0,732	0,076			
N_{vDCI}	0,647	0.067			
Total	**966,845**	**100,00**	**Total**	**966,845**	**100,00**

The volume of air blowing is:

$$V_{air} = O_{2\ tu} \cdot \frac{100}{21{,}184} = 1240{,}639\ [Nm^3\ air]$$

5. Conclusions

The blasting of the pulverized coal is made in order to reduce the consumption of coke, the replacement of liquid fuels and natural gas, the increase in economic efficiency and the improvement of environmental conditions.

The worldwide trend is to continuously decrease the specific consumption of coke in the blast furnaces. Thus, in the European Union there is a current of approximate 180 kg CDI/t of pig iron, consumption of 320 kg coke/t of pig iron.

The efficiency of CDI technology is determined by the amount of CD injecting and the coke - CD replacement index obtained.

Iron production in ArcelorMittal Galati uses a modern injection of coal dust plant with a nominal capacity of 70 t CD/h or approx. 560,000 t CD/year.

For all periods of operation with the CDI, the replacement index is set at acceptable, of 0.8 ÷ l kg coke/kg CD. The main problem to be resolved remains the increase of the CDI above the apparent critical level to that corresponding to the rated capacity of the installation. Regime characterized by temperature air - 1060 ^{0}C the enrichment of the air in oxygen by 2% and the maintenance of the same air humidity at the injection of 100 kg/t of pig iron resulted a specific coke consumption of 434 kg/t of pig iron, replacement, E = 0.87 kg coke/kg CD, which also takes into account the influences of the measures that condition CD injection.

In many cases, however, there is a ceiling for acceptance of blast furnace CDI at 130 - 160 kg CD/t of pig-iron levels and practically coke specific consumption remains at relatively high rates of over 400 kg/t reflecting the existence of technological reserves recovered:

a) general measures to optimize the entire technological flow (the quality of the raw materials, the agglomerate, the pellets, the coke, the parameters of the elaboration process, including the distribution of the load and the gas distribution, the increase of the computerization of the process) of technological coke consumption in reference mode (no auxiliary fuels), roughly equal to the total fuel requirement under CDI conditions.

b) combustion intensification measures CDI:

- optimization of O_2 enrichment level of the insulated air;
- optimization of constructive and insufflation parameters of O_2 through lances;
- optimization of CDI burning parameters (O/C ratio, granulation, humidity, temperature and flame);
- reducing the possibilities of forming black and black fume in sewage plants;
- use of coal mixtures with different VM content that are easier to grind and have a lower heat dissipation.

References

[1]. *******, Documentation of ArcelorMittal Galati.
[2]. Xingu Ming, *Possibility of Combustion Blast furnace Operation with Oxygen*, University of Michigan, Mechanical Engineering, p. 3-2.
[3]. Harting W., et al. *Measures to increase blast furnace productivity*, Stahl und Eisen, Germany, nr. 6/2015.
[4]. Cheng A., *Coke Quality Requirements for Blast Furnaces, Part III*, vol. 28, no. 3, p. 39-40, March 2001.
[5]. Loison R., Foch P., Boyer A., *Coke Quality and Production*, Second edition, Butterworths Borough Green, Sevenoaks Kent TN15 8PH, England, ISBN 0-408-02870-X, 1989.
[6]. Robinson R., *High Temperature Properties of By-product Cold Bonded Pellets Containing Blast Furnace Flue Dust*, Thermochemical Acta, vol. 432, no. 1, p. 112-12, 2005.

THE ANNALS OF "DUNAREA DE JOS" UNIVERSITY OF GALATI
FASCICLE IX. METALLURGY AND MATERIALS SCIENCE
N°. 4 - 2017, ISSN 1453-083X

THE BEHAVIOR OF AN EXPERIMENTAL MODEL OF WIND TURBINE WITH VERTICAL AXLE WITH OVERLAPPED CUPS AT LOW WIND SPEEDS

Nelu CAZACU
"Dunarea de Jos" University of Galati
email: nelu.cazacu@ugal.ro

ABSTRACT

This work is based on an experimental model of vertical axis wind turbine (VAWT), which used a pair of hemispherical blades (cups) with variable overlap. Maintaining the rotation speed to a constant value and in order to meet an important criterion for a current generator fitted to the shaft via a speed multiplier is achieved with a centrifugal mechanism. The experiments conducted in laboratory conditions using experimental model wind tunnel at speeds below 4.5 m/s confirm the validity of the concept.

KEYWORDS: vertical axis wind turbine (VAWT), airfoil, hemispheric cup, overlap, gap

1. Introduction

Vertical axis wind turbines (VAWT) have as main characteristic simplicity constructive and independent of wind direction. "Savonius rotor", "Darrieus rotor" and "H-rotor" are considered the most representative classes VAWT [1].

Savonius wind turbine (SWT), with Savonius rotor, also called S-type rotor (see Fig. 1(b), Figure 2) is a wind vertical axis that uses "drag force", which represents tangential limit their speed of rotation that values close to the wind speed ($\lambda \approx 1$).

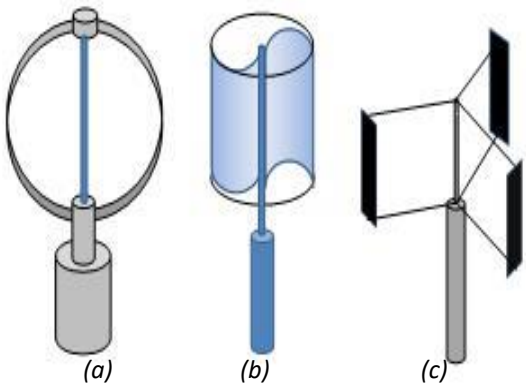

Fig. 1. *VAWT main models: (a) DWT - Darrieus wind turbine; (b) SWT - Savonius wind turbine; (c) HWT - "H" type wind turbines [1]*

SWT has a limited field of use determined by small output, with a maximum of approximately 18% (Betz limit) and a rotation speed low ($\lambda = 0,5 \ldots 1,5$). Use as aero water pumping systems is the best [2, 3].

Darrieus wind turbine (DWT, Figure 1 (a)) is a high-speed VAWT that uses "lift force", and has 2 or 3 blades. DWT is the main advantage of higher tangential speed, which offers advantages for use in power generation.

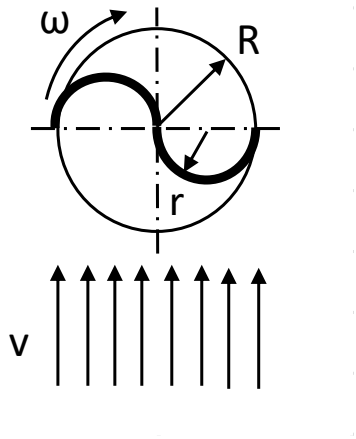

Fig. 2. *Savonius wind turbine*

"H" type wind turbine (HWT) comes from DWT and represents the middle portion, which led to

specific construction building structures with simplifications in achieving the tower and anchor and especially balancing axial forces.

Wind energy is pure kinetic energy and can be partially transformed into mechanical work [1, 2]:

$$E = \frac{1}{2} m v^2 \qquad (1)$$

where: E – wind kinetic energy, [J];
m – air mass, [kg];
v - is the wind speed, [m/s].

The volume flow over the swept area is:

$$\dot{V} = A \cdot v \qquad (2)$$

where: $\dot{V}$ – air volume flow, [m^3];
A – rotor swept area, [m^2].

And the mass flow results in:

$$\dot{m} = \rho \cdot A \cdot v \qquad (3)$$

where: $\dot{m}$ - air mass flow, [kg];
ρ - air density, [kg/m^3].

Hence, the power (energy per second) results:

$$P = \frac{1}{2} \cdot \rho \cdot A \cdot v^3 \qquad (4)$$

where: P – wind power, [W].

According to Betz's law, no turbine can capture more than 16/27 (59.3%) of the kinetic energy in wind. The factor 16/27 (0.593) is known as Betz's coefficient. The Savonius wind turbines (SWT) operate on the drag force and have much lower performance, approximately 15% (14.81%, with a Betz limit of maximum 4/27). Under the influence of the wind speed, the blades move at the velocity *u* under force *D* (Figure 3).

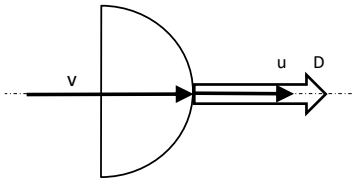

Fig. 3. *Drag force on each blade and wind [4]*

The drag force is [4]:

$$D = C_D \frac{1}{2} \rho (v - u)^2 A \qquad (5)$$

where: D – drag force, [N];
C_D - drag coefficient;
u - is the flow velocity relative to the object (rotor blade velocity).

The power obtained to each blade is:

$$P = D_u = C_D \frac{1}{2} \rho v^3 (1 - \frac{u}{v})^2 \frac{u}{v} A \qquad (6)$$

A dimensionless speed ratio is:

$$\lambda = \frac{u}{v} \qquad (7)$$

And power at turbine axle is [4]:

$$P = C_D \frac{1}{2} \rho v^3 (1 - \lambda)^2 \lambda A \qquad (8)$$

2. Experimental conditions

The schematic view of experimental model (EM) proposed with hemispheric cups is shown in Figure 4.

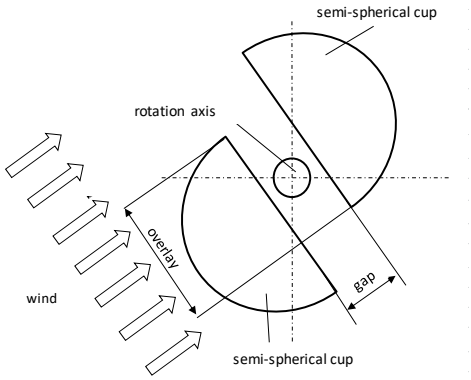

Fig. 4. *Schematic of VAWT Experimental Model with hemispheric cups*

Figure 5 shows the experimental model for VAWT with hemispheric cups tested.

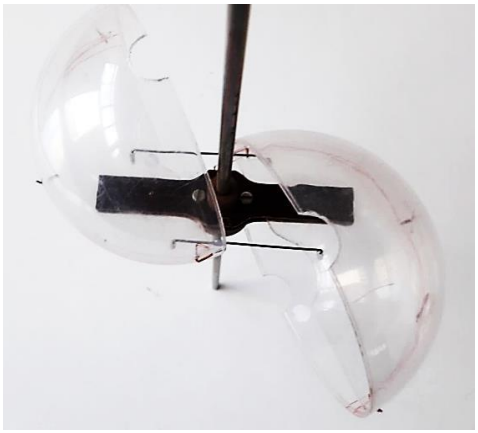

Fig. 5. *Experimental Model for VAWT with hemispheric cups*

The specifications of the scale model are shown in Table 1 and Table 2 presents the experimental conditions.

Table 1. *Experimental model characteristics*

no.	symbol	characteristics	value	m.u.	observation
1	r	sphere radius (cup)	0,055	m	cup shape
2	R	turbine radius	0,093	m	
3	n	blade number	2	-	
4	k	level number	1	-	
5	gmax	cup wall thickness	0,002	m	
6	gm	depth blade material	0,002	m	
7	PEc	blade material ME	-	-	PS
8	lp	blade long	0,173	m	
9	Sd	total blade surface	0,019	m2	
10	0	cup surface	0,009	m2	
11	S	swept area:	-	m2	
12	Smin	min	0,009	m2	
13	Smax	max	0,017	m2	plan diametral perpendicular pe vant
14	τ	rotor solidity:	0	0	
15	τmin	min	0,556	-	
16	τmax	max	1	-	
17	a	gap	0	m	variable
18	s	overlap	0,3	-	v ariable: 35...55%

Table 2. *Experimental conditions*

no.	symbol	characteristics	value	m.u.	observation
1	ta	air temperature	22	°C	measured
2	z	site altitude	40	m	Galati
3	Ta	absolute air temperature	295,16	K	0
4	0	air humidity	0	0	(Nelson, 2009), site
5	ρas	standard air density	1,225	kg/m3	15°C, sea level
6	ρa	real air density	1,19064558	kg/m3	with corrections (2) (Nelson, 2009)
7	Pr	atmospheric pressure	780	mmHg	measured
8	va	kinematic viscosity of air	0,00001568	m2/s	
9	ηa	dynamic viscosity of air	0,00001983	Ns/m2	
10	C_D	power coefficient of drag devices	1	-	(Nelson, 2009)
11	τ	time	60	s	measured
12	VP	vapour pressure	0	mmHg	

For the test experiments, a low-speed tunnel was used (V = 0...5 m/s) and a measurement section de 0,5 m x 0,5m. (S = 0,025 m^2). The swept surface was between 0.005 m^2 to 0.011 m^2 and was dependent on the overlay degree of the hemispherical cups (35% to. 55%).

3. Results and discussion

Performance results are presented in this section. The experimental data are presented in Table 3, Table 4, Table 5 and Table 6 and describe typical behaviour of "D-force" wind turbine [1, 5].

Table 3. *Obtained data for EM in wind tunnel experiments for 55% blade overlay*

exp.no.	revolutions		frequency	unghiular speed	periferic speed	specific speed	Reynolds number	specific power	power	conversion efficiensy
symbol	n		f	ω	vt	λ	Re	P/A	Pa	η
u.m.	rpm	rot/s	Hz	rad/s	m/s	-	-	W/m^2	W	-
1	0	0	0	0	0	0	0	0	0	0
2	0	0	0	0	0	0	0	0	0	0
3	0	0	0	0	0	0	0	0	0	0
4	0	0	0	0	0	0	0	0	0	0
5	0	0	0	0	0	0	0	0	0	0
6	0	0	0	0	0	0	0	0	0	0
7	0	0	0	0	0	0	0	0	0	0
8	0	0	0	0	0	0	0	0	0	0
9	180	3,00	3,00	18,84	1,75	0,42	65613	5,05	0,03	0,12

Table 4. *Obtained data for EM in wind tunnel experiments for 45% blade overlay*

exp.no.	revolutions		frequency	unghiular speed	periferic speed	specific speed	Reynolds number	specific power	power	conversion efficiensy
symbol	n		f	ω	vt	λ	Re	P/A	Pa	η
u.m.	rpm	rot/s	Hz	rad/s	m/s	-	-	W/m2	W	-
1	0	0	0	0	0	0	0	0	0	0
2	0	0	0	0	0	0	0	0	0	0
3	0	0	0	0	0	0	0	0	0	0
4	45	0,75	0,75	4,71	0,44	0,14	15149	1,72	0,01	0,08
5	87	1,45	1,45	9,11	0,85	0,25	29288	2,84	0,02	0,12
6	109	1,82	1,82	11,41	1,06	0,29	36694	3,44	0,02	0,12
7	157	2,62	2,62	16,43	1,53	0,40	52853	4,03	0,03	0,12
8	187	3,12	3,12	19,57	1,82	0,45	62952	4,33	0,03	0,11
9	189	3,15	3,15	19,78	1,84	0,44	63625	4,92	0,03	0,12

Table 5. *Obtained data for EM in wind tunnel experiments for 40% blade overlay*

exp.no.	revolutions		frequency	unghiular speed	periferic speed	specific speed	Reynolds number	specific power	power	conversion efficiensy
symbol	n		f	ω	vt	λ	Re	P/A	Pa	η
u.m.	rpm	rot/s	Hz	rad/s	m/s	-	-	W/m2	W	-
1	0	0	0	0	0	0	0	0	0	0
2	0	0	0	0	0	0	0	0	0	0
3	0	0	0	0	0	0	0	0	0	0
5	48	0,80	0,80	5,02	0,47	0,14	16159	1,79	0,02	0,09
6	129	2,15	2,15	13,50	1,26	0,37	43427	2,99	0,03	0,12
7	147	2,45	2,45	15,39	1,43	0,40	49486	3,39	0,03	0,12
8	171	2,85	2,85	17,90	1,66	0,44	57566	3,88	0,04	0,12
9	189	3,15	3,15	19,78	1,84	0,46	63625	4,30	0,04	0,11
0	192	3,20	3,20	20,10	1,87	0,45	64635	4,87	0,05	0,11

Table 6. *Obtained data for EM in wind tunnel experiments for 35% blade overlay*

exp.no.	revolutions		frequency	unghiular speed	periferic speed	specific speed	Reynolds number	specific power	power	conversion efficiensy
symbol	n		f	ω	vt	λ	Re	P/A	Pa	η
u.m.	rpm	rot/s	Hz	rad/s	m/s	-	-	W/m2	W	-
1	0	0	0	0	0	0	0	0	0	0
2	39	0,65	0,65	4,08	0,38	0,14	13129	0,99	0,01	0,09
3	86	1,43	1,43	9,00	0,84	0,27	28951	2,07	0,02	0,12
5	141	2,35	2,35	14,76	1,37	0,42	47466	2,38	0,03	0,12
6	135	2,25	2,25	14,13	1,31	0,38	45447	2,97	0,03	0,12
7	155	2,58	2,58	16,22	1,51	0,42	52179	3,32	0,04	0,12
8	180	3,00	3,00	18,84	1,75	0,46	60595	3,76	0,04	0,11
9	189	3,15	3,15	19,78	1,84	0,46	63625	4,30	0,05	0,11
0	207	3,45	3,45	21,67	2,01	0,49	69685	4,61	0,05	0,11

The data are first shown in terms of rotation speed rate (Figure 6), specific speed (Figure 7), Reynolds Number (Figure 8), specific power (Figure 9), power to the turbine shaft (Figure 10) and efficiency (Figure 11) for a range of wind speed (0 - 5 m/s) and different overlay (35% - 55%).

Figure 6 presents the speed variation in rpm with wind speed for different overlay. The maximum rpm is for 35% overlay and 4,2 m/s. Specific speed λ, was 0.5 for wind speed 4,2m/s and overlay 0.35.

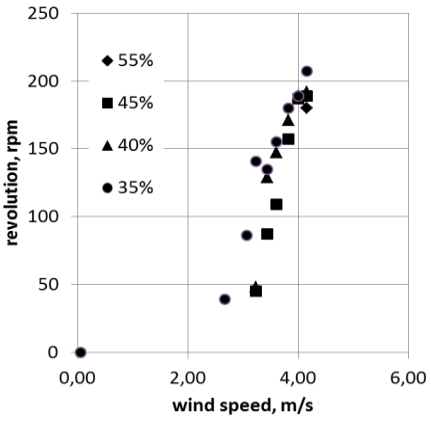

Fig. 6. *Rotation speed variations of EM with the wind speed for different overlay*

Figure 7 shows the specific speed variations of experimental model depending on wind speed at different overlay. Except for the experiments when *u* = 0, with no starting torque, λ approaches 0.5 for wind speeds approaching the maximum limit used for experiments.

The Reynolds Number (R_e) is the decisive factor in the air-flow in determining whether the inertial effect or the viscous effect wins. A low Reynolds Number gives laminar flow while a high Reynolds Number gives turbulent flow. Since the change in the Reynolds numbers influences the rotor design in many respects, in Figure 8 are presented the calculated Reynolds number as a function of wind speed under different overlay.

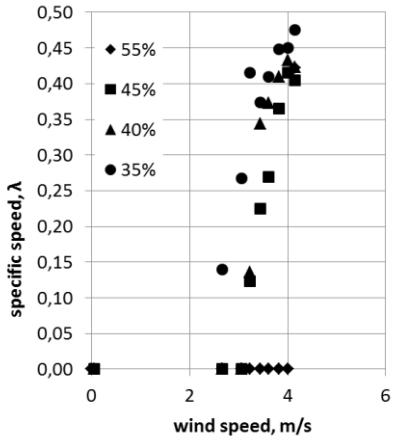

Fig. 7. *Specific speed variations of EM with the wind speed for different overlay*

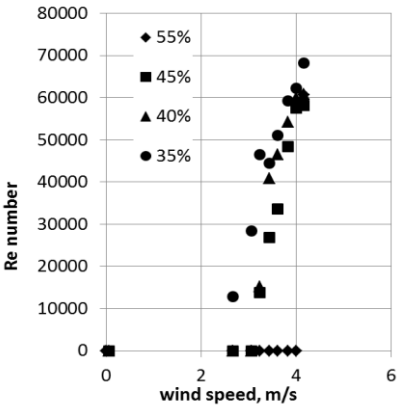

Fig. 8. *Re number variation for EM with the wind speed for different overlay*

Re number has a continuous increase for all experiments up to 70000 and the overlapping influence is small (Figure 8).

Figure 9 shows the specific power variations of experimental model depending on wind speed at different overlay.

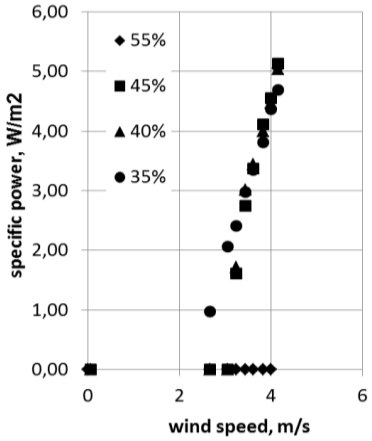

Fig. 9. *Specific Power of EM depending on wind speed and for different overlay*

Except in situations where EM had zero rotations speed, before having the starting torque, the specific power developed at the axle increases with the wind speed for all the experiments performed (Figure 9).

In Figure 10 is presented the power to the turbine shaft corresponding to experimental model depending on the wind speed at different overlay.

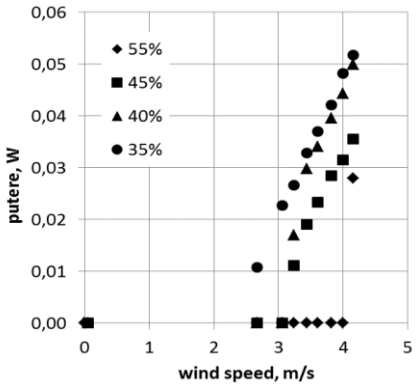

Fig. 10. *Power to the turbine shaft with the wind speed for different overlay*

When the experimental model rotates, the axle power is high when the overlay decreases and the wind speed approaches the maximum used in experiments 4.2 m/s (Figure 10).

Figure 11 shows the efficiency variations of experimental model depending on wind speed at different overlay.

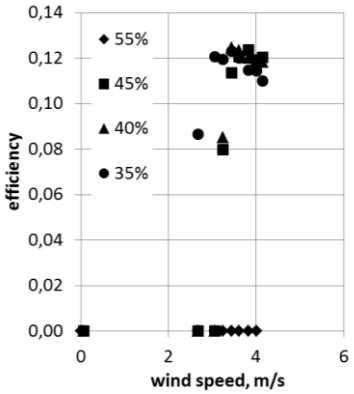

Fig. 11. *Efficiency variations of EM by wind speed for different overlapping*

Figure 12 shows the Re number values depending on specific speed of experimental model and for different overlay.

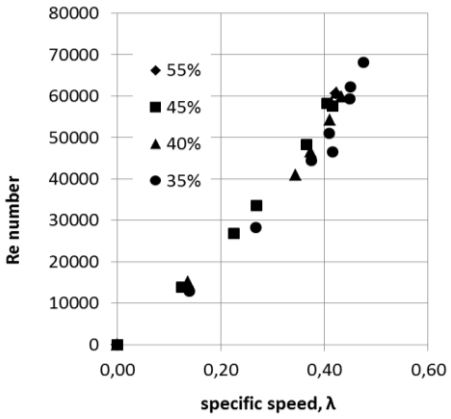

Fig. 12. *Re number values by specific speed of EM for different overlay*

Figure 13 present the efficiency variation depending on Re number and for different overlay.

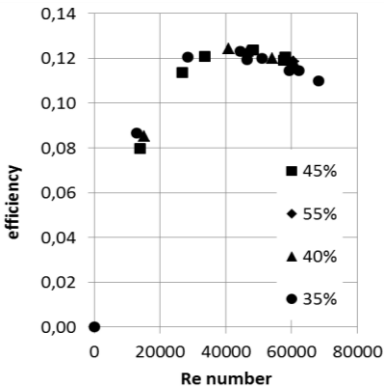

Fig. 13. *Efficiency variations of EM by Re number for EM tested in wind tunnel*

In Figure 12 it can be seen that Re number has a continuous increase with increasing of specific speed up to 70000 and the overlapping influence is small.

Efficiency calculated for the experimental model is between 0.11 and 0.13 when the Re number is between 30000 and 70000 as it can be seen in Figure 13.

4. Conclusions

Semi-spherical cups offer advantages in using them as blades for drag wind turbines that come from the sphere geometry (maximum volume at a fixed outer surface.

The conceptual model of VAWT with semi permeable cups with overlap and the distance between it and the gap was tested in laboratory conditions on a scale of 1:5 to 1:10 for wind speeds of less than 4, 2 m/s and no load. Experiments show that:

1. the existence of a wind velocity threshold for starting the rotational movement of the experimental model which increases with the increase of the overlapping of the cups.
2. for the wind speed range used (0 - 4.2 m/s), the relative speed reached about 0.5.
3. the Re number ranges from 30000 to 70000 depending on the wind speed.
4. the calculated conversion efficiency was between 0.11 and 0.13 for wind speeds of 3.0 to 4.2 m/s and is in line with the "drag-force" VAWT limit of 0.14 which is 0.14

References

[1]. Hau E., *Wind Turbines, Fundamentals, Technologies, Applications, Economics*, publisher: Springler, 2006.
[2]. Manwell J.F., McGowan J.G., Rogers A.L., *Wind Energy Explained. Theory, Design and Application*, publisher: John Wiley & Sons Ltd, p. 590, 2002.
[3]. Sathyajith M., *Wind Energy_Fundamentals, Resource Analysis and Economics*, publisher: Springer, 2006.
[4]. Smulders P.T., *Rotors for wind power.* Eindhoven: University of Technology, Eindhoven, Faculty of Physics, 1st edition October 1991, (revised edition January 2004).
[5]. Dumitrescu H., Georgescu A., *Calcului elicei*, Cap. 4 - *Elicea eoliana*, Editura Academiei Romane, 1990.
[6]. The European Wind energy association. *Wind in power. 2010 European statistics.* 2011.
[7]. Benesh A., *Wind turbine system using a vertical axis Savonius-type rotor, Patent - 4784568* US, 1988.
[8]. Burton T., Sharpe D., Jenkins N., Bossanyi E., *Wind Energy Handbook*, Publisher: John Wiley & Sons, Ltd, p. 463. ISBN 0 471 48997 2, 2001.
[9]. Contributors: European Wind Energy Association, European Commission. Directorate-General for Energy, *Wind Energy - The Facts, Vol.1 – Technology*, Publisher: European Wind Energy Association, 1997.
[10]. Kyozuka Y., *An Experimental Study on the Darrieus-Savonius Turbine for the Tidal Current Power Generation*, Journal of Fluid Science and Technology, Vol. 3, No. 3, pp. 439-449, 2008.
[11]. Menet J.-L., Bourabaa N., *Increase in a savonius rotor efficiency*, European Wind Energy conference, 2004.

THE ANNALS OF "DUNAREA DE JOS" UNIVERSITY OF GALATI
FASCICLE IX. METALLURGY AND MATERIALS SCIENCE
N°. 4 - 2017, ISSN 1453-083X

THE INFLUENCE OF THE NUMBER OF BLADES AND THE NUMBER OF LEVELS ON BEHAVIOR OF THE "S" -ROTOR EXPERIMENTAL MODELS

Nelu CAZACU
"Dunarea de Jos" University of Galati
email: nelu.cazacu@ugal.ro

ABSTRACT

The paper is based on wind tunnel (WT) experiments on experimental models (EMs), vertical axis wind turbines (VAWT), Savonius (SWT, "S" Turbine). The experimental models had the maximum dimensions: height of 0.395 m, and diameter of 0,150 m.

A study was conducted concerning the behavior of the EM experimental models for the level (1L) and three levels with a pair of blades (1PB) and a level with two pairs of blades (1L - 2PB). Wind speeds ranging from 0 to 2 m/s were used. Test section of the wind tunnel was 0,5 m x 0,5 m (0,25 m^2) and a shutter coefficient of 0,23. Experiments performed confirm the SWT's good behavior at low wind speeds and the possibility of being used to generate low-power electric power with DC generators.

KEYWORDS: vertical axis wind turbines, Savonius wind turbine

1. Introduction

Vertical axis wind turbines (VAWT) remain attractive for residential scale applications because the low conversion efficiency (Betz Limit, max. 14.81%) is offset by the performance of other system elements: battery buffers, LED (light emitting diode) lighting systems, high input voltage converters and all this at increasingly low prices [1, 2]. The only condition is the existence of a wind of 3 to 7 m/s for as long as possible in the year to make an investment efficient [3, 4]. Furthermore, the evolution of microprocessor-based electronic systems allows the management of dual power systems with wind turbine (Renewable Energy Sources - RES) and grid power, or triple power supply: solar, wind (RES) and grid [2]. All this leads to the use of Savonius wind turbines (SWT) as a primary source of mechanical work taken from wind energy and conversion to electricity with permanent magnet generators. The only condition is that SWT approaches with efficiency as much as 14.81%.

The power of wind (P) depends on wind speed (v), air density (ρ) and swept area (A):

$$P = 0{,}5\rho A v^3 \qquad (1)$$

The power extracted from a wind power by a VAWT Savonius type is depending by Drag force as follows:

$$D = C_D \frac{1}{2}\rho (v-u)^2 A \qquad (2)$$

where: u – is blade speed.

The power of wind becomes:

$$P = D_u = C_D \frac{1}{2}\rho v^3 (1-\frac{u}{v})^2 \frac{u}{v} A \qquad (3)$$

When $\lambda = \frac{u}{v}$, the extracted power becomes [5]:

$$P = C_D \frac{1}{2}\rho v^3 (1-\lambda)^2 \lambda A \qquad (4)$$

2. Materials and experimental conditions

For experimental testing, the following SWT models were used:

- EM1 (SWT-1L-1PB) made according to the classic SWT structure, two semi-cylindrical blades (one pair of blades, 1PB) on a level (1L) as is shown in Figure 1.

- EM2 (SWT-1L-2PB) made with four semi-cylindrical blades (two pairs of blades, 2PB) on a level (1L) as is shown in Figure 2.

- EM3 (SWT-3L-1PB) made with three levels (3L) of one pair of semi-cylindrical blades (1PB) as is shown in Figure 3.

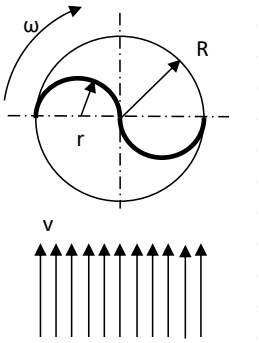

Fig. 2. *Transversal section through EM1 (SWT-1L-1PB)*

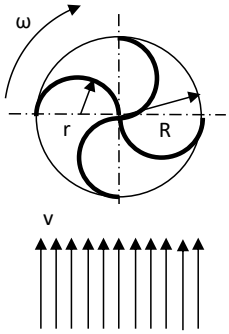

Fig. 2. *Transversal section through EM2 (SWT-1L-2PB)*

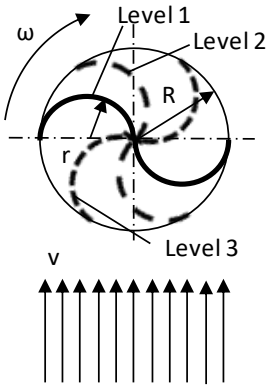

Fig. 3. *Image with EM3 (SWT-3L-1PB)*

The common features of the experimental models (EM1, EM2 and EM3) are shown in the Table 1 and the experimental conditions are presented in Table 2.

The Table 3 shows the wind characteristics of the wind tunnel (WT).

The wind tunnel used offers conditions for experimenting with experimental models at low wind speeds (< 4.5 m/s). The test section is 0.5 m x 0.5 m (0.25 m^2). The area occupied by the model is 23.5% of the measurement section. Real speed increases with the same percentage according to the Bernoulli equation. Wind speed was measured with LCA6000 anemometer. The speed of the experimental model is measured with the reed sensor and the Ventura IV system.

Table 1. *Experimental model common characteristics*

no.	symbol	characteristics	m.u.	relation	value	observation
1	H	high	m		0,39	input
2	R	rotor radius	m		0,075	input
3	D	rotor diameter	m	D=2R	0,15	
4	r	blade radius	m	r=R/2	0,0375	
5	AR	aspect ratio	-	Ar=H/D	2,6	
6	N	blade number	-	0	4	variable 1...4
7	k	level number	-	0	1	variable 1...3
8	0	blade airfoil	-	0	-	semi-cylindrical surface
9	h	blade high	m	h=r	0,022	
10	gm	depth blade material	m		0,002	input
11	PEc	blade material ME	-		-	PE
12	lb	blade long	m	lb=πr	0,118	
10	Ad	total blade surface	m2	Ad=lp.H	0,046	
11	As	rotor swept area:	m2			
12	Asmin	min	m2	Amin=hH	0,017	
13	Asmax	max	m2	Amax=R. H	0,059	
14	τ	solidity:	-			
15	τmin	solidity, min	-	τmin=Amin/Amax	0,293	
16	τmax	solidity, max	-	τmin=Amax/Amax	1	
17	a	gap	m		-	no gap
18	o	overlay	m		-	no overlay
19	m	total model mass	kg			measured

Table 2. *Experimental conditions*

no.	symbol	characteristics	m.u.	relation	value	observation
1	t	air temperature	◦C		25	measured
2	T	absolute air temperature	K	Ta=ta+273,16	298,16	
3	0	air humidity	%		0,3	(Nelson, 2009), weather
4	ρ	standard air density	kg/m3	-	1,225	la 15°C, nivelul marii
5	ρa	real air density	kg/m3	ρa=(353,049/T)e-0,034 z/T	1,17872	(Nelson, 2009), with corrections
6	Pr	air pressure	mmHg		780	weather
7	ϑ	kinematic air viscosity	m2/s		1,6E-05	(Matthews C, 2002)
8	ηa	dynamic air viscosity	Ns/m2		2E-05	(Matthews C, 2002)
9	VP	presiunea de vapori	mmHg		0	0
10	z	altitude	m		40	Galati city
11	τ	time	s		60	measured
12	CD	aerodynamic drag coefficient SWT	-		1	(Nelson, 2009)
13	ω	angular velocity	rad/s	ω=2πn; ω=2πf		variable
14	rev	revolutions	rpm			measured
15	I	moment of inertia	kgm2	I=mr2	0,00041	1rev=360°=2π;
16	m	mass of experimental model	kg	0	0,072	se măsoară pe balanță
17	Erot	kinetic energy (rotational)	J	Erot=1/2 Iω2		variable
18	v	wind speed	m/s			anemometer
19	u	tip speed	m/s	u=ωr		variable
20	λ	tip speed ratio,TSR	-	λ=u/v; λ=ωD/2u		variable
21	n	rotor speed (revolutions)	rpm			measured
22	σ	rotor solidity	-	σ=Nc/R	1	

Table 3. *Wind characteristics*

symbol	v	Ev	Pv	pv	0
u.m.	m/s	J	W	W/m2	W
1	4,25	158,80	2,65	45,24	0,39
2	3,81	114,41	1,91	32,60	0,28
3	2,62	37,20	0,62	10,60	0,09
4	2,48	31,55	0,53	8,99	0,08
5	2,21	22,33	0,37	6,36	0,06
6	2,01	16,80	0,28	4,79	0,04
7	1,80	12,06	0,20	3,44	0,03
8	1,59	8,32	0,14	2,37	0,02
9	0	0	0	0	0

The wind tunnel used offers conditions for experimenting with experimental models at low wind speeds (< 4.5 m/s). The test section is 0.5 m x 0.5 m (0.25 m^2). The area occupied by the model is 23.5% of the measurement section. Real speed increases with the same percentage according to the Bernoulli equation. Wind speed was measured with LCA6000 anemometer. The speed of the experimental model is measured with the reed sensor and the Ventura IV system.

Experiments were performed without mechanical or electrical load. All outputs are directly or indirectly dependent on wind speed in the tunnel [6-8]. For wind tunnel experiments on the EM1, EM2 and EM3 the maximum wind speed was 4.2 m/s.

3. Results and discussion

The resulted data are shown in terms of rotation speed (Figure 4), the power at the EM axis (Figure 5), Reynolds Number (Figure 6), power to the turbine shaft (Figure 7), specific speed (Figure 8) and axle frequency (Figure 9) for different wind speed (0 – 4.2 m/s).

The experimental results corresponding to SWT-1L-1PB are presented in Table 4, in Table 5 for SWT-1L-2PB and in Table 6 for SWT-3L-1PB. The rotational speed of the experimental models is shown in Figure 4.

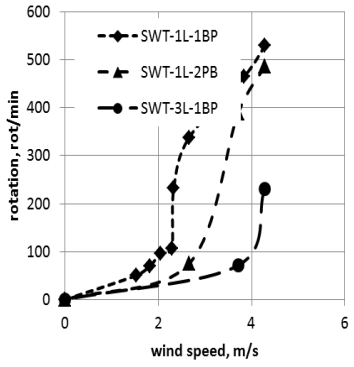

Fig. 4. *Rotation speed depending on wind speed for EM1, EM2 and EM3*

Table 4. *Results for experiments with SWT-IL-1PB*

symbol	n	0	f	ω	u	λ	Re	P/A	Pa	η
u.m.	rpm	rot/s	Hz	rad/s	m/s	-	-	W/m2	W	-
1	530	8,83	8,83	55,47	4,16	0,97	84908	0,04	0,00	0,00
2	465	7,75	7,75	48,67	3,65	0,95	74495	0,07	0,00	0,00
3	338	5,63	5,63	35,38	2,65	1,00	54149	0,00	0,00	0,00
4	232	3,87	3,87	24,28	1,82	0,78	37167	0,30	0,02	0,04
5	107	1,78	1,78	11,20	0,84	0,37	17142	2,41	0,14	0,34
6	96	1,60	1,60	10,05	0,75	0,37	15380	1,72	0,10	0,34
7	70	1,17	1,17	7,33	0,55	0,30	11214	1,47	0,09	0,41
8	50	0,83	0,83	5,23	0,39	0,26	8010	0,97	0,06	0,46
9	0	0,00	0,00	0,00	0,00	0,00	0	0	0	0

Table 5. *Results for experiments with SWT-IL-2PB*

symbol	n	0	f	ω	vt	λ	Re	P/A	Pa	η
u.m.	rot/min	rot/s	Hz	rad/s	m/s	-	-	W/m2	W	-
1	486	8,10	8,10	50,87	3,82	0,89	77859,18	0,41	0,02	0,01
2	388	6,47	6,47	40,61	3,05	0,82	62159,18	0,67	0,04	0,02
3	75	1,25	1,25	7,85	0,59	0,22	12015,31	1,26	0,07	0,11
4	0	0	0	0	0	0	0	0	0	0

Table 6. *Results for experiments with SWT-3L-1PB*

symbol	n	0	f	ω	vt	λ	Re	P/A	Pa	η
u.m.	rot/min	rot/s	Hz	rad/s	m/s	-	-	W/m2	W	-
1	231	3,85	3,85	24,18	1,81	0,42	37007	5,52	0,32	0,12
2	71	1,18	1,18	7,43	0,56	0,15	11374	2,77	0,16	0,09
3	0	0	0	0	0	0	0	0	0	0

From Figure 4 it can be seen that the Savonius wind turbine with 1L-1PB (EM1) has the highest rotational speed compared to the other two models (EM2 and EM3).

Figure 5 presents the power at the EM axis depending on the wind speed.

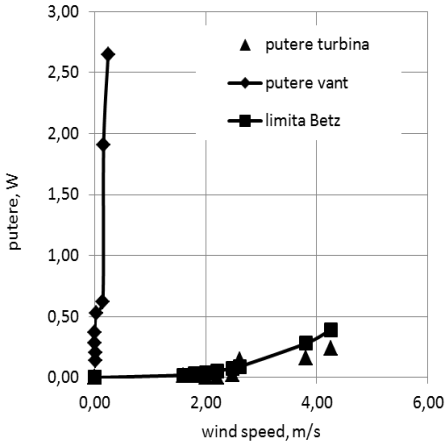

Fig. 5. *The power at the EM axis depending on the wind speed*

In Figure 6 are presented the calculated Reynolds number as a function of wind speed and Figure 7 indicates the variations of turbine wind power with the different wind speeds.

In Figure 7 it can be clearly seen that the best values in terms of turbine wind power correspond to experimental model EM3, which has the most even torque and the best start.

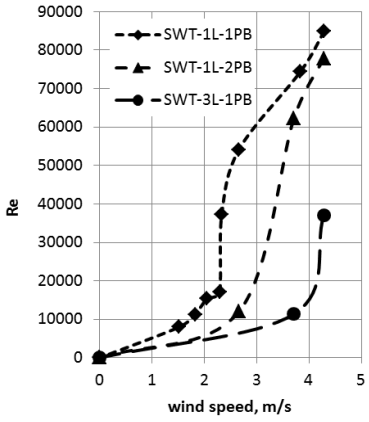

Fig. 6. *Variation of Re with wind speed*

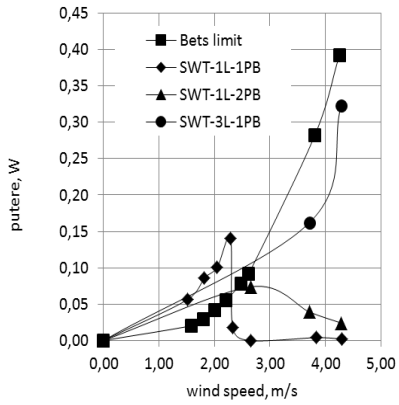

Fig. 7. *Turbine wind power for the experimental models depending on the wind speed*

In Figure 8 is presented the variation of specific speed as a function of wind speed.

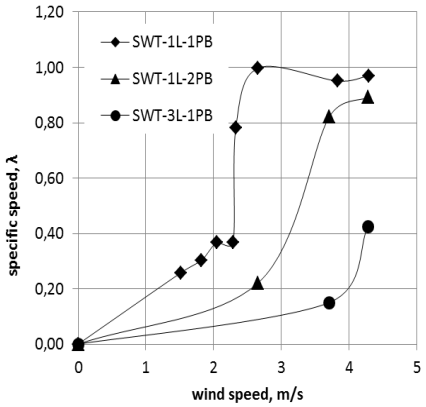

Fig. 8. *Specific speed (speed ratio) depending on wind speed*

Figure 9 shows the axle frequency variations depending on wind speed.

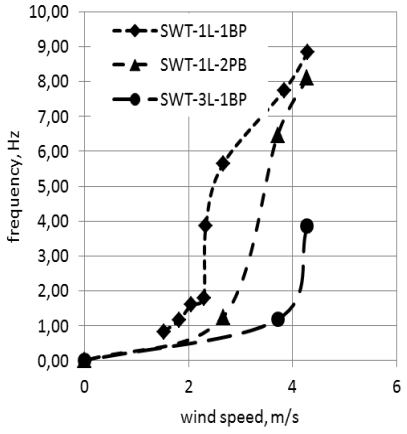

Fig. 9. *Axle frequency with wind speed*

Figure 9 shows that frequency of rotations of SWT axle has to small value for directly coupled to grid being necessary a mechanical multiplier with i=10 for EM1 and EM2 and a centrifugal regulator.

Figure 10 presents the variation of Re number depending on specific speed for all three experimental models tested.

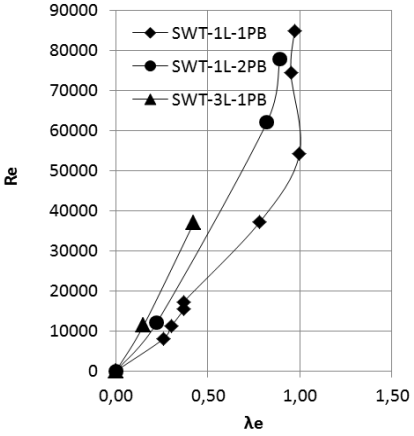

Fig. 10. *Re number variation with specific speed for EM's*

From Figure 10 it can be seen that the only EM that approaches λ = 1 is EM1 (classical SWT with 1L and 1PB). For the same λ, Re number is higher for SWT with 2PB and for λ <0,5 SWT with 3L and 1PB and each level offset at 120 °.

4. Conclusions

The best behavior in experiments was EM1 (classic Savonius wind turbine) with S-shaped blades which is consistent with: best sensitivity to the wind speed high rotation speed, high specific speed (close to 1) and a higher Re number.

The only problem is the low power which can develop at the shaft, and that the experiments recommend it for small powers.

For a higher power and with a possible greater uniformity at coupling, three-levels EM3 may be recommended.

For the use of turbines with a DC electric generator with permanent magnets with a one pair of magnetic pole, a speed around of 1200 rpm is required and a multiplier of i = 5 is required.

References

[1]. Blackwell B., *Wind tunnel performance data for two bucket savonius rotors*, 1977.

[2]. Badea N., *Sistem integrat de poligenerare descentralizata a energiei din surse regenerabile, CBI A/00402/2011*. 29 Aprilie 2011.

[3]. Manwell J.F., McGowan J.G., Rogers A.L., *Wind Energy Explained. Theory, Design And Application.* Publisher: John Wiley & Sons Ltd, p. 590, 2002.
[4]. Nelson V., *Wind Energy. Renewable Energy and the Environment.* Publisher: Taylor & Francis Group LLC, 2009.
[5]. Smulders P.T., *Rotors for wind power.* Eindhoven: University of Technology, Eindhoven, Faculty of Physics, 1st edition October 1991, (revised edition January 2004).
[6]. Piggot H., *Small Wind Turbine Design Notes.* 1998.
[7]. Menet J.L., Bourabaa N., *Increase in a savonius rotor efficiency,* European Wind Energy conference, 2004.
[8]. Saha U.K., Rajkumar M.J., *On the performance analysis of Savonius rotor with twisted blades,* 31, Vol. Renewable Energy, 2006.
[9]. Zigman A., *Optimization of a Savonis Rotor Vertical-Axes wind turbine.* Massachussets: MIT, 2007.

MANUSCRISELE, CĂRŢILE ŞI REVISTELE PENTRU SCHIMB, PRECUM ŞI ORICE CORESPONDENŢE SE VOR TRIMITE PE ADRESA:

MANUSCRIPTS, REVIEWS AND BOOKS FOR EXCHANGE COOPERATION, AS WELL AS ANY CORRESPONDANCE WILL BE MAILED TO:

LES MANUSCRIPTS, LES REVUES ET LES LIVRES POUR L'ECHANGE, TOUT AUSSI QUE LA CORRESPONDANCE SERONT ENVOYES A L'ADRESSE:

MANUSCKRIPTEN, ZIETSCHRITFTEN UND BUCHER FUR AUSTAUCH SOWIE DIE KORRESPONDENZ SID AN FOLGENDE ANSCHRIFT ZU SEDEN:

After the latest evaluation of the journals by the National Center for Science Policy and Scientometrics (**CENAPOSS**), in recognition of its quality and impact at national level, the journal will be included in the B^+ category, 215 code (http://cncsis.gov.ro/userfiles/file/CENAPOSS/Bplus_2011.pdf).

The journal is already indexed in:

SCIPIO-RO: http://www.scipio.ro/web/182206

EBSCO: http://www.ebscohost.com/titleLists/a9h-journals.pdf

Google Academic: https://scholar.google.ro

The papers published in this journal can be viewed on the website of "Dunarea de Jos" University of Galati, the Faculty of Engineering, pages: http://www.sim.ugal.ro, http://www.imsi.ugal.ro/Annals.html.

Name and Address of Publisher:
Contact person: Elena MEREUȚĂ
Galati University Press - GUP
47 Domneasca St., 800008 - Galati, Romania
Phone: +40 336 130139
Fax: +40 236 461353
Email: gup@ugal.ro

Name and Address of Editor:
Prof. Dr. Eng. Marian BORDEI
Dunarea de Jos University of Galati, Faculty of Engineering
111 Domneasca St., 800201 - Galati, Romania
Phone: +40 336 130208
Phone/Fax: +40 336 130283
Email: mbordei@ugal.ro

AFFILIATED WITH:

- THE ROMANIAN SOCIETY FOR METALLURGY
- THE ROMANIAN SOCIETY FOR CHEMISTRY
- THE ROMANIAN SOCIETY FOR BIOMATERIALS
- THE ROMANIAN TECHNICAL FOUNDRY SOCIETY
- THE MATERIALS INFORMATION SOCIETY (ASM INTERNATIONAL)

Edited under the care of the FACULTY OF ENGINEERING

Annual subscription (4 issues per year)

Editing date: 15.12.2017
Number of issues: 200
Printed by Galati University Press (accredited by CNCSIS)
47 Domneasca Street, 800008, Galati, Romania